View metadata, citation and similar papers at core.ac.uk
brought to you by CORE
provided by ScholarBank@NUS

DESIGN OPTIMIZATION OF SMALL-SCALE UNMANNED AIR VEHICLES

NG TZE HUI THOMAS

NATIONAL UNIVERSITY OF SINGAPORE
2006

DESIGN OPTIMIZATION OF SMALL-SCALE UNMANNED AIR VEHICLES

NG TZE HUI THOMAS
(*B.Eng. (Hons.), NUS*)

A THESIS SUBMITTED
FOR THE DEGREE OF DOCTOR OF PHILOSOPHY IN ENGINEERING
DEPARTMENT OF MECHANICAL ENGINEERING
NATIONAL UNIVERSITY OF SINGAPORE
2006

Acknowledgements

I would like to express my utmost gratitude to my project supervisor, Associate Professor Gerard Leng Siew Bing for his guidance and patience in the course of training me to think independently and critically. Without him, I would not have this privilege of pursuing a PhD in engineering.

Many thanks to the technical staff of Dynamics & Vibrations lab for their invaluable help and support, especially Mr. Ahmad Bin Kasa, Mr. Cheng Kok Seng, Ms. Amy Chee, and Ms. Priscilla Lee.

Table of Contents

Summary

In this thesis, new design methodologies have been developed for the design of small-scale unmanned air vehicle (UAV) and micro air vehicle (MAV). It is well known that the design of aircraft involves an iterative process of achieving trade-offs between conflicting aerodynamic, stability, propulsion, performance, structural requirements as well as some other mission-specific constraints.

This thesis describes the use of genetic algorithms to automate the design process for small-scale rotary-wing UAV/MAV, using commercial off-the-shelf components. A design methodology is also proposed for the aerodynamic shape design of a fixed-wing configuration.

A new unconventional configuration has been proposed for the purpose of producing rotary-wing UAV/MAV that is as easy to fabricate as the conventional quadrotor configuration, but possibly even smaller, given the availability of the same components. A detailed comparison is given in the thesis to assess the merits of the proposed configuration. A design methodology is also proposed to automate the design of this unconventional flight vehicle.

List of Figures

List of Tables

Nomenclature

b_2	fixed-wing MAV winglet span
B	breadth of component
BL plane	surface of the component comprising its breadth and length
BH plane	surface of the component comprising its breadth and height
$\bar{c}$	mean chord length
c_1	main wing chord
c_2	wing tip chord
c_3	winglet tip chord
C_D	drag coefficient
C_L	lift coefficient
C_M	pitching moment coefficient
CG	overall center of gravity of the rotary-wing UAV/MAV
$CG_{component}$	center of gravity of individual component
$d_{i,j}$	distance of the j^{th} component's CG from the origin in the i^{th} axis
f_i	fitness value of the i^{th} chromosome
$F_{tail,\ max}$	maximum thrust generated by tail rotor
H	height of component
HL plane	surface of the component comprising its height and length
K_n	static margin
K_v	voltage versus current constant of the propulsion set
K_{thrust}	thrust versus current constant of the propulsion set
K_{torque}	torque versus current constant of the propulsion set
L	length of component
L_{sf}	lift safety factor
$L_{tail,\ min}$	minimum distance of the tail rotor from the overall CG
m	mass of component
M_1	reaction torque produced by rotor 1 in JQUAD-rotor
M_2	reaction torque produced by rotor 2 in JQUAD-rotor

M_3	reaction torque produced by rotor 3 in JQUAD-rotor
M_4	reaction torque produced by rotor 4 in JQUAD-rotor
M_z	moment produced by the tail rotor about the Z-axis
N	total number of components used in the UAV/MAV
N_{chrom}	number of chromosomes in GA population
P_{roll}	percentage of lift contribution by roll motor
P_c	crossover rate
P_i	probability of i^{th} chromosome selected for reproduction
P_m	mutation rate
S	wing planform area
T_{flight}	flight time of rotary-wing UAV/MAV
T_{main}	torque generated by main rotor
U	airplane relative velocity
$V_{i,\ overlapped}$	volume of i^{th} component overlapping with the components already added in the design space by optimization
$V_{i,\ protrude}$	volume of i^{th} component protruding the main rotor plane
wt_j	weight of the j^{th} component
V_c	cruising speed
x	position of the component's center of gravity with respect to the X-axis
x_{ac}	aerodynamic center of the airplane
$X_{CG,\ L}$	shortest achievable x location of center of gravity
X_{CG}	position of the overall CG obtained by optimization with respect to the X-axis
$X_{CG,\ s}$	position of the desired overall CG with respect to the X-axis
X_{total}	overall x dimension of the UAV/MAV
y	position of the component's center of gravity with respect to the Y-axis
Y_{CG}	position of the overall CG obtained by optimization with respect to the Y-axis
$Y_{CG,\ s}$	position of the desired overall CG with respect to the Y-axis
Y_{total}	overall y dimension of the MAV

z	position of the component's center of gravity with respect to the Z-axis
Z_{CG}	position of the overall CG obtained by optimization with respect to the Z-axis
$Z_{CG,\ s}$	position of the desired overall CG with respect to the Z-axis
Z_{total}	overall z dimension of the MAV
$+z_{max}$	main rotor plane
α	angle of attack
δ	tolerance
δ_{prop}	minimum clearance between propellers obtained by optimization
$\delta_{prop,\ s}$	stiputaled minimum clearance between propellers
λ_m	main wing taper ratio
λ_w	winglet taper ratio
ϕ	roll Euler angle
θ	pitch Euler angle
θ_t	main wing twist angle
ρ	air density
ψ	yaw Euler angle
Ω_i	speed of i^{th} rotor in JQUAD-rotor

1. Introduction

Ever since the Wright brothers performed the first successful powered flight in 1903, there have been significant achievements in the science of aviation. As the boundaries of technology are pushed further with the launch of the biggest jet airliner A380 by Airbus, the conventional airplane is also shrinking with the advent of small-scale unmanned air vehicle (UAV) and palm-sized micro air vehicle (MAV).

An unmanned air vehicle, as its name implies, is practically the same as the conventional airplane, except that it does not carry a human pilot and hence can be much smaller in size. In recent years, there have been growing interests in the research development of small-scale UAVs and micro air vehicles or MAVs. MAVs belong to a class of flight vehicles that are very much smaller than UAVs. The definition employed in the research program of US Defence Advanced Research Projects Agency (DARPA) limits them to a size less than 15 cm in length, width and height.

Presently, UAVs are increasingly been employed in both civilian and military applications. In the industrial chemical sector, UAVs are valuable tool in assessing the site and searching for injured personnel when industrial accidents such as chemical spillage occur. Scientists conducting environment studies are experimenting with UAVs to collect important scientific data in dangerous environment such as an active volcano. There are also some attempts to use UAVs

for the surveying of dense forest areas, to detect fire spots early, so as to prevent the escalation to large-scale disastrous fire mishaps [1-16].

In search-and-rescue operations, UAVs have been used to assist in locating missing persons in remote areas, and the results are very encouraging. The agricultural industry has seen more UAVs been deployed, such as spraying of insecticides onto crops, as it is recognized to be a more economical option than using normal-sized piloted aircraft [17-29]. Law enforcement agencies have also started making use of UAVs to assist in their operations [30-49]. Traffic control authorities are also impressed by the performance of UAVs in traffic control [50-52]. These are just some of the numerous examples that show the increasing popularity and importance of UAVs in civilian applications.

As for military applications, UAVs are also receiving greater emphasis in the deployment of military operations. They are used mainly for border patrol and surveillance missions [53-74], such as the Pioneer UAV (Figure 1.1) which is currently operational in many countries worldwide. Another example is the Predator UAV which is already operational in the US military, and has participated in numerous combat missions and proven its high military value.

Figure 1.1. Photograph of the Pioneer UAV.

UAVs are not only being deployed closer to us in our daily activities, they are also going to be deployed in faraway space exploration missions. This is because it is still not feasible to have human astronauts exploring the atmospheres and terrains of these planets. Therefore, UAVs will be excellent substitutes for these dangerous tasks [75-77].

Currently, there are also research works on MAVs because they are much smaller in size and also more lightweight, offering greater portability and superior combat advantage in modern military warfare. Due to its miniature size, MAVs are able to operate in close proximity to the point of interest with minimum risks of detection. Thus, these miniature flight vehicles can provide surveillance teams with critical information, such as warning troops before they enter a danger zone. Fitted into an infantry soldier's backpack, MAVs do not incur much significant load on the combat personnel, but greatly enhance their combat capability. As no special automotive vehicles are required for the transportation of MAVs, they can be deployed in almost all kinds of terrain. One of the more promising works is the Black Widow developed by AeroVironment, with a wingspan of 15cm and a mass of only 56g (Figure 1.2).

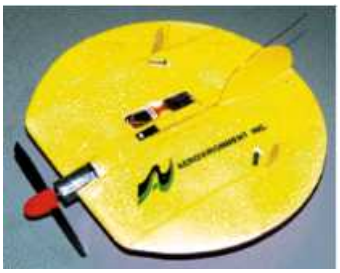

Figure 1.2. Photograph of the Black Widow MAV.

Flight vehicle design involves making many iterative trade-off studies between conflicting aerodynamic, stability, propulsion, performance and structural requirements. For example, a fixed-wing aircraft with long wingspan has greater aerodynamic efficiency but this imposes higher demands on its structural provisions, usually resulting in a greater overall weight. With an increase in overall weight, the aircraft must either have a larger wing area or more powerful propulsion, which will result in greater overall weight, making the problem a viscous cycle. Optimization has been recognized to be a powerful tool in the field of aircraft conceptual design. At this preliminary design stage, it is desirable to obtain the sizing and configuration layout for the flight vehicle quickly that will meet closely the requirements of the designer. The use of genetic algorithms (GA) as an optimization tool in aircraft design has shown great potentials [78-87].

1.1 Thesis objectives

This work aims to make use of genetic algorithms to automate the conceptual design of small-scale rotary-wing UAVs/MAVs. The generic GA has been modified to facilitate the optimization process. In order to minimize the research development and product cost, the strategy adopted here is to employ commercial off-the-shelf components in the design of the flight vehicles. Another reason for using commercial-off-the-shelf components instead of developing miniature ones is because of the unavailability of a team of researchers specializing in the different component disciplines. Thus, whether the small-scale UAV obtained by the design optimization can be small enough to match the MAV's definition will depend on the physical attributes of the commercial components that are available.

In addition, this thesis seeks to investigate the feasibility of an unconventional configuration that is as easy to fabricate as the quadrotor but possibly more compact, given the same range of component products to choose from.

Finally, with the encouraging results obtained in designing rotary-wing UAV/MAVs, a design methodology is proposed for the aerodynamic shape design of a fixed-wing MAV. A simple example is illustrated using a tailless fixed-wing configuration.

1.2 Thesis organization

Chapter 2 describes an automated design methodology in the design of rotary-wing UAV/MAV. This chapter focuses on the layout design and geometric sizing of a standard single main rotor and tail rotor configuration. The design problem is to obtain the most compact configuration subjected to physical and control constraints.

Chapter 3 describes an automated design methodology for a more complex design problem involving the layout design, geometric sizing and component selection of a quadrotor UAV/MAV configuration. The design problem is to select a suitable combination of components and position them such that it would be most compact without violating the physical and control constraints.

Chapter 4 introduces an alternative unconventional configuration rotary-wing UAV/MAV and explores its feasibility in producing UAV/MAVs smaller than the quadrotor configuration given the same available range of component products to choose from. A design methodology is also proposed to automate the design process of this unconventional flight vehicle. A model simulation of the proposed control mechanism is carried out to test the feasibilty of this new configuration.

Chapter 5 focuses on an automated design methodology for the conceptual design of a fixed-wing UAV/MAV using genetic algorithms. A description is given on how the design problem is formulated as a GA optimization problem. The GA optimization is then compared with another nonlinear optimization package, DONLP2.

Chapter 6 provides an overview of the workings of genetic algorithms (GA) and why they are becoming more popular in solving numerous engineering optimization problems. The modifications of the generic genetic algorithms to enhance its performance will also be explained.

In chapter 7, the main ideas and contributions of this research work are summarized, with some recommendations for future work.

2. Design Optimization of Single Main and Tail Rotar UAV/MAV

There are three main different types of UAVs and MAVs. The first type is the traditional fixed-wing configuration. The disadvantage of fixed-wing configuration MAV is that most of them need to fly typically at a minimum speed of more than 7m/s. With this flight speed constraint, Watkins [88] has commented that from his experience, the use of fixed-wing MAVs at outdoor environment is still a challenge at the present stage. Fixed-wing MAVs are more suitable for open terrain and not suitable for maneuvering in a densely populated urban environment where there are many buildings in close proximity.

The second type is the rotary-wing UAV/MAVs which can overcome this existing limitation of fixed-wing UAV/MAVs. Unlike the fixed-wing MAVs which need to fly constantly in order to stay airborne, the rotary-wing UAV/MAV has the distinct advantage of being able to hover at a fixed spot, making it very difficult to be detected. Moreover, rotary-wing UAV/MAVs have much greater maneuverability which allows them to travel around even inside a building.

The third configuration which is also receiving a lot of academic interest is a kind of insect-like flying machines [89-123]. The main motivation is to mimic the flying mechanisms of natural creatures in hopes of achieving even smaller MAVs than existing ones that have flown successfully. However, they are still in the experimental phase and not ready for operational deployment.

This chapter focuses on the design methodology to automate the configuration layout design and geometric sizing of a rotary-wing UAV/MAV that has a single main rotor and tail rotor configuration. The objective of this design optimization problem is to organize a given set of components and payloads, such that the resulting flight vehicle has the most compact overall size, and still fulfils the given physical and control constraints. A detailed discussion is presented to explain how the rotary-wing MAV design problem can be formulated as a GA optimization problem.

A low-cost approach to the development of a UAV/MAV can be achieved by integrating the smallest available commercial-off-the-shelf components (propulsion systems, sensors, power source, etc.). In this approach, one of the biggest challenges is to position the aircraft components and payloads, to achieve the smallest possible overall size, and still satisfy the physical and control constraints present.

This design optimization problem cannot be solved in a straightforward manner as the well-known knapsack, bin packing or container loading problem that other researchers, such as Martello et al. [124] and Pisinger [125] have proposed. This is because of the presence of additional constraints in the design problem. Firstly, there is a constraint on the location of the overall center of gravity (CG) for stability and control purposes. In addition, there is a need to impose a constraint on the minimum moment arm of the tail rotor, so that it is sufficient to counterbalance the torque produced by the main rotor. Moreover, some components such as the

main rotor assembly, tail rotor assembly and the rate sensors can only be mounted with specific orientation, making the design process even more complicated.

Crossley and Laananen [126] have previously attempted to use genetic algorithms in the conceptual design of rotary-wing aircraft. Their design focuses on conventional helicopters, instead of miniature rotary-wing flight vehicles. One common method in the layout design of rotary-wing flight vehicle is to vary the positions of the components in a trial-and-error manner, until all the above-mentioned constraints are satisfied. This approach is time consuming, and does not guarantee that the size of the flight vehicle is the smallest possible. Therefore, the objective of this study is to employ genetic algorithms to automate the layout design and geometric sizing of a rotary-wing UAV/MAV.

2.1 Problem Formulation

In the optimization design problem, the propulsion, control, sensors components and payload are modeled as rectangular blocks. The dimensions, length L, breadth B and height H (refer to Figure 2.1) of each block are defined by the smallest rectangular box that can enclose the component completely. These dimensions, along with the mass and center of gravity information, of all the components are measured and input into the optimization computer program.

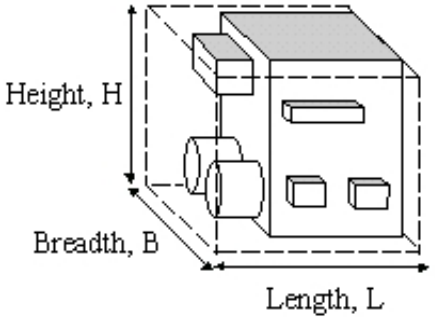

Figure 2.1. Dimension definition of individual component.

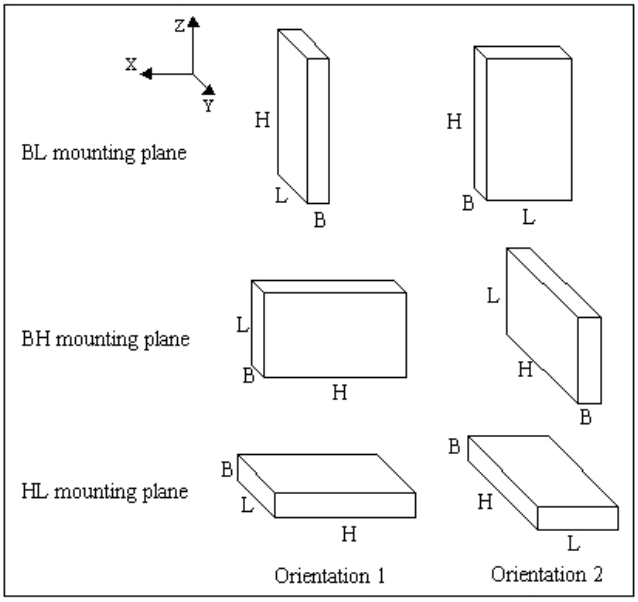

Figure 2.2. Mounting plane and orientation of component definition.

The position of each component's center of gravity ($CG_{component}$) in the design space is defined with respect to a Cartesian co-ordinate system whose origin is set at the base of rotor shaft of the main rotor assembly. Thus, the main rotor assembly does not need the x, y and z position design variables, thereby eliminating three design variables. The choice of setting the origin at the base of the main rotor shaft ensures that the main rotor's thrust will provide strictly a lifting thrust without

producing any roll or pitching moment. This will avoid the need for a constraint to ensure that there is no unbalanced roll or pitching moment caused by the main rotor's lifting thrust in the final configuration.

There are three possible surfaces to mount a component: its BL, BH or HL plane. These planes are arbitrarily chosen by designer on the component to identify the different sides of the component, independent of the global axes system used. The BL plane is the surface comprising its breadth and length. The BH plane is the surface comprising its breadth and height. Lastly, the HL plane is the surface comprising of its height and length. The mounting plane design variable is defined to be 1 for BL plane, 2 for BH plane and 3 for HL plane. Either the BL, BH or HL plane of the component can be mounted parallel to the XY plane of the global axes, as determined by the optimization process, except for certain components that have certain special limitations. For each mounting plane, the component can be orientated with respect to the X-axis in two different ways. For example, if the mounting plane chosen is the BL plane, the component can be oriented either with its BH plane or HL plane facing towards the positive X-axis (refer to Figure 2.2). Therefore, there are altogether six possible ways to mount a component into the flight vehicle, defined by three mounting planes and two orientations design variables. The design variables used in the geometric sizing and configuration design problem are the mounting plane, orientation and the (x,y,z) location of each component's center of gravity ($CG_{component}$) in the design space.

There are certain special restrictions on how some components can be mounted in the rotary-wing MAVs. Firstly, the main rotor assembly can only be positioned such that its rotational axis is perpendicular to the XY plane, i.e. parallel to the Z-axis (or yaw axis). Thus, it will only have the orientation variable and no mounting plane variable. The other component is the tail rotor assembly whose rotational axis must be parallel to the Y-axis (or pitch axis). The tail rotor assembly does not have the z location design variable as it must be placed such that its thrust-line is in the z = 0 plane, so that it will produce strictly a yaw moment and no roll moment. The tail rotor assembly can be mounted either on its BH or HL plane, but only with orientation type two. Hence, the lower bound of the tail rotor mounting design variable is two instead of one and it has no orientation design variable.

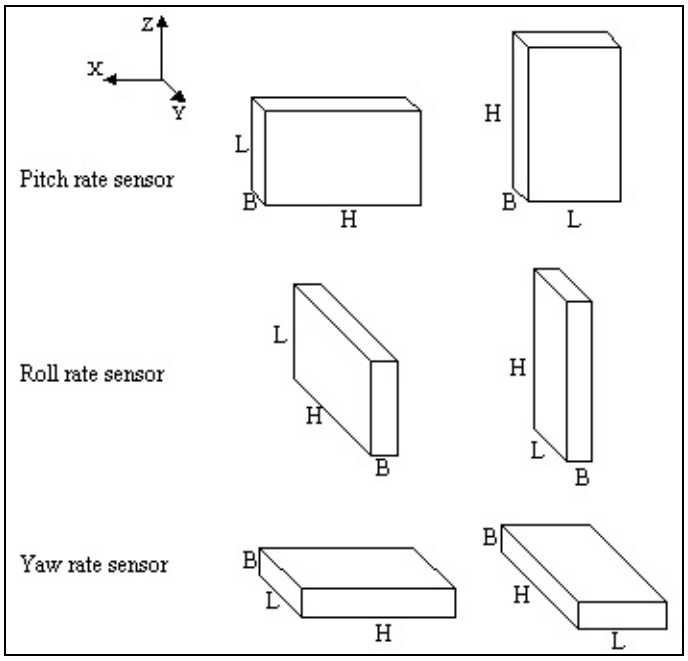

Figure 2.3. Rate sensors' allowed mounting planes and orientations.

The three rate sensors for measuring the rate of pitch, roll and yaw of the aircraft must be mounted such that its rotational axis is parallel to the corresponding roll, pitch and yaw axis. For the roll rate sensor, it can be mounted on its BH plane with orientation type two or on its BL plane with orientation type one. The pitch rate sensor can be mounted on its BH plane with only orientation type one or on its BL plane with orientation type two. Hence, both the roll and pitch rate sensors have mounting plane and no orientation variables. As for the yaw rate sensor, it can only be mounted on its HL plane with two possible orientations, and thus, has no mounting plane variable (refer to Figure 2.3).

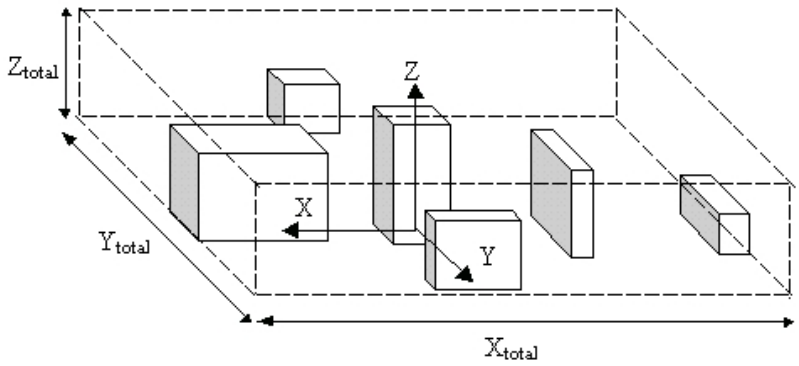

Figure 2.4. Definitions of overall dimensions of rotary-wing MAV.

The video camera does not have any orientation and mounting plane variable because it can only be mounted on its HL plane, with orientation type one. Therefore, it will only have three design variables, i.e. x, y and z position variables. The use of the video transmitter component contributes another five additional design variables – the three position, mounting plane and orientation variables.

It is desirable to minimize the overall dimensions of the flight vehicle, X_{total}, Y_{total} and Z_{total} (see Figure 2.4). This ensures that the frame that houses the components will be minimal, and also reduce the overall weight of the flight vehicle. Thus, this objective will produce a compact MAV that is easier to store, lightweight, and more difficult to detect. The optimization problem is formulated as

$$\text{minimize } X_{total} * Y_{total} * Z_{total} \tag{2.1}$$

subjected to the following four constraints on

(a) overlapping regions

(b) main rotor boundary

(c) moment arm of tail rotor

(d) overall CG location

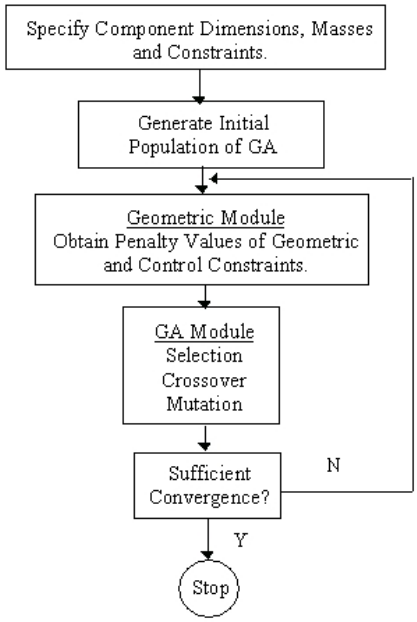

Figure 2.5. Flow chart of design optimization using GA.

A detailed explanation of these constraints is provided in the following sections. The optimization design flowchart using GA is shown in Figure 2.5.

2.2 Design Constraints

2.2.1 Overlapping regions constraint

It is apparent that not more than one component can occupy the same physical space. Thus, it is necessary to set this constraint in the design optimization. This constraint is incorporated into the objective function as a penalty function whose penalty value is equal to the volume of overlapped regions (see Figure 2.6) between the components. This ensures that as the components are positioned closer together, they do not actually cut into one another's region. The constraint function is given as

$$\sum_{i=2}^{N} V_{i,\,\text{overlapped}} = 0 \tag{2.2}$$

where $V_{i,\ \text{overlapped}}$ is the amount of overlapped volume experienced by the i^{th} component, i = 2, …, N.

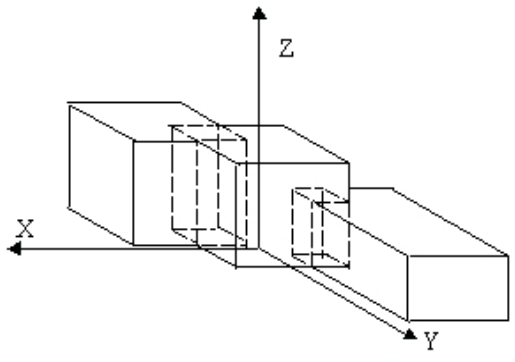

Figure 2.6. Overlapping-regions constraint.

The penalty function associated with this constraint is given as

$$h_1 = \sum_{i=2}^{N} V_{i,\ \text{overlapped}} \tag{2.3}$$

2.2.2 Main rotor boundary constraint

Another geometric constraint that needs to be imposed in the optimization problem is related to the plane in which the main rotor blade sweeps through. It is important that no component is placed such that it protrudes above the plane where the main rotor revolves. At first, this may seem to be a redundant constraint, since the origin is already set at the base of the main rotor assembly. The z plane of the main rotor would be known and could have been used as the upper bound for the z location of the other components. However, due to the three possible mounting planes that the component can be placed unto the MAV, there will be three possible z distances from the component's $CG_{component}$, depending on how it is mounted. Therefore, it will not be possible to use the upper bound of the z location variable to prevent the component from protruding above the main rotor plane.

The penalty incurred under this violation is equal to the volume of component that exceeds the main rotor plane, $+z_{max}$ (see Figure 2.7). Thus, the constraint function is given as

$$\sum_{i=2}^{N} V_{i,\ \text{protrude}} = 0 \tag{2.4}$$

where $V_{i,\ protrude}$ is the amount of protruded volume by the i^{th} component, i = 2, …, N.

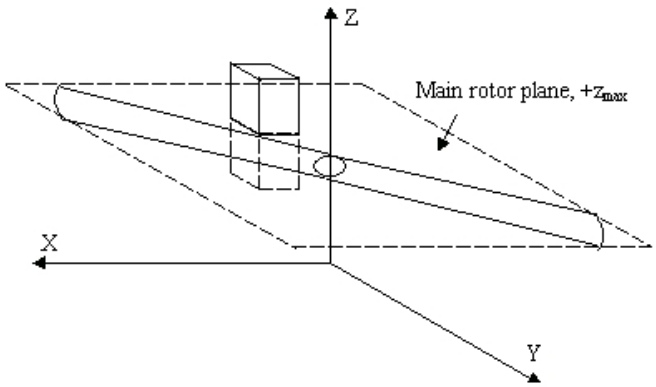

Figure 2.7. Maximum Z boundary constraint.

If this constraint is violated, the penalty function is

$$h_2 = \sum_{i=2}^{N} V_{i,\ protrude} \tag{2.5}$$

2.2.3 Moment arm of tail-rotor constraint

There is a limit as to how small the overall x dimension of the rotary-wing MAV can be achieved in reality. This is because the tail rotor has only certain finite amount of maximum thrust output, $F_{tail,\ max}$. The minimum allowable distance of the tail rotor from the actual CG, $L_{tail,\ min}$ is constrained by whether the tail rotor can provide enough counter-torque to balance the torque of the main rotor. Let M_z denote the moment produced by the tail rotor about the Z-axis, which is

$$M_z = F_{tail,\ max} * L_{tail,\ min} \tag{2.6}$$

Since the M_z has to be greater than the torque generated by the main rotor, T_{main}, the constraint becomes

$$M_z > T_{main} \tag{2.7}$$

By combining Eq. (2.6) into the inequality constraint Eq. (2.7), the minimum tail length inequality constraint can be expressed as

$$L_{tail,\,min} > T_{main} \,/\, F_{tail,\,max} \tag{2.8}$$

Since the thrust-line of the tail rotor passes through its own CG, this constraint can be satisfied by setting the lower bound of the x location of tail rotor to be = T_{main} / $F_{tail,\,max}$, avoiding the need of a penalty function. This arrangement will also reduce the amount of search time by removing the unnecessary search space.

2.2.4 Overall center of gravity constraint

It is possible to manually arrange the various components such that the final configuration fulfils the minimum tail length requirement. However, the resulting overall center of gravity of the flight vehicle may end up in an undesirable location that will render it very unstable (Prouty [127]). The choice of the overall CG location depends on the type of control systems implemented or the designer's personal preference. It is highly inefficient, if not impossible, to adopt a manual trial-and-error arrangement of the components to obtain the most compact MAV that will also satisfy the overall CG location constraint.

Once the mounting plane, orientation and position of the components are finalized, the overall center of gravity of the rotary-wing MAV can be calculated as follows,

$$CG_{i,j} = \frac{\sum_{j=1}^{N} (wt_j * d_{i,j})}{\sum_{j=1}^{N} wt_j}$$

(2.9)

where i = 1, …, 3, j = 1, …, N. $d_{i,j}$ is the distance of the j^{th} component's CG from the origin in the i^{th} axis, wt_j is the component's weight and N is the total number of components.

The constraints are defined as,

$$| X_{CG} - X_{CG,s} | < \delta$$

(2.10)

$$| Y_{CG} - Y_{CG,s} | < \delta$$

(2.11)

$$| Z_{CG} - Z_{CG,s} | < \delta$$

(2.12)

In practice, after all the components have been assembled with the wires fitted in, the final CG location may deviate slightly from the stipulated one. Therefore, a slight tolerance of $\delta = 1$ mm is allowed in these CG constraints. This will avoid the excessive computation in the search to enforce the more stringent constraints of $X_{CG} - X_{CG,s} = 0$, $Y_{CG} - Y_{CG,s} = 0$ and $Z_{CG} - Z_{CG,s} = 0$.

The penalty value of this constraint condition is given by the difference in the actual overall CG obtained by optimization (X_{CG}, Y_{CG}, Z_{CG}) and the stipulated CG location ($X_{CG, s}$, $Y_{CG, s}$, $Z_{CG, s}$).

$$h_3 = | X_{CG} - X_{CG, s} | - \delta \tag{2.13}$$

$$h_4 = | Y_{CG} - Y_{CG, s} | - \delta \tag{2.14}$$

$$h_5 = | Z_{CG} - Z_{CG, s} | - \delta \tag{2.15}$$

In this study, the chromosome is a string of mixed combination of integer and float numbers. The objective function in the GA optimization problem is defined as

$$\text{minimize } f = \sum_{i=1}^{5} \sigma_i h_i + \sigma_6 (X_{total} * Y_{total} * Z_{total}) \tag{2.16}$$

where $h_{i=1 \text{ to } 5}$ are the penalty functions defined for the constraints earilier, and $\sigma_{i=1 \text{ to } 6}$ are the weighing factors tabulated in Table 2.1.

Table 2.1. Table of weighing factors.

Weighing factors	Value
σ_1	1.996 x 10
σ_2	1.996 x 10
σ_3	1.996 x 10
σ_4	1.996 x 10
σ_5	1.996 x 10
σ_6	1.996 x 10^{-1}

2.3 Case Study

To investigate the feasibility of the proposed design strategy, the methodology is applied to the design of a single main rotor and tail rotor rotary-wing MAV using nine small-sized commercial-off-the-shelf components: main rotor assembly, radio receiver, tail rotor assembly, yaw sensor, pitch sensor, roll sensor, electric power-pack, video camera and video transmitter (refer to Table 2.2 for the components' dimensions and mass).

Table 2.2. Table of dimensions and mass of individual components.

	Component	Length, L (m)	Breadth, B (m)	Height, H (m)	Mass, M (kg)
1.	Main rotor assembly (excluding main rotor)	0.025	0.030	0.045	0.030
2.	Radio receiver	0.036	0.017	0.012	0.006
3.	Tail rotor assembly	0.015	0.010	0.035	0.008
4.	Yaw sensor	0.025	0.025	0.015	0.016
5.	Pitch sensor	0.025	0.025	0.015	0.016
6.	Roll sensor	0.025	0.025	0.015	0.016
7.	Electric power source	0.034	0.015	0.030	0.026
8.	Video transmitter	0.040	0.020	0.010	0.020
9.	Video camera	0.030	0.030	0.025	0.030

Altogether, there are 34 design variables, 11 integer number variables and 23 float number variables, whose lower and upper bounds are shown in Table 2.3. In this case study, the desired overall CG location has been arbitrarily chosen to be at the origin, i.e. $X_{CG,\,s} = 0.0$, $Y_{CG,\,s} = 0.0$, $Z_{CG,\,s} = 0.0$. The maximum Z boundary, $+z_{max}$ is given as z = 0.045 m and the tail length constraint value, $T_{main} / F_{tail,\,max} = 0.050$ m. The design optimizations are performed on a Pentium IV 2.4 GHz PC using many different sets of GA parameters.

Table 2.3. Table of design variables, corresponding bounds and final results.

	Variable Name	Lower Bound	Upper Bound	Values
1.	Main rotor assembly orientation	1	2	2
2.	Radio receiver mounting plane	1	3	2
3.	Radio receiver orientation	1	2	1
4.	Radio receiver x position (m)	-0.100	0.100	-0.020
5.	Radio receiver y position (m)	-0.100	0.100	-0.009
6.	Radio receiver z position (m)	-0.100	0.100	0.019
7.	Tail rotor mounting plane	2	3	2
8.	Tail rotor x position (m)	-0.100	-0.050	-0.050
9.	Tail rotor y position (m)	-0.100	0.100	0.000
10.	Yaw sensor orientation	1	2	2
11.	Yaw sensor x position (m)	-0.100	0.100	-0.032
12.	Yaw sensor y position (m)	-0.100	0.100	-0.004
13.	Yaw sensor z position (m)	-0.100	0.100	-0.020
14.	Pitch sensor mounting plane	1	2	1
15.	Pitch sensor x position (m)	-0.100	0.100	-0.007
16.	Pitch sensor y position (m)	-0.100	0.100	0.005
17.	Pitch sensor z position (m)	-0.100	0.100	-0.019
18.	Roll sensor mounting plane	1	2	2
19.	Roll sensor x position (m)	-0.100	0.100	0.025
20.	Roll sensor y position (m)	-0.100	0.100	0.010
21.	Roll sensor z position (m)	-0.100	0.100	-0.021
22.	Electric power source mounting plane	1	3	2
23.	Electric power source orientation	1	2	1
24.	Electric power source x position (m)	-0.100	0.100	0.022
25.	Electric power source y position (m)	-0.100	0.100	-0.010
26.	Electric power source z position (m)	-0.100	0.100	-0.017
27.	Video transmitter mounting plane	1	3	2
28.	Video transmitter orientation	1	2	2
29.	Video transmitter x position (m)	-0.100	0.100	-0.033
30.	Video transmitter y position (m)	-0.100	0.100	0.012
31.	Video transmitter z position (m)	-0.100	0.100	-0.012
32.	Video camera x position (m)	0.020	0.100	0.025
33.	Video camera y position (m)	-0.100	0.100	-0.001
34.	Video camera z position (m)	-0.100	0.100	0.027

2.4 Optimization Results

From Table 2.4, it can be seen that the GA parameters (population size, crossover rate P_c, and mutation rate P_m) do affect the outcome of the optimization process significantly. Firstly, a large population size is generally better than a small population size. The final results obtained using population size = 50 are usually poorer than the rest. However, increasing population size does not necessarily follow a linear relationship with optimality. This can be seen from the final results obtained with the population size parameter 400. Moreover, the advantage of a large population size comes with a price, which is an increase in computational overheads.

Table 2.4. Table of final values ($x10^{-4}$ m^3) obtained for different GA parameters.

	Mutation rate, P_m		
	5%	10%	20%
Population size = 50, P_c = 70%	4.018	2.914	3.164
Population size = 100, P_c = 70%	3.063	2.724	2.888
Population size = 200, P_c = 70%	2.794	3.235	2.558
Population size = 400, P_c = 70%	3.975	4.769	2.849
Population size = 50, P_c = 80%	3.584	2.923	4.176
Population size = 100, P_c = 80%	5.763	4.679	3.559
Population size = 200, P_c = 80%	3.069	3.628	2.775
Population size = 400, P_c = 80%	3.570	3.446	2.968
Population size = 50, P_c = 90%	3.727	3.398	3.250
Population size = 100, P_c = 90%	2.925	3.939	4.307
Population size = 200, P_c = 90%	5.231	3.732	3.498
Population size = 400, P_c = 90%	3.774	3.653	3.210

A higher crossover rate also tend to give rise to better results as there are more chances for the chromosomes to exchange their genes, increasing the probability of obtaining a more superior set of genes. When comparing the population size coupled with different crossover rate, it is seen that generally it is not possible to

obtain superior results from large population size unless there is also a higher crossover rate.

An examination on the effect of mutation rate reveals an interesting observation. There is a general trend that higher mutation rate tends to produce better solutions. This is one of the important attributes that make GA a more powerful optimization tool compared with many existing gradient-based optimization methods. The mutation operator helps to prevent the search process from being trapped in local minima, a problem that is unavoidable when using the conventional gradient-based methods. However, if the mutation rate is too high, the search may become an erratic and random process.

Therefore, the results presented here serve as a good guideline in selecting the GA parameters for the design optimization problem. It is advisable to use a high crossover rate P_c, and depending on the allowable design time given, to use a larger population size. In addition, when the allocated design time is short, a choice of high mutation rate can help to compensate the shortcomings of using small population size.

Figure 2.8 shows the layout obtained by the optimization process obtained at the first generation. It can be seen that the main motor and the video camera overlap, not surprising since the variables were generated at random initially. However, this overlapping problem is very quickly averted by the optimization process since it constitutes a bad solution, as seen at the tenth generation from Figure 2.9.

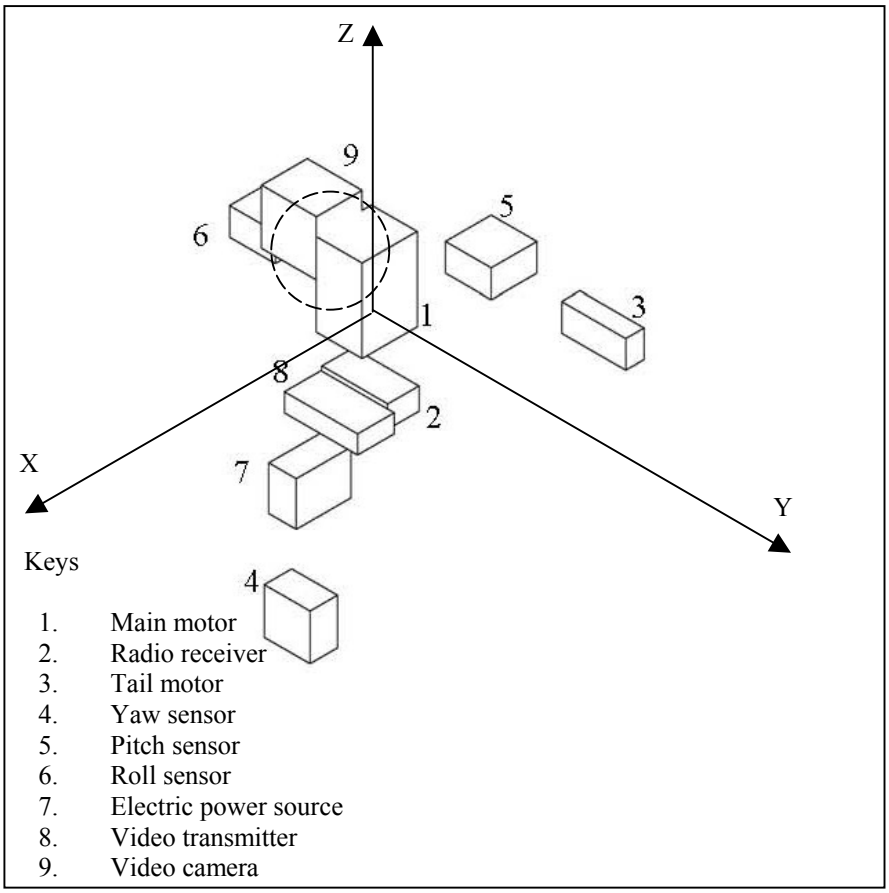

Figure 2.8. Layout obtained by optimization at first generation.

At the 30th generation (Figure 2.10), there is already a marked improvement in result as the components are much closer than the initial generations, and there is still no overlapping between the various components.

At only 324th generation (Figure 2.11), the layout can be seen to be very compact, and overlapping among the components is still prevented despite the present cramped layout.

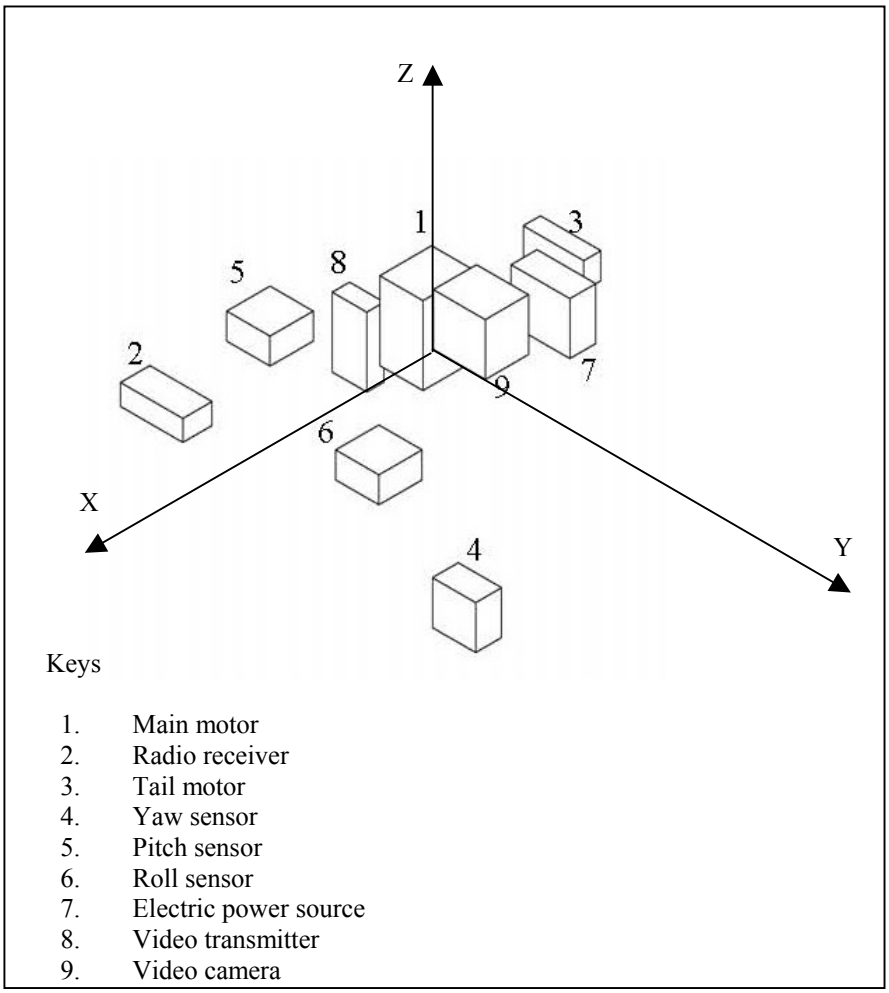

Figure 2.9. Layout obtained by optimization at tenth generation.

Finally, at the 1259th generation, the best layout and geometric sizing obtained from the design optimization (with all penalty functions $h_{i=1 \text{ to } 5}$ equal to zero) is shown in Figure 2.12 and its corresponding parameters tabulated in Table 2.3. The best overall dimensions are 0.093 x 0.035 x 0.079 m. The computational time taken is only 28 s. This research work on this topic has been published in [128-129].

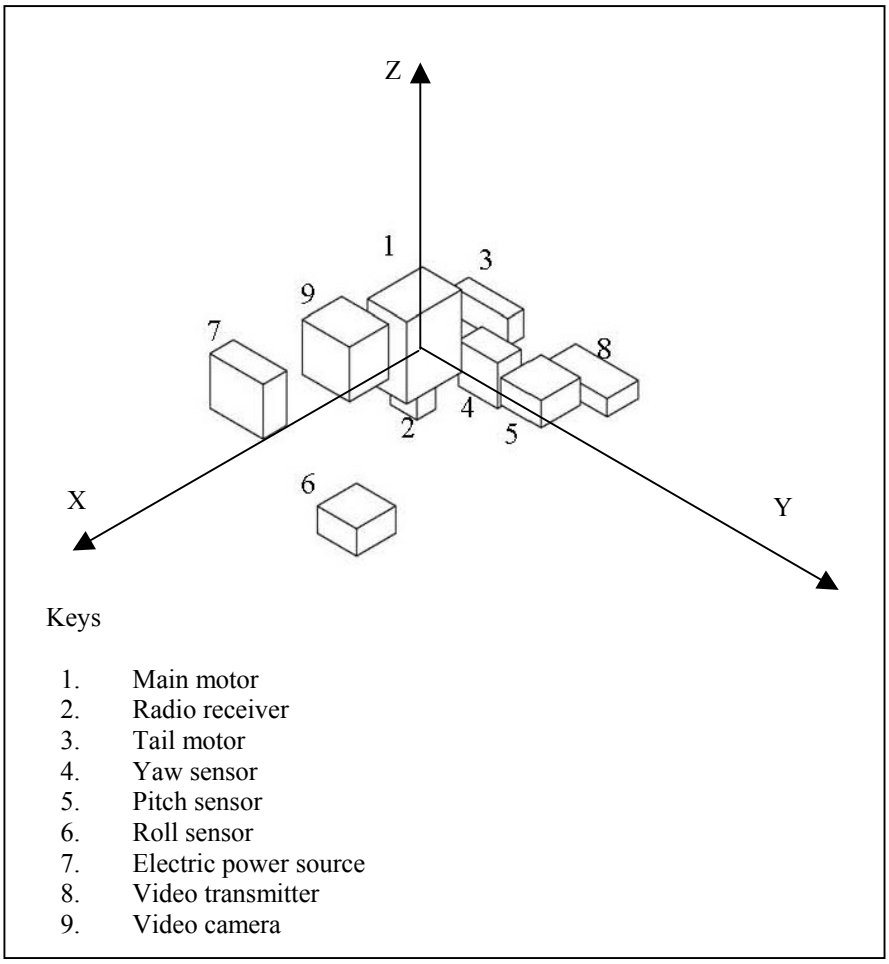

Figure 2.10. Layout obtained by optimization at 30th generation.

This design methodology is suitable for the cases where the designer has only one available set of components. The main and tail propulsion systems are able to produce sufficient thrust and uplift, and the power supply is able to provide the total current consumption.

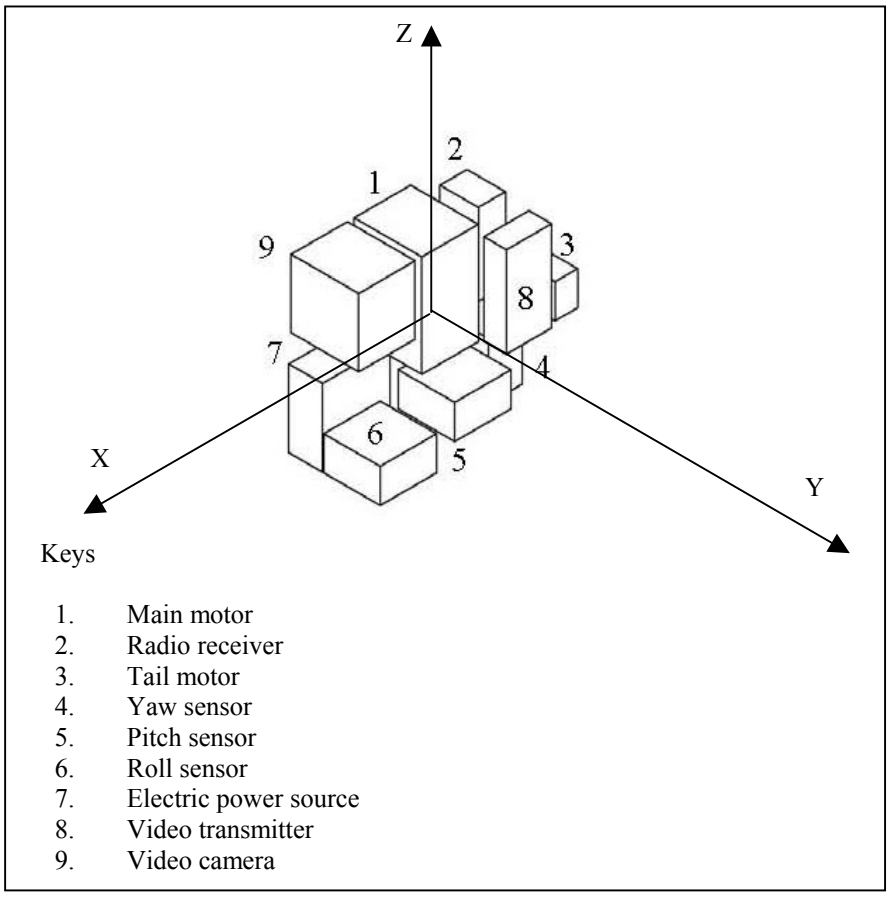

Figure 2.11. Layout obtained by optimization at 324th generation.

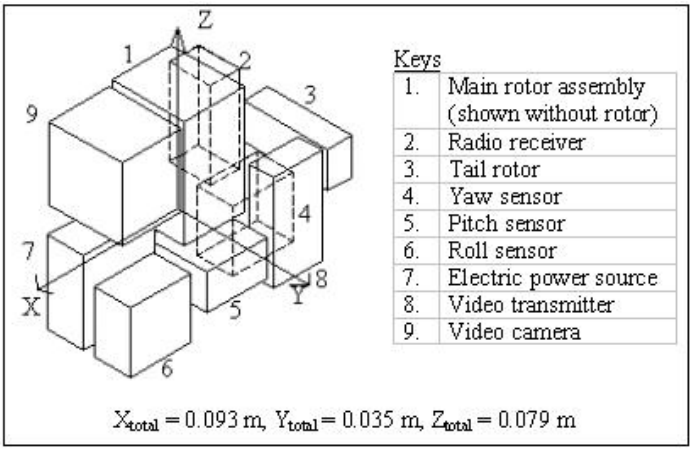

Figure 2.12. Final layout/geometric size obtained by optimizations.

2.4.1 Parallel computation results

In this section, an investigation is carried out to assess the performance of a parallel GA implementation of the design process. The model of parallel GA is called island model [130]. In this model, there is no distinction of master and slave nodes. Each node has a subpopulation or deme that performs the selection, crossover and mutation operations independent of the other subpopulations. However, exchange of individuals known as migration is possible.

The basic language tool for creating parallel programs for cluster computing is called the Message Passing Interface or MPI, a set of standard libraries [131] available in the common C and Fortran programming languages. With a few basic functions, such as MPI_Send(), MPI_Recv() and MPI_Bcast(), programmers are able to transfer data across the network of computers, dividing a big task into many simpler ones and speed up the overall computation.

Since GA has an element of randomness in its performance, the comparison between the serial GA and parallel GA will be carried out by repeating the optimization process 20 times. For the single machine, the GA population size is 200, while the parallel GA on 4 PCs will each have a subpopulation of size 50. The migration generation is set as 50. The optmization process will terminate if the improvement in the objective value is less than 0.5% for consecutively 1000 generations.

The average time taken for the serial GA to compute one generation is 0.034 s while the parallel GA takes an average time of 0.0068 s to complete one generation. From Table 2.5, the average time for convergence in the single machine's case is 2894 x 0.044 s = 98 s, while the average time for convergence in the parallel GA's case is 3077 x 0.0066 s = 21 s. Therefore, one can expect an average speedup of 98/21 = 4.6 for convergence to occur when the parallel GA is used. Comparing the quality of the converged values, the average parallel GA differs to the single machine average result by only 0.68%.

Table 2.5. Comparison of converged results between single machine GA and parallel GA for 20 runs.

	Single machine		4-node cluster	
Run	Converged value	Generation of convergence	Converged value	Generation of convergence
1	3.235E-04	2315	3.584E-04	3215
2	2.888E-04	2725	3.727E-04	2832
3	2.925E-04	2689	2.914E-04	3305
4	3.498E-04	3015	2.925E-04	3112
5	2.894E-04	2885	3.164E-04	2954
6	3.063E-04	2596	2.968E-04	2787
7	2.968E-04	2932	2.894E-04	3296
8	2.894E-04	3122	2.914E-04	3205
9	2.914E-04	2796	2.925E-04	2899
10	3.069E-04	2995	2.894E-04	3133
11	2.968E-04	3098	2.968E-04	2961
12	2.894E-04	2852	3.063E-04	3059
13	2.923E-04	3210	3.069E-04	3213
14	3.164E-04	2673	2.914E-04	2921
15	3.559E-04	3115	3.250E-04	3144
16	3.235E-04	2923	3.164E-04	2951
17	2.894E-04	2835	2.894E-04	3240
18	2.925E-04	3064	3.063E-04	3129
19	3.164E-04	3112	3.210E-04	2985
20	2.923E-04	2933	2.914E-04	3205
Average=	3.050E-04	2894	3.071E-04	3077

3. Design Optimization of Quadrotor UAV/MAV

In this chapter, the design methodology is still related to rotary-wing UAV/MAV, except the focus is on multiple-rotor configuration with no swash plate and linkage mechanism. Moreover, the complexity of the design problem is increased with the inclusion of component selection and additional design constraints.

The most common rotary-wing flight vehicle in operation is probably the Igor Sikorsky's single main and tail rotor configuration, flown successfully in 1939. The main rotor provides the lift and the tail rotor counteracts the torque generated by the main rotor, and hence prevents the vehicle from spinning around in the main rotor axis.

The control is performed via a cumbersome swash plate and linkage mechanism. Using the collective control, the entire swash plate assembly is raised as a unit. This changes the pitch of both blades simultaneously, and the aircraft will climb or descend accordingly. The cyclic control pushes one side of the swash plate assembly upward or downward. This changes the pitch of the blades unevenly depending on where they are in the rotation. Thus, the rotor has a greater angle of attack on one side of the helicopter and a lesser angle of attack on the opposite side. This allows the aircraft to move forward/backward or sideways.

It is not easy to fabricate and assemble the swash plate mechanism, especially for small-scale rotary-wing flight vehicle whose rotor size is less than 1m. The use of high precision machining process to fabricate such small-scale mechanism results

in high production cost. Another problem with this kind of mechanism is that through prolonged usage, mechanical wearing results in looseness or breakage in the linkages, causing inconsistency and uncertainty in control.

Another type of rotary-wing vehicle uses the tandem rotor configuration [132-133]. The tandem rotor configuration basically consists of two main rotors that rotate in opposite directions to cancel each other's torque reactions, and thus, there is no need for a tail rotor. One classic example of such configuration is the well-known military helicopter Boeing CH-47 Chinook. However, the swash plate and linkage control mechanism is still required to control the vehicle's motion. The coaxial-rotors configuration [134-136] works similarly to the tandem rotor configuration, except here, one rotor is directly above another, sharing the common rotational axis.

In quadrotor configuration [137], there are two pairs of tandem rotors, whereby the four rotors are arranged in a diamond shape. As the two pairs of rotors are of oppositely rotating rotors, the vehicle is balanced without the need of a tail rotor. In order to eradicate the swash plate and linkage mechanism, propellers or fixed-pitch rotors are used instead of variable-pitch rotors. The translational motion can be achieved completely by varying the thrust of a specific propeller or fixed-pitch rotor. Thus, this configuration is a good choice of rotary-wing UAV/MAVs that are easier to construct. Other researchers [138-143] have worked on the quadrotor UAV, but they have not adopted an automated design optimization approach to make their craft as compact as possible.

3.1 Problem Formulation

As in Chapter 2, the propulsion, sensors, radio receiver and other components are modeled as rectangular blocks. The dimensions, length L, breadth B and height H of each block are defined by the smallest rectangular box that can enclose the component completely. These dimensions, along with the mass, center of gravity, voltage requirement and power consumption information, are input into the optimization program.

The location of each component's center of gravity, $CG_{component}$ is defined with respect to a Cartesian co-ordinates system whose origin is set in center of the rotor formation (Figure 3.1).

Similar to Chapter 2, the design variables are the mounting plane, orientation and the (x, y, z) position of each component's center of gravity, $CG_{component}$ in the design space. However, in this chapter, the design problem has been extended to include component choice as a design parameter.

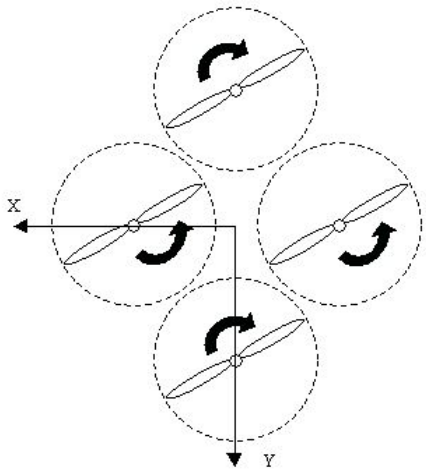

Figure 3.1. Quadrotor layout configuration.

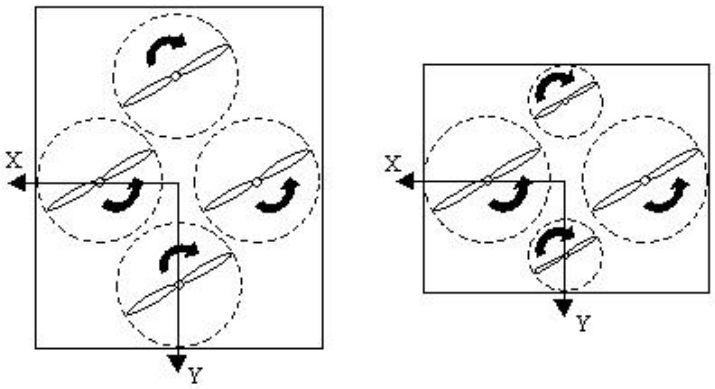

Figure 3.2. Comparison of two possible quadrotor layout configurations.

The selection of propulsion set is tricky as the more powerful propulsion sets can generate more thrust, but they are usually bigger, heavier and consume higher currents. In order to ensure that the more suitable ones are selected, the propulsion set choice is considered as one of the design variables. Instead of having only one propulsion set choice variable for all the four propulsion sets needed, it would be better to have two separate propulsion choice variables, one for the front/back pair and one for the left/right pair. As seen in Figure 3.2, this will allow a more compact configuration, if one of the two pairs has smaller propellers, and could still contribute sufficient lift to make the aircraft airborne.

In order for the flight vehicle to be balanced without any resultant pitch (about the Y-axis) and roll (about the X-axis) moments, each pair consists of two identical motors and propellers which are positioned in symmetry about the axis. Thus, each propulsion pair has only one location variable, the front/back pair will have a x location variable and the left/right pair will have a y location variable. The

front/back pair is only allowed to generate a pitching moment, and no roll moment, so its y position is fixed at y = 0. In the same line of thought, the left/right pair is only allowed to generate a rolling moment, and no pitching moment, so its x position is fixed at x = 0. The two pairs of propulsion sets have orientation variable and no mounting plane variable as they can only be mounted on its BL plane, with the rotational axis parallel to the Z-axis.

Another new design variable introduced here is the percentage usage of the maximum allowable current for each electric motor in the propulsion set, when the aircraft is hovering at a stationary spot. Each motor has a maximum allowable current consumption limit to prevent it from having a premature burnout. The reason for this new variable is because the choice of propulsion set is a variable, and thus, it is not known beforehand what will be its current consumption and the corresponding thrust output. Moreover, it should not be assumed that each motor would be drawing its maximum allowable current to produce its maximum possible thrust in order for the vehicle to become airborne and hover at a stationary spot. Another reason is because the electric power source which is a battery pack has a finite current output that may be insufficient to meet all the electric motors' maximum current consumption. Furthermore, if the two pairs are of different motor/propeller combinations, the more powerful pair must consume less current to balance the smaller torque created by the weaker pair.

There are many different types of commercial battery packs available and they are different in size, mass and capacity. In general, the greater the capacity of the

battery, the bigger and heavier it is, which then requires the motors to consume more current to generate more lift. If the designer chooses the lightest battery pack, it may not have enough current output to power the components or it may be sufficient to power all the components but for only a very short period to accomplish any meaningful task. As the choice of propulsion set and its usage of current are design variables, it is also not possible to decide on the suitable battery pack by the designer in advance. Thus, it is important to select one that is optimal, one that can supply sufficient current for an acceptable time period without incurring too much weight. This task is left to genetic algorithms by making the battery choice a design variable.

The other components such as gyros and radio receivers are also available with different specifications. Certain manufacturer's product may be lighter but bigger in size than other manufacturers'. Also, their current consumption may be different, one being better than the others. Hence, these components' choices are considered as GA design variables as well. For the video transmitter and video camera, there is only available information on one set of these components, so they will not have a component choice variable. If the technical data of more choices is available, they can then be added easily into the design problem.

Some of the necessary information about the propulsion set required by the design optimization are the minimum and maximum operating voltage for the motor, and the voltage versus current constant, K_v. In addition, the thrust versus current

constant, K_{thrust} and torque versus current constant, K_{torque} of the propulsion set are also essential. The current, I, used by each motor is given by

$$\text{I} = \text{percentage current usage} * \text{maximum allowable current} \tag{3.1}$$

where

$$\text{maximum allowable current} = \text{maximum allowable voltage}/ K_v \tag{3.2}$$

The thrust generated by the motor is

$$\text{Thrust} = I * K_{thrust} \tag{3.3}$$

and the torque produced is

$$\text{Torque} = I * K_{torque} \tag{3.4}$$

Propulsion set with higher K_{thrust} seems better as it produces more thrust with the same consumption as another propulsion set of lower K_{thrust}. However, they usually have a larger propeller and a greater reaction torque.

As in the previous chapter, it is desirable to minimize the overall dimensions of the vehicle's fuselage, $X_{fuselage}$, $Y_{fuselage}$ and $Z_{fuselage}$. This ensures that the frame that houses the components will be minimal and the overall weight of the flight vehicle will be reduced. Thus, this objective will produce a compact UAV/MAV that is easier to store, lightweight, and difficult to detect.

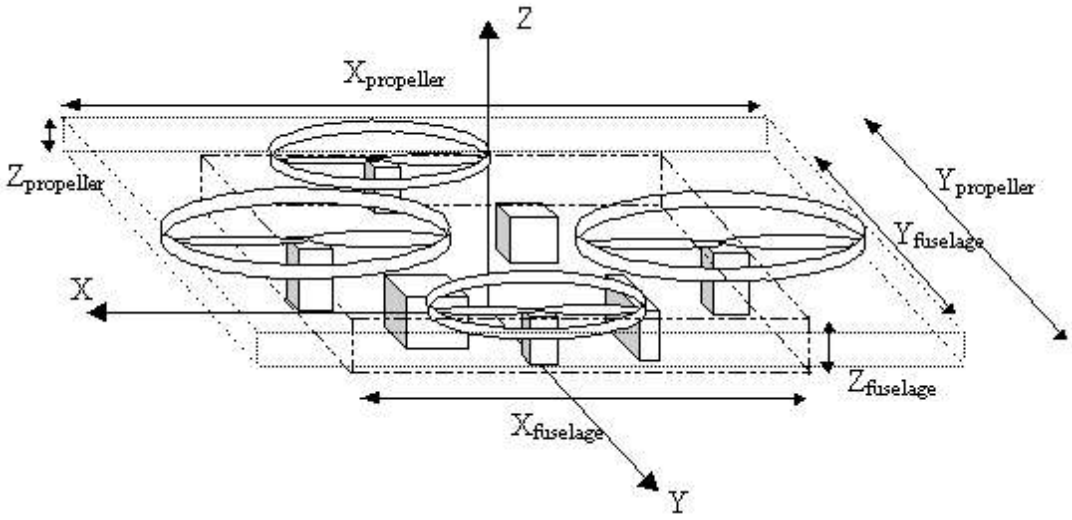

Figure 3.3. Definitions of overall dimensions of quadrotor UAV/MAV.

In addition, it is also desirable to minimize the overall dimensions of the vehicle's propellers, $X_{propeller}$, $Y_{propeller}$ and $Z_{propeller}$ (refer to Figure 3.3). This ensures that the propeller chosen will produce sufficient thrust and not larger than necessary. Thus, the optimization problem is formulated as

minimize

$$X_{fuselage} * Y_{fuselage} * Z_{fuselage} + X_{propeller} * Y_{propeller} * Z_{propeller} \tag{3. 5}$$

subjected to the following eight constraints on

a) overlapped regions

b) maximum Z boundary

c) overall CG location

d) inter-propeller distance

e) balanced yaw moment

f) minimum voltage and current of power source

g) lift-to-weight ratio

h) minimum flight time

3.2 Design Constraints

The first three constraints on overlapped regions, minimum z boundary and overall CG location are the same as described in Sections 2.2.1, 2.2.2 and 2.2.4 of Chapter 2. The subsequent five new constraints will be explained in the following sub-sections.

3.2.1 Inter-propeller distance constraint

Though the overlapped region constraint could enforce the propellers not to overlap one another, there is still a need to ensure that there is sufficient clearance between the propellers (Figure 3.4), and exactly how much this clearance should be will be decided by the designer. Thus, this additional constraint is defined as,

$$\delta_{prop} \geq \delta_{prop,\,s} \tag{3.6}$$

where δ_{prop} is the minimum clearance between propellers obtained by optimization and $\delta_{prop,\,s}$ is the stipulated clearance. If this constraint is violated, the penalty value is given by

$$h_6 = \delta_{prop,\,s} - \delta_{prop} \tag{3.7}$$

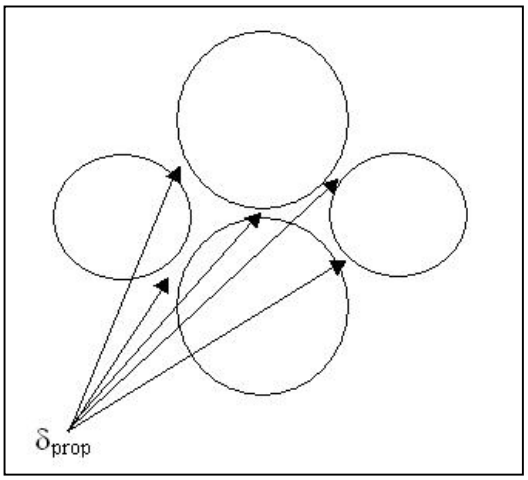

Figure 3.4. Location of the inter-propeller distance constraint.

3.2.2 Balanced yaw moment constraint

If the four propulsion sets are identical, and each set generates ¼ of the total lift required during hovering, the reaction torques will be of same magnitude and cancel each other. However, if the two pairs are not identical, it is not just sufficient for them to produce lift equal to the vehicle weight in order for the flight vehicle to hover at a stationary spot. At that instance, the reaction torques generated by the two different pairs must also cancel one another, so that there will be no net yaw moment that will cause the vehicle to spin around. This consideration is essential since there is no tail rotor in the quadrotor configuration that is responsible for the torque cancellation. Whether or not it is possible to have two pairs of different propulsion sets that can fulfill these conditions depends on the hardware availability, and this possibility should not be ruled out. The constraint is defined as

$$\sum \text{Moment}_{yaw} = 0$$

(3.8)

Instead of enforcing this equality constraint, a small tolerance δ can be allowed by the designer

$$|\sum \text{Moment}_{yaw}| < \delta$$

(3.9)

If this constraint is violated, the penalty value is given by

$$h_7 = |\sum \text{Moment}_{yaw}| - \delta$$

(3.10)

As mentioned earlier, because the two pair of propulsion sets are arranged in symmetry, there is no resultant pitch and roll moments, when each motor of the same pair produces the same amount of thrust during hovering. Hence, there is no need for two other constraints to enforce zero resultant pitch and roll moments.

3.2.3 Minimum voltage and current of power source constraint

Every component from different manufacturers has different power consumption, voltage and current requirements. Likewise, different electric power packs from different manufacturers have different capacity, voltage and current ratings. It is apparent that the voltage and current ratings of the electric power source must be equal or greater than the components' requirements in order for them to operate normally. In the case where the supply voltage is too high, a simple potential-divider circuit is used to tap the necessary voltage for the component, averting any possible circuit damage to the electrical components. Since the choice of the

electric power source is a design variable, it is necessary to enforce the following constraints,

$$V_{supply} \geq V_i \tag{3.11}$$

$$I_{supply} \geq \sum_{i=1}^{N} I_i \, , \; i \neq 5 \tag{3.12}$$

where V_i and I_i are the voltage and current requirements of the i^{th} component, V_{supply} is output voltage and I_{supply} is the output current of the power source. It is noted that component 5 is the power supply and its power consumption due to internal resistance is treated as negligible. The penalty value associated with the violation of these two constraints are given by

$$h_8 = [(\sum_{i=1}^{N} I_i) - I_{supply}], \; i \neq 5 \tag{3.13}$$

and

$$h_9 = \sum_{i=1}^{N} (V_i - V_{supply}), \; i \neq 5 \tag{3.14}$$

3.2.4 Lift-to-weight ratio constraint

Generally, the larger electric motors are more powerful and can generate more thrust. However, they are also heavier and thus contribute to the weight penalty of the vehicle. For a rotary-wing flight vehicle, there is a crucial requirement on its propulsion systems. The total thrust generated by the combination of electric

motors and propellers must be greater than the total weights of all the components and fuselage, in order for the flight vehicle to be airborne.

Since the objective function includes the minimization of the propellers, this constraint will ensure that propellers selected are not simply because they are the smallest, as they have to generate the required lift. This essential constraint is defined as,

$$L_p/W = 1 + L_{sf} \tag{3.15}$$

where L_{sf} is the lift safety factor, L_p is the total thrust (in kg) generated by the propulsion systems, W is the total mass of components and estimated fuselage mass.

Instead of enforcing this equality constraint, a small tolerance δ can be allowed by the designer

$$|(1 + L_{sf}) - L_p/W| < \delta \tag{3.16}$$

If this constraint is violated, the penalty value is given by

$$h_{10} = |(1 + L_{sf}) - L_p/W| - \delta \tag{3.17}$$

3.2.5 Minimum flight time constraint

It seems that all the necessary constraints have been considered after the components are positioned as close as possible without any overlapping, the overall CG, minimum thrust and electrical requirements fulfilled. However, it will serve no purpose if the UAV/MAV can only fly for a very short period to accomplish any meaningful mission. The flight time, T_{flight}, can be calculated as follow,

$$T_{flight} = \text{battery capacity / total current usage} \tag{3.18}$$

Therefore, there is a need to ensure that the flight vehicle is able to perform flight for a minimum stipulated time. This constraint is given as,

$$T_{flight} \geq T_{flight,\, s} \tag{3.19}$$

where T_{flight} is the actual flight time obtained and $T_{flight,\, s}$ is the desired minimum flight time. If this constraint is violated, the penalty value is given by

$$h_{11} = T_{flight,\, s} - T_{flight} \tag{3.20}$$

For the design problem, the goal is obtain the smallest possible overall vehicle volume. The objective function in the GA optimization problem is defined as

$$\text{minimize } f = \sum_{i=1}^{11} \sigma_i h_i + \sigma_{12} (X_{fuselage} * Y_{fuselage} * Z_{fuselage} + X_{propeller} * Y_{propeller} * Z_{propeller}) \tag{3.21}$$

where $h_{i=1 \text{ to } 11}$ are the penalty functions defined for the constraints and $\sigma_{i=1 \text{ to } 12}$ are the weighing factors tabulated in Table 3.1.

Table 3.1. Table of weighing factors.

Weighing factors	Value
σ_1	9.9989 x 10
σ_2	9.9989 x 10^{-5}
σ_3	9.9989 x 10^{-5}
σ_4	9.9989 x 10^{-5}
σ_5	9.9989 x 10^{-5}
σ_6	9.9989 x 10^{-5}
σ_7	9.9989 x 10^{-3}
σ_8	9.9989 x 10^{-5}
σ_9	9.9989 x 10^{-5}
σ_{10}	9.9989 x 10^{-5}
σ_{11}	9.9989 x 10^{-5}
σ_{12}	9.9989 x 10^{-8}

3.3 Case Study

To investigate the feasibility of the proposed design strategy, the methodology is applied to the design of the quadrotor UAV/MAV using 11 small-scale commercial-off-the-shelf components: four electric propulsion sets, radio receiver, pitch rate sensor, roll rate sensor, yaw rate sensor, electric power-pack, video transmitter and video camera. (Refer to Tables 3.2-3.4 for the components' technical specifications).

There are 45 design variables consisting of 20 integer variables and 25 float number variables, and their corresponding lower and upper bounds are shown in Table 3.5. In this case study, the desired overall CG location has been arbitrarily chosen to be at the origin, i.e. ($X_{CG, s}$, $Y_{CG, s}$, $Z_{CG, s}$) is (0, 0, 0). The minimum

required clearance between the propellers,$\delta_{prop,\ s}$ is 0.01 m, minimum desired flight time, $T_{flight,\ s}$ is 300 s and the lift safety factor, L_{sf} is 0.05. The estimated mass of fuselage and electrical wiring is set as 0.014 kg. The GA parameters used are population size of 100, crossover probability, P_c of 0.90 and mutation probability, P_m of 0.20.

Table 3.2. Table of specifications of available propulsion sets.

Component	L (m)	B (m)	H (m)	M (kg)	Propeller diameter (m)	Propeller height (m)	Min Voltage (V)	Max Voltage (V)	Thrust-to-current ratio (kg/A)	Torque-to-current ratio (Nm/A)	Voltage-to-current ratio (V/A)
Propulsion set #1	0.012	0.010	0.015	0.006	0.065	0.008	4.0	8.0	0.03	0.01	10.18
Propulsion set #2	0.012	0.010	0.015	0.0076	0.200	0.015	4.0	8.0	0.0595	0.021	10.18
Propulsion set #3	0.012	0.012	0.018	0.0126	0.200	0.015	4.0	10.0	0.0837	0.020	9.22
Propulsion set #4	0.012	0.012	0.018	0.0132	0.230	0.015	4.0	10.0	0.0797	0.026	9.00
Propulsion set #5	0.012	0.012	0.018	0.0136	0.260	0.015	4.0	10.0	0.0904	0.034	11.96
Propulsion set #6	0.017	0.017	0.017	0.0206	0.260	0.015	4.0	10.0	0.1056	0.032	12.52
Propulsion set #7	0.015	0.015	0.024	0.0249	0.280	0.015	4.0	10.0	0.1444	0.036	13.16

Table 3.3. Table of specifications of available electric power sources.

Component	L (m)	B (m)	H (m)	M (kg)	Voltage output (V)	Current output (A)	Capacity (Ah)
Electric Power Source #1	0.045	0.015	0.051	0.051	9.0	2.0	0.770
Electric Power Source #2	0.015	0.015	0.153	0.051	9.0	2.0	0.770
Electric Power Source #3	0.045	0.015	0.034	0.036	9.0	1.0	0.425
Electric Power Source #4	0.015	0.015	0.102	0.036	9.0	1.0	0.425
Electric Power Source #5	0.070	0.028	0.014	0.055	9.6	2.0	0.110
Electric Power Source #6	0.045	0.030	0.051	0.102	9.0	4.0	1.540
Electric Power Source #7	0.030	0.015	0.102	0.102	9.0	4.0	1.540
Electric Power Source #8	0.070	0.028	0.028	0.110	9.6	4.0	0.220
Electric Power Source #9	0.036	0.021	0.022	0.028	11	3.6	0.350

Table 3.4. Table of technical specifications of other components.

Component	L (m)	B (m)	H (m)	M (kg)	Voltage (V)	Current (A)
Rate sensor #1	0.025	0.025	0.013	0.009	3.0	0.014
Rate sensor #2	0.027	0.026	0.012	0.005	4.8	0.010
Radio receiver #1	0.027	0.015	0.006	0.003	5.0	0.010
Radio receiver #2	0.036	0.017	0.012	0.006	5.0	0.010
Video camera	0.026	0.026	0.015	0.012	9.0	0.100
Video transmitter	0.030	0.018	0.010	0.007	9.0	0.300

Table 3.5. Table of design variables and corresponding bounds (quadrotor design).

	Variable Name	Lower Bound	Upper Bound
1.	Front/back propulsion choice	1	7
2.	Left/right propulsion choice	1	7
3.	Front motor orientation	1	2
4.	Back motor orientation	1	2
5.	Left motor orientation	1	2
6.	Right motor orientation	1	2
7.	Front propulsion x position (m)	0.001	0.500
8.	Left propulsion y position (m)	0.001	0.500
9.	Front/back propulsion percentage usage of maximum allowable current	0.010	0.990
10.	Left/right propulsion percentage usage of maximum allowable current	0.010	0.990
11.	Radio receiver choice	1	2
12.	Radio receiver mounting plane	1	3
13.	Radio receiver orientation	1	2
14.	Radio receiver x position (m)	-0.500	0.500
15.	Radio receiver y position (m)	-0.500	0.500
16.	Radio receiver z position (m)	-0.500	0.500
17.	Pitch rate sensor choice	1	2
18.	Pitch rate sensor mounting plane	1	2
19.	Pitch rate sensor x position (m)	-0.500	0.500
20.	Pitch rate sensor y position (m)	-0.500	0.500
21.	Pitch rate sensor z position (m)	-0.500	0.500
22.	Roll rate sensor choice	1	2
23.	Roll rate sensor mounting plane	1	2
24.	Roll rate sensor x position (m)	-0.500	0.500

25.	Roll rate sensor y position (m)	-0.500	0.500
26.	Roll rate sensor z position (m)	-0.500	0.500
27.	Yaw rate sensor choice	1	2
28.	Yaw rate sensor orientation	1	2
29.	Yaw rate sensor x position (m)	-0.500	0.500
30.	Yaw rate sensor y position (m)	-0.500	0.500
31.	Yaw rate sensor z position (m)	-0.500	0.500
32.	Electric power source choice	1	9
33.	Electric power source mounting plane	1	3
34.	Electric power source orientation	1	2
35.	Electric power source x position (m)	-0.500	0.500
36.	Electric power source y position (m)	-0.500	0.500
37.	Electric power source z position (m)	-0.500	0.500
38.	Video transmitter mounting plane	1	3
39.	Video transmitter orientation	1	2
40.	Video transmitter x position (m)	-0.500	0.500
41.	Video transmitter y position (m)	-0.500	0.500
42.	Video transmitter z position (m)	-0.500	0.500
43.	Video camera x position (m)	0.000	0.500
44.	Video camera y position (m)	-0.500	0.500
45.	Video camera z position (m)	-0.500	0.500

3.4 Optimization Results

At the first generation, only three out of the eight constraints are violated (Table 3.6). From Figure 3.5, it can be seen that the components are well spread out, and thus do not overlap with one another. However, the CG location obtained is not at the desired origin. The front/back propeller is 23cm while the left/right propeller is 26cm in diameter. The total lift generated is also lesser than the total mass, and thus the solution at this instance is still not a feasible one. It is not a surprise as this is only the first generation and improvement in results can be expected.

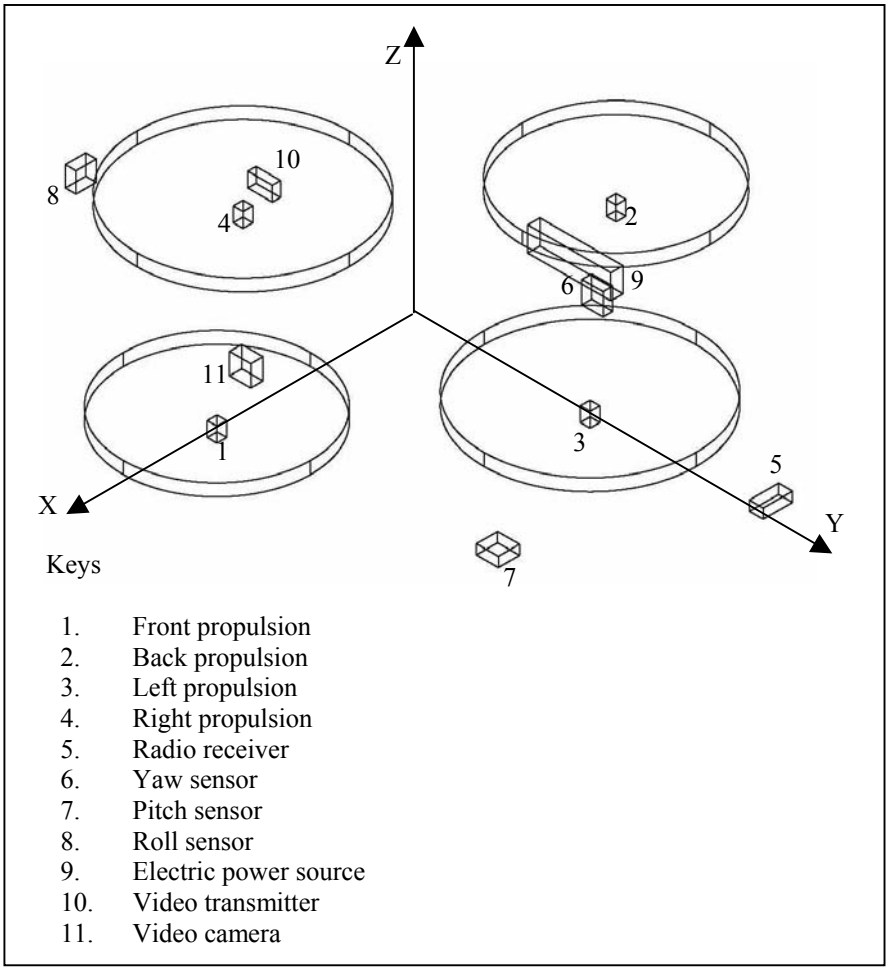

Figure 3.5. Layout obtained by optimization at first generation.

Table 3.6. Results of optimization constraints at first generation.

Constraints	Status
Overlapping regions	Fulfilled
Maximum Z boundary	Violated
Overall CG location	Violated
Inter-propeller distance	Fulfilled
Balanced yaw moment	Fulfilled
Minimum voltage and current of power source	Fulfilled
Lift-to-weight ratio	Violated
Minimum flight time	Fulfilled

After 523 generations, the design parameters have evolved to produce a feasible solution with no constraint being violated. Both pairs of propulsion sets are #4, whose propeller diameter is 23cm. The overall dimensions of the vehicle are tabulated in Table 3.7. From Figure 3.6, it can be seen that the components are still not organized in a very compact manner yet.

Table 3.7. Results of overall dimensions at 523rd generation.

Overall fuselage x dimension (m)	0.3320
Overall fuselage y dimension (m)	0.3700
Overall fuselage z dimension (m)	0.1160
Overall propellers' x dimension (m)	0.5500
Overall propellers' y dimension (m)	0.5880
Overall propellers' z dimension (m)	0.0150

At the 379928th generation (Figure 3.7), the design parameters have further evolved, with the most significant change in the propulstion sets from #4 to #3 which has a propeller diameter of 20cm. Table 3.8 shows the current overall dimensions.

Table 3.8. Results of overall dimensions at 379928th generation.

Overall fuselage x dimension (m)	0.4280
Overall fuselage y dimension (m)	0.2500
Overall fuselage z dimension (m)	0.0325
Overall propellers' x dimension (m)	0.6160
Overall propellers' y dimension (m)	0.4380
Overall propellers' z dimension (m)	0.0150

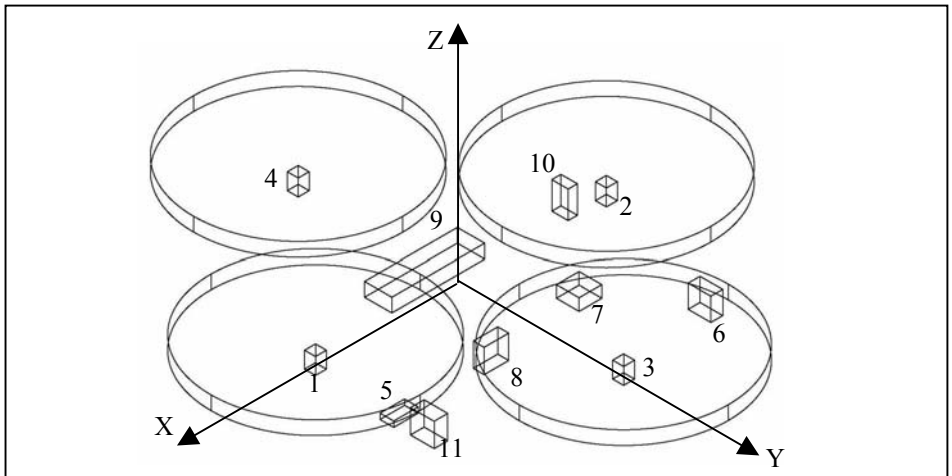

Keys

1. Front propulsion
2. Back propulsion
3. Left propulsion
4. Right propulsion
5. Radio receiver
6. Yaw sensor
7. Pitch sensor
8. Roll sensor
9. Electric power source
10. Video transmitter
11. Video camera

Figure 3.6. Layout obtained by optimization at 523rd generation

The final solution is obtained at the 380170th generation with all penalty functions ($h_{i=1\ to\ 11}$) equal to zero, and the final layout is shown in Figure 3.8. The corresponding overall dimensions are given in Table 3.9.

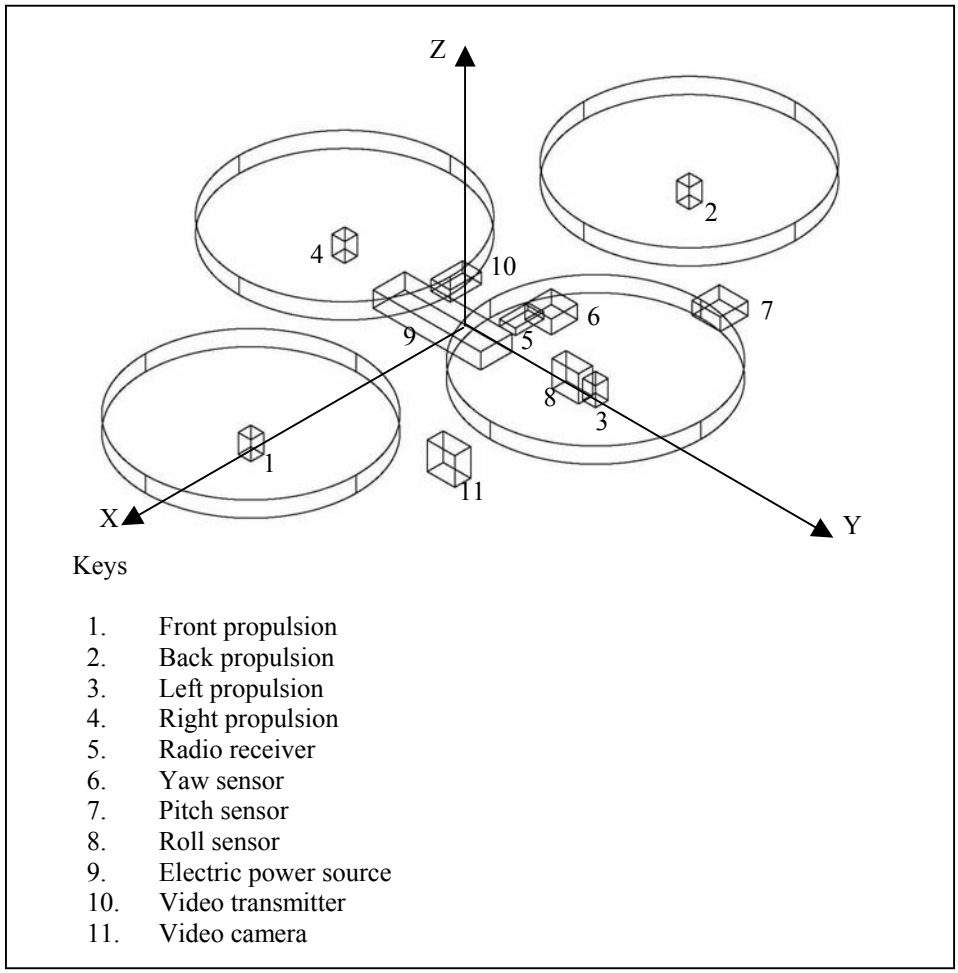

Keys

1. Front propulsion
2. Back propulsion
3. Left propulsion
4. Right propulsion
5. Radio receiver
6. Yaw sensor
7. Pitch sensor
8. Roll sensor
9. Electric power source
10. Video transmitter
11. Video camera

Figure 3.7. Layout obtained by optimization at 379928th generation.

Table 3.9. Final overall dimensions at 380170th generation.

Overall fuselage x dimension (m)	0.3760
Overall fuselage y dimension (m)	0.2220
Overall fuselage z dimension (m)	0.0285
Overall propellers' x dimension (m)	0.5640
Overall propellers' y dimension (m)	0.4100
Overall propellers' z dimension (m)	0.0150

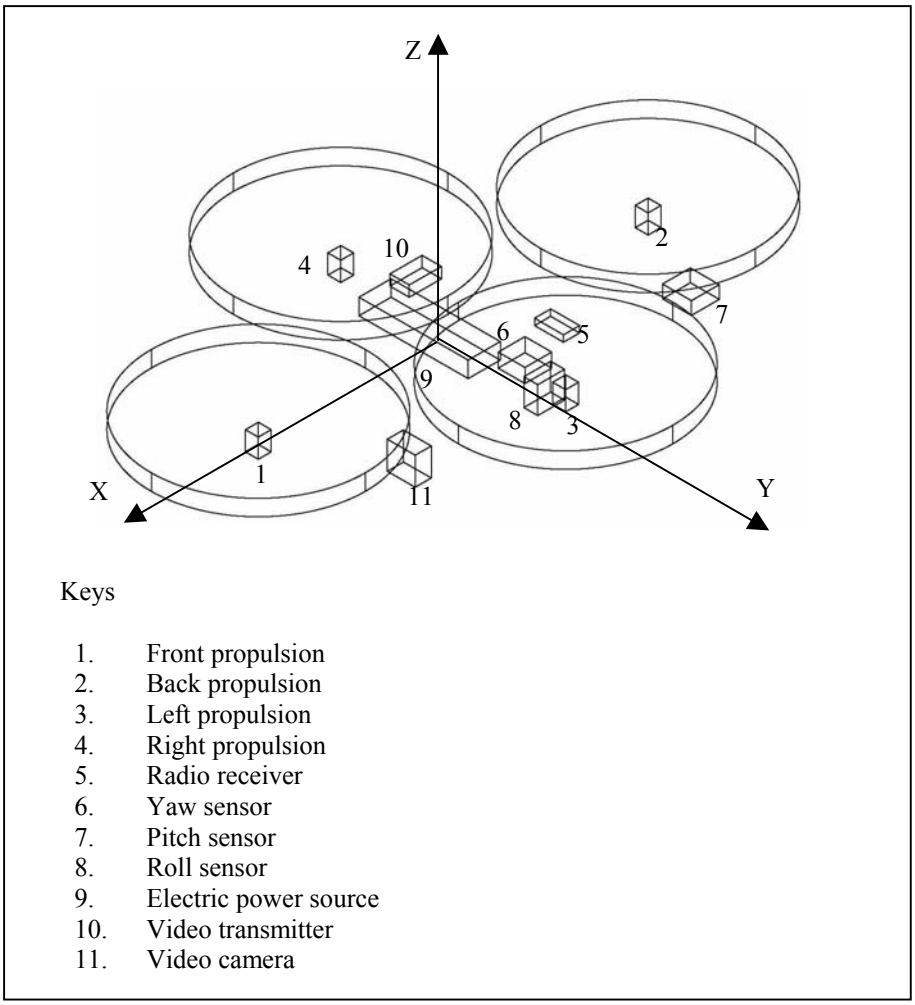

Figure 3.8. Final layout obtained at 380170th generation.

The final propulsion sets chosen are still #3, with each set contributing ¼ of the total required lift. It is interesting to note that set #1 which has the smallest propeller of the available choices, is not selected. This is because four #1 propulsion sets are not able to produce enough lift to support the total weight of the vehicle. It seems that though one pair of set #3 and one pair of set #1 are able to generate sufficient lift force, it is unfortunate that this combination is not able to cancel each other's reaction torques. This combination of components is able to

achieve a theoretical flight time of 1785 s. The final values of the design variables are tabulated in Table 3.10. The performace graph is shown in Figure 3.9

The electric power source selected is the heaviest battery #7 instead of the lightest battery #9. The quadrotor has four heavy identical propulsion sets, and the total mass is quite high. Thus, it needs to consume a very high current in order to generate the necessary lift. Battery #9 is unable to meet the current demand and is thus not chosen.

There is another very interesting observation. GA has managed to select the lighter radio receiver #1 instead of radio receiver #2. However, the pitch and yaw gyros selected are the heavier gyro #1 while the roll gyro is the lighter gyro #2. At first, this may appear to be a strange outcome, but a closer examination would help explain this mystery. The objective of the optimization program is to minimize the overall dimensions, without violating any of the eight specified constraints. By replacing the pitch and yaw gyros with a lighter gyro #2, it will not produce a more compact vehicle, and so there is no "motivation" for GA to change those particular design variables, since it has already accomplished its goal. In fact, if those variables were changed to the lighter gyro #2 and their location variables are not changed appropriately, the CG location constraint will be violated.

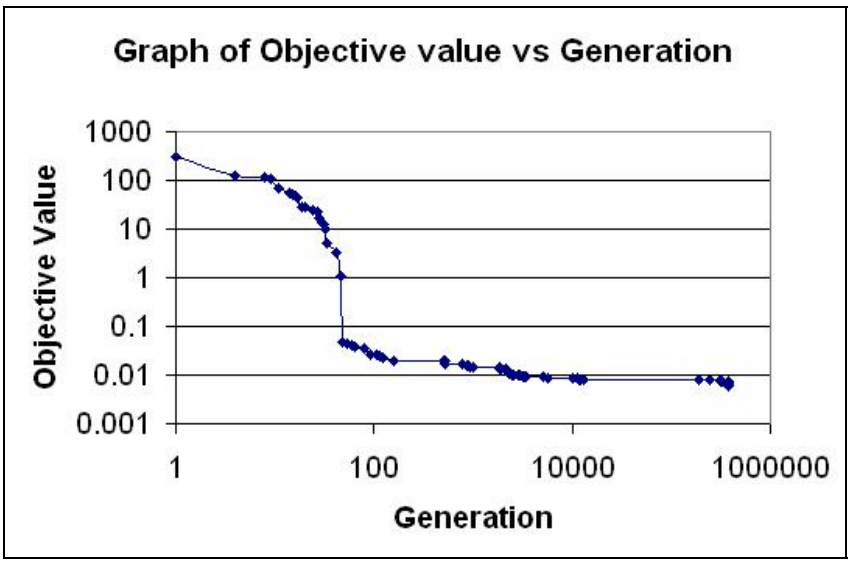

Figure 3.9. Objective value vs generation performance graph.

Another possible reason is that the extra mass incurred by having two heavier gyros is only 0.008 kg which is not very significant considering that the quadrotor is able to provide ample lift force. The computational time to obtain the final solution is only 2965 s.

Table 3.10. Table of final variable values (quadrotor design).

	Variable Name	Values
1.	Front/back propulsion choice	3
2.	Left/right propulsion choice	3
3.	Front motor orientation	2
4.	Back motor orientation	1
5.	Left motor orientation	1
6.	Right motor orientation	1
7.	Front propulsion x position (m)	0.182
8.	Left propulsion y position (m)	0.105
9.	Front/back propulsion percentage usage of maximum allowable current	0.672
10.	Left/right propulsion percentage usage of maximum allowable current	0.689
11.	Radio receiver choice	1
12.	Radio receiver mounting plane	1

13.	Radio receiver orientation	1
14.	Radio receiver x position (m)	-0.047
15.	Radio receiver y position (m)	0.050
16.	Radio receiver z position (m)	0.013
17.	Pitch rate sensor choice	1
18.	Pitch rate sensor mounting plane	1
19.	Pitch rate sensor x position (m)	-0.019
20.	Pitch rate sensor y position (m)	0.048
21.	Pitch rate sensor z position (m)	-0.002
22.	Roll rate sensor choice	2
23.	Roll rate sensor mounting plane	1
24.	Roll rate sensor x position (m)	-0.153
25.	Roll rate sensor y position (m)	0.069
26.	Roll rate sensor z position (m)	-0.003
27.	Yaw rate sensor choice	1
28.	Yaw rate sensor orientation	2
29.	Yaw rate sensor x position (m)	0.000
30.	Yaw rate sensor y position (m)	0.085
31.	Yaw rate sensor z position (m)	0.003
32.	Electric power source choice	7
33.	Electric power source mounting plane	3
34.	Electric power source orientation	2
35.	Electric power source x position (m)	-0.001
36.	Electric power source y position (m)	-0.023
37.	Electric power source z position (m)	-0.003
38.	Video transmitter mounting plane	1
39.	Video transmitter orientation	2
40.	Video transmitter x position (m)	-0.038
41.	Video transmitter y position (m)	-0.073
42.	Video transmitter z position (m)	-0.004
43.	Video camera x position (m)	0.121
44.	Video camera y position (m)	0.080
45.	Video camera z position (m)	0.004

Table 3.11 shows the comparison between the final quadrotor obtained with a commercial quadrotor called Draganflyer. It is clear that the final quadrotor obtained is lighter, more compact and has a longer flight time compared to the quadrotor available commercially.

Table 3.11. Comparison of final quadrotor and Draganflyer.

Attributes	Quadrotor	Draganflyer
Overall fuselage x dimension (m)	0.3760	0.5000
Overall fuselage y dimension (m)	0.2220	0.5000
Overall fuselage z dimension (m)	0.0285	0.1350
Overall fuselage volume (m^3)	2.38×10^{-3}	3.38×10^{-2}
Overall propellers' x dimension (m)	0.5640	0.8000
Overall propellers' y dimension (m)	0.4100	0.8000
Overall propellers' z dimension (m)	0.0150	0.0150
Overall propeller volume (m^3)	3.47×10^{-3}	9.60×10^{-3}
Total volume (m^3)	5.85×10^{-3}	4.34×10^{-2}
Mass (kg)	0.22197	0.53865
Flight time (s)	1785	720

3.4.1 Parallel computation results

In this section, an investigation is carried out to assess the performance of a parallel GA implementation of the design process. Since GA has an element of randomness in its performance, the comparison between the serial GA and parallel GA will be carried out by repeating the optimization process 20 times. For the single machine, the GA population size is 200, while the parallel GA on 4 PCs will each have a subpopulation of size 50. The migration generation is set as 50. The optmization process will terminate if the improvement in the objective value is less than 0.5% for consecutively 5000 generations.

The average time taken for the serial GA to compute one generation is 0.040 s while the parallel GA takes an average time of 0.0098 s to complete one generation. From Table 3.12, the average time for convergence in the single machine's case is 424497 x 0.040 s = 16980 s, while the average time for convergence in the parallel GA's case is 443642 x 0.0098 s = 4348 s. Therefore, one can expect an average speedup of 16980/4348 = 3.9 for convergence to occur

when the parallel GA is used. Comparing the quality of the converged values, the average parallel GA result is better than the single machine average result by 0.5 %.

Table 3.12. Comparison of converged results between single machine GA and parallel GA for 20 runs.

Run	Single machine		4-node cluster	
	Converged value	Generation of convergence	Converged value	Generation of convergence
1	6.022E-03	449020	6.463E-03	428300
2	5.848E-03	413440	6.411E-03	447800
3	5.972E-03	408900	5.848E-03	416900
4	6.411E-03	435755	6.560E-03	432400
5	6.022E-03	403852	6.213E-03	443870
6	5.972E-03	435214	5.972E-03	439560
7	6.560E-03	428770	6.213E-03	423460
8	6.941E-03	394530	6.022E-03	450100
9	5.972E-03	410250	5.972E-03	449680
10	6.748E-03	437980	6.213E-03	452430
11	6.619E-03	419630	5.922E-03	442800
12	6.463E-03	419800	6.022E-03	437580
13	5.848E-03	439300	6.463E-03	446730
14	6.022E-03	406000	6.560E-03	452870
15	5.972E-03	418200	5.972E-03	445320
16	6.213E-03	454300	6.294E-03	460100
17	6.463E-03	436900	6.213E-03	447400
18	5.972E-03	424700	6.022E-03	452130
19	6.560E-03	419600	6.619E-03	446210
20	6.411E-03	433800	6.411E-03	457200
Average=	6.251E-03	424497	6.219E-03	443642

4. Design Optimization of an Asymmetrical Quadrotor UAV/MAV (JQUAD-rotor)

In Chapter 3, it is recognized that the quadrotor UAV/MAV is a configuration that is easier to fabricate compared to the traditional single main and tail rotor and other configurations that use the swash plate and linkages for control, especially evident for small-scale UAV and MAV. In this chapter, a new unconventional rotary-wing UAV/MAV design is presented to demonstrate its feasibility in producing flight vehicles that are as easy to fabricate as the quadrotor UAV/MAV, and can be even smaller than the quadrotor configuration, given the availability of same component products to choose from. This new design has not been attempted and its optimization has not been carried out before.

4.1 Design Outline

The proposed configuration uses four rotors, same as the conventional quadrotor, but they are not arranged in symmetry (refer to Figure 4.1). The proposed configuration is named "JQUAD-rotor" because it is shaped like the letter 'J' when viewed from below.

Quadrotor requires two pairs of oppositely-rotating rotors/propellers. The counter-rotating rotor/propeller is not commercially available in small size (especially for diameter of six inches and below). This poses a difficulty in designing small-scale UAV or MAV using the quadrotor configuration, often resulting in significant cost and time consumed in fabricating the small counter-rotating rotor/propeller. The JQUAD-rotor does not have this problem because all four rotors/propellers can be

of same rotational direction (as shown in Figure 4.1) and they are readily available in small size, even as small as 6 cm in diameter.

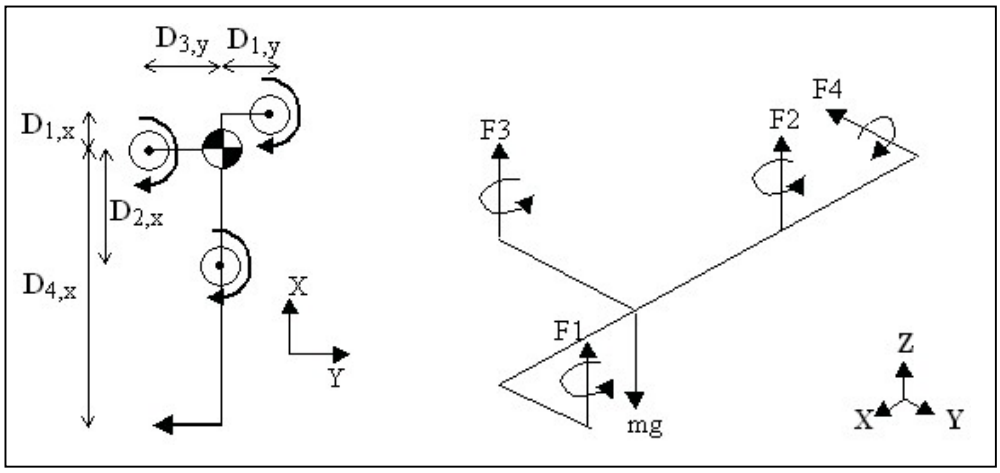

Figure 4.1. Proposed JQUAD-rotor configuration layout.

In the original quadrotor, there are either four identical motor/propeller systems or two pairs of identical motor/propeller systems. This restriction may result in a rotary-wing vehicle that is unnecessarily larger and heavier than other non-quadrotor configurations. The JQUAD-rotor uses one main motor/propeller system (F1) that is responsible for producing the majority of the lift required for it to become airborne and also for altitude control. Three other smaller motor/propeller systems connected via three off-the-shelf gyros, are used to provide the roll (F3), pitch (F2) and yaw (F4) control for steering the vehicle forward/backward and sideward. The rotor that is in charge of yaw control functions in the same way as the tail rotor of the single main and tail rotor configuration. Figure 4.2 compares the x and y dimensions of a typical quadrotor with the proposed JQUAD-rotor, for both cases where staggering of propellers is

allowed and not allowed. It is apparent that the JQUAD-rotor has a more compact layout than the quadrotor.

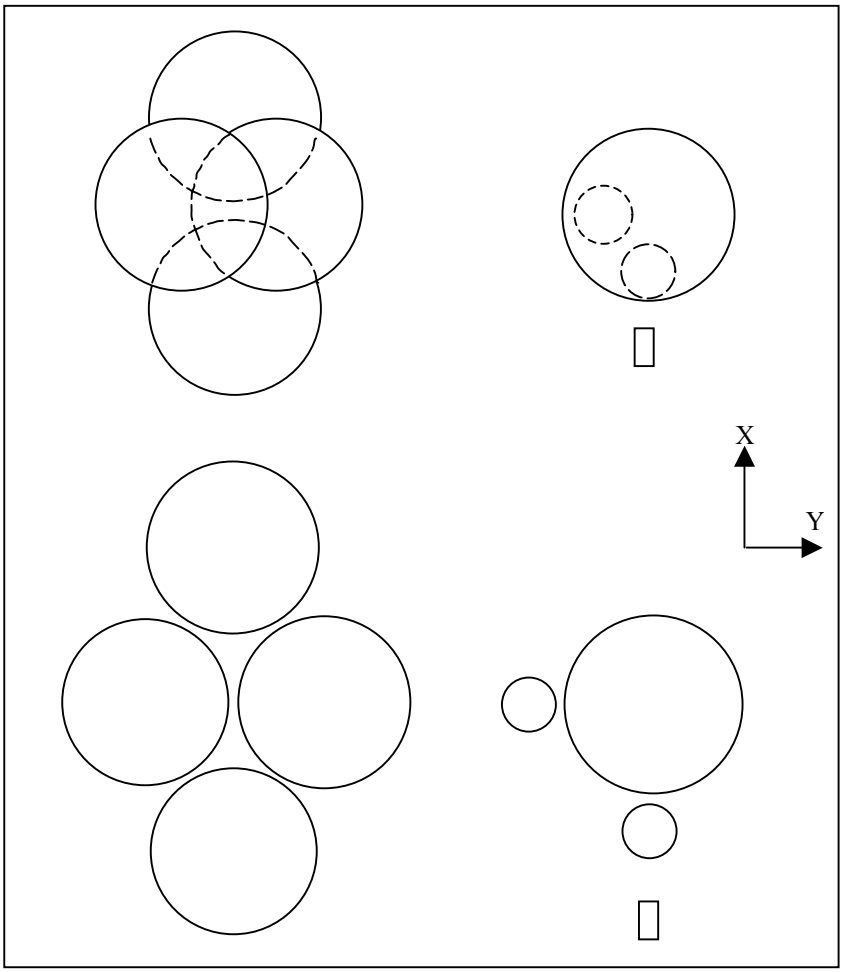

Figure 4.2. Comparison of length and width dimensions between quadrotor and JQUAD-rotor.

The next attractive attribute of the JQUAD-rotor is that it is easier to control than the traditional quadrotor. For the quadrotor, the ascending/descending requires a specialized altitude controller that causes the four rotors to increase/decrease thrust evenly, so that the net yaw moment remains zero. Altitude control for the JQUAD-rotor is simpler, as the remote pilot only needs to adjust the stick control of the radio transmitter corresponding to the main rotor without any additional specialized controller circuit.

In the case of roll or pitch control of quadrotor, one of the pair of rotating rotors has to increase speed while the other of the same pair decrease speed by the same amount to create an unbalanced moment to till the vehicle in the desired direction. The JQUAD-rotor can achieve its roll or pitch motion simply by adjusting only one corresponding stick-control on the radio transmitter. Yaw control for quadrotor is even more complex. The pair of similar rotating rotors must increase/decrease speed while the other pair decrease/increase their rotor speed. As for the JQUAD-rotor, yaw control is again performed simply by adjusting only one stick-control on the radio transmitter corresponding to the yaw rotor. The proposed flight vehicle can achieve airborne flight without the use of additional controller circuits designed for the roll, pitch, yaw motion and altitude control. Table 4.1 summarizes the main differences between the quadrotor and the proposed JQUAD-rotor configuration.

Table 4.1. Summary of main differences between proposed JQUAD-rotor and quadrotor.

Quadrotor	JQUAD-rotor
Either four identical motors/propellers or two pairs of identical motors/propellers	Three motors/propellers can be smaller than the main motor/propeller
Two pairs of oppositely-rotating propellers	All four propellers can have the same rotation direction
Roll, pitch, yaw and altitude stability and control requires four different specially designed controllers	Roll, pitch, yaw and altitude control can be simply performed with just three off-the-shelf gyros installed onboard
Symmetric layout	Asymmetric layout

4.2 Problem Formulation

In this section, a design methodology is introduced to automate the design of the proposed JQUAD-rotor. The goal is to investigate whether this unconventional configuration can be more compact than quadrotor, given the same range of component products to choose from. As in Chapter 2 and Chapter 3, the propulsion, sensors, radio receiver and other components are modeled as rectangular blocks. The dimensions, length L, breadth B and height H of each block are defined by the smallest rectangular box that can enclose the component completely.

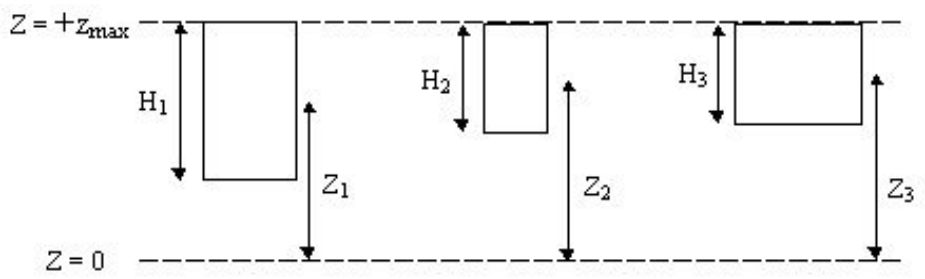

Figure 4.3. Z locations of the main, roll control and pitch control motors.

The design variables here are mostly same as the quadrotor design problem in Chapter 3, with a few exceptions. In this design problem, the main propulsion has a z location variable, Z_1, because the yaw rotor is fixed at z = 0, and there is a chance its radius may exceed the $+z_{max}$ plane. In case the yaw rotor does protrude the main rotor's plane, the optimization routine can set z_1 higher to clear the yaw rotor. However, there is no z location variable for the roll and pitch control propulsion as their rotors will flush with the main rotor (see Figure 4.3). Thus, their respective z location will be given by,

$$Z_2 = Z_1 + 0.5H_1 - 0.5H_2 \tag{4.1}$$

$$Z_3 = Z_1 + 0.5H_1 - 0.5H_3 \tag{4.2}$$

The positioning of the main, pitch control and yaw control in this design problem is a complicated task. The most obvious conflict is that if they are to be very compact, then the moment arm will be smaller, and this has to be compensated with a greater thrust to produce the necessary counter moments. In order to generate more thrust, the motors need to consume more current, and this may exceed the battery pack's maximum current output capability or resulting in a very short flight time.

The x and y location of the main propulsion should not be too high as this will cause the the roll and pitch control motors to use more current for generating more thrust to balance the roll and pitching moments due to main propulsion.

Alternatively, these have to be located further from the CG so that there is a longer moment arm to create the necessary counter moments. Therefore, this will make the overall dimensions of the vehicle larger. On the other hand, if the x and y location of the main propulsion is too small, then the roll and pitch motors may just have to produce a very small force to counter the unbalanced moments. This can create another problem, as the total summation of the three upward forces may be less than the downward weight. Therefore, GA will evolve these design parameters until the best consensus is achieved.

The roll control motor has no x location variable because it is fixed at x = 0, so that it will create strictly a roll moment and no pitch moment. It has also no y location variable because the y position will be such that it will counter the roll moment created by the main propulsion.

The pitch control motor has no y location variable because it is fixed at y = 0, so that it will create only a pitch moment and no roll moment. Simlarly, there is no x location variable for the pitch control motor because the x position will be such that it will counter any unbalanced pitch moment.

As for the yaw control motor, its z location is fixed at z = 0, so that it will generate only a yaw moment and no roll moment. It does not have x location variable as it will counterbalance the reaction torques of the main, pitch control and yaw control motors.

A new design variable, percentage of lift contribution by roll motor for the remaining required lift after main propulsion's contribution, P_{roll}, is also introduced here. The lift produced by the roll motor is

$$F3 = (\text{Total lift required} - F1) * P_{roll} \tag{4.3}$$

The main propulsion set with higher K_{thrust} is better as it produces more thrust with the same current consumption as another propulsion set of lower K_{thrust}. But, it will most likely have a larger propeller. Moreover, it will have a higher torque versus current constant K_{torque}, and this will require the yaw control motor to generate more counter torque either by consuming more current or having a larger moment arm (making the vehicle less compact).

The main propulsion, pitch control and roll control propulsion have only orientation variables and no mounting plane variable as they can only be mounted on its BL plane. The yaw control has only mounting plane variable and no orientation variable as it can only be mounted on its BH or HL plane with only one possible orientation which is its rotational axis parallel to Y-axis.

As in chapter 3 concerning the design of quadrotor UAV/MAV, the design problem is to minimize the overall dimensions of the vehicle's fuselage, $X_{fuselage}$, $Y_{fuselage}$ and $Z_{fuselage}$ (including that of yaw propeller) and the vehicle's propellers, $X_{propeller}$, $Y_{propeller}$ and $Z_{propeller}$ (only the main, pitch control and roll control propellers in this case).

Minimize

$$X_{fuselage} * Y_{fuselage} * Z_{fuselage} + X_{propeller} * Y_{propeller} * Z_{propeller} \quad (4.4)$$

subjected to the following constraints on

a) overlapped regions

b) maximum Z boundary

c) overall CG location

d) inter-propeller distance

e) balanced yaw moment

f) minimum voltage and current of power source

g) lift-to-weight ratio

h) minimum flight time

i) balanced pitch moment

j) balanced roll moment

4.3 Design Constraints

The first eight constraints are the same as those described in Chapter 2 and Chapter 3. The two additional constraints are related to balanced pitch and roll moments.

4.3.1 Balanced pitch and roll moment constraints

As mentioned in the previous chapter, the quadrotor by default will have balanced pitch and roll moments. In the case of JQUAD-rotor, the tasks of enforcing balanced yaw, pitch and roll moments during hovering are performed by the yaw,

pitch and roll control propulsions. Thus, the two additional constraints are defined as

$$\sum \text{Moment}_{\text{pitch}} = 0 \tag{4.5}$$

$$\sum \text{Moment}_{\text{roll}} = 0 \tag{4.6}$$

Instead of enforcing these equality constraints, a small tolerance δ can be allowed by the designer

$$\left|\sum \text{Moment}_{\text{pitch}}\right| < \delta \tag{4.7}$$

$$\left|\sum \text{Moment}_{\text{roll}}\right| < \delta \tag{4.8}$$

If these constraints are violated, the penalty values are given by

$$h_{12} = \left|\sum \text{Moment}_{\text{pitch}}\right| - \delta \tag{4.9}$$

$$h_{13} = \left|\sum \text{Moment}_{\text{roll}}\right| - \delta \tag{4.10}$$

For the design problem, the goal is obtain the smallest possible overall vehicle volume. The objective function in the GA optimization problem is defined as

$$\text{minimize } f = \sum_{i=1}^{13} \sigma_i h_i + \sigma_{14} (X_{\text{fuselage}} * Y_{\text{fuselage}} * Z_{\text{fuselage}} + X_{\text{propeller}} * Y_{\text{propeller}} * Z_{\text{propeller}}) \tag{4.11}$$

where $h_{i=1 \text{ to } 13}$ are the penalty functions defined for the constraints, and $\sigma_{i=1 \text{ to } 14}$ are the weighing factors tabulated Table 4.2.

Table 4.2 Table of weighing factors.

Weighing factors	Value
σ_1	9.9979×10^{-4}
σ_2	9.9979×10
σ_3	9.9979×10^{-4}
σ_4	9.9979×10^{-4}
σ_5	9.9979×10^{-4}
σ_6	9.9979×10^{-4}
σ_7	9.9979×10^{-4}
σ_8	9.9979×10^{-4}
σ_9	9.9979×10^{-4}
σ_{10}	9.9979×10^{-3}
σ_{11}	9.9979×10^{-4}
σ_{12}	9.9979×10^{-4}
σ_{13}	9.9979×10^{-4}
σ_{14}	9.9979×10^{-7}

There are altogether 50 design variables in this problem, five more than the previous quadrotor design problem, consisting of 22 integer variables and 28 float number variables, whose lower and upper bounds are shown in Table 4.3. Refer to Tables 3.2-3.4 for the available components' technical specifications.

Table 4.3. Table of design variables and corresponding bounds (JQUAD-rotor).

	Variable Name	Lower Bound	Upper Bound
1.	Main propulsion choice	1	7
2.	Main propulsion orientation	1	2
3.	Main propulsion x position (m)	0.001	0.060
4.	Main propulsion y position (m)	0.001	0.060
5.	Main propulsion z position (m)	0.000	0.030
6.	Main propulsion percentage usage of maximum allowable current	0.020	0.980
7.	Pitch control propulsion choice	1	7
8.	Pitch control orientation	1	2
9.	Roll control propulsion choice	1	7
10.	Roll control orientation	1	2
11.	Contribution of roll control propulsion on remaining lift after main propulsion ‘s contribution	0.100	0.990
12.	Yaw control propulsion choice	1	7
13.	Yaw control mounting plane	2	3
14.	Yaw control propulsion y position (m)	-0.500	0.500
15.	Yaw control propulsion percentage usage of maximum allowable current	0.010	0.900
16.	Radio receiver choice	1	2
17.	Radio receiver mounting plane	1	3
18.	Radio receiver orientation	1	2
19.	Radio receiver x position (m)	-0.500	0.500
20.	Radio receiver y position (m)	-0.500	0.500
21.	Radio receiver z position (m)	-0.500	0.500
22.	Pitch rate sensor choice	1	2
23.	Pitch rate sensor mounting plane	1	2
24.	Pitch rate sensor x position (m)	-0.500	0.500
25.	Pitch rate sensor y position (m)	-0.500	0.500
26.	Pitch rate sensor z position (m)	-0.500	0.500
27.	Roll rate sensor choice	1	2
28.	Roll rate sensor mounting plane	1	2
29.	Roll rate sensor x position (m)	-0.500	0.500
30.	Roll rate sensor y position (m)	-0.500	0.500
31.	Roll rate sensor z position (m)	-0.500	0.500
32.	Yaw rate sensor choice	1	2
33.	Yaw rate sensor orientation	1	2
34.	Yaw rate sensor x position (m)	-0.500	0.500
35.	Yaw rate sensor y position (m)	-0.500	0.500
36.	Yaw rate sensor z position (m)	-0.500	0.500
37.	Electric power source choice	1	9
38.	Electric power source mounting plane	1	3

39.	Electric power source orientation	1	2
40.	Electric power source x position (m)	-0.500	0.500
41.	Electric power source y position (m)	-0.500	0.500
42.	Electric power source z position (m)	-0.500	0.500
43.	Video transmitter mounting plane	1	3
44.	Video transmitter orientation	1	2
45.	Video transmitter x position (m)	-0.500	0.500
46.	Video transmitter y position (m)	-0.500	0.500
47.	Video transmitter z position (m)	-0.500	0.500
48.	Video camera x position (m)	-0.500	0.500
49.	Video camera y position (m)	-0.500	0.500
50.	Video camera z position (m)	-0.500	0.500

4.4 Optimization Results

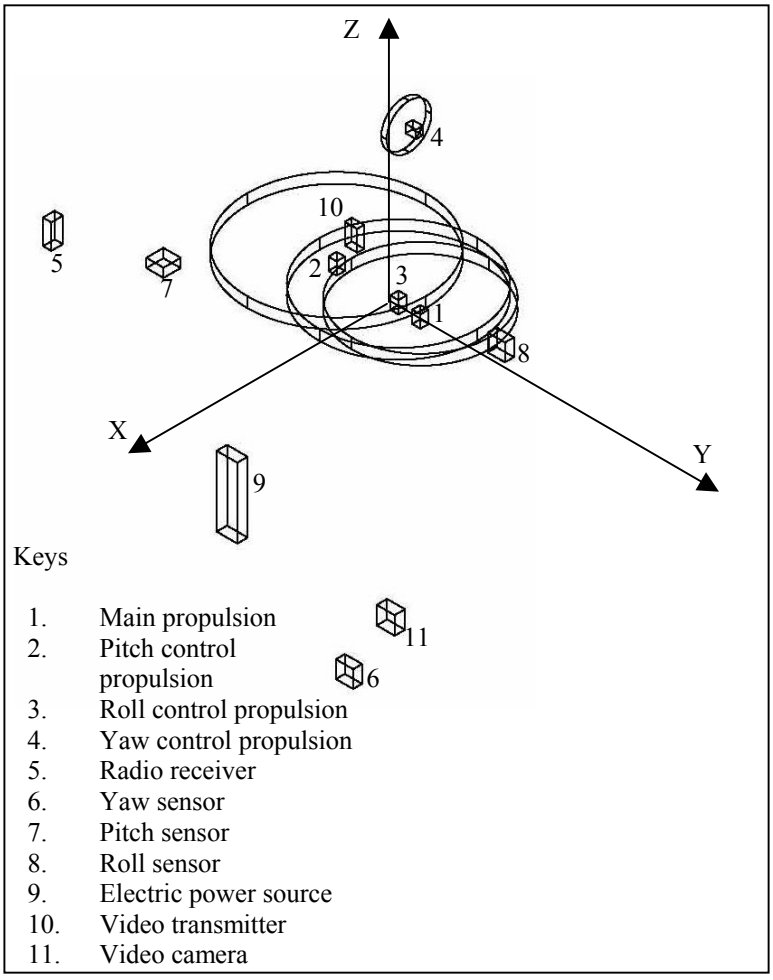

Figure 4.4. Layout obtained by optimization at first generation.

At the first generation, the optimization program has selected the propulsion set with the smallest propeller of 6.5 cm for yaw control. The pitch control propeller is 23cm and roll control propeller is 26cm, both larger than the main propulsion propeller of 20 cm. At this stage, the main, pitch and roll control propulsion are concentrated near the origin (Figure 4.4) and four out of the design ten constraints are violated and given in Table 4.4.

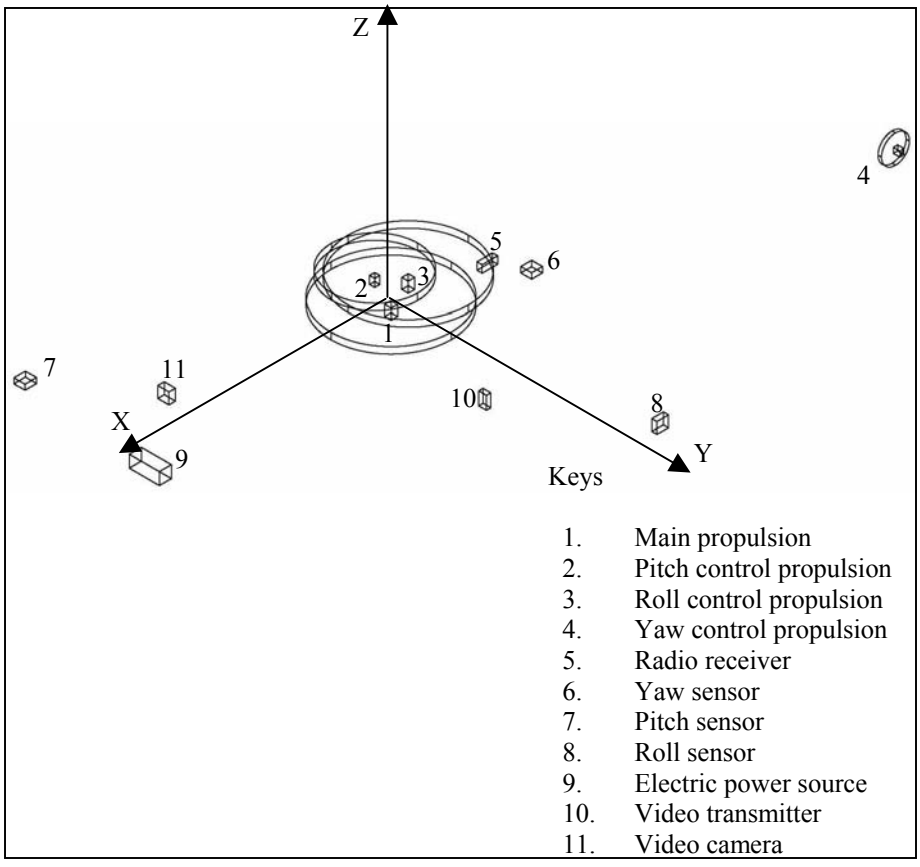

Figure 4.5. Layout obtained by optimization at seventh generation.

At the seventh generation, there is already some marked improvement. The main propulsion has changed to the largest propeller of diameter 28cm. The pitch control

propulsion propeller is also 28cm in diameter. The roll control propeller diameter has decreased from 26cm to 20cm. This combination of propulsion sets has allowed the vehicle to generate enough upward lift to overcome its downward weight. From Figure 4.5, the main, pitch and roll control motors are still clustered together but now only two out of ten design constraints are violated (Table 4.5). The main, pitch control and roll control propellers are constrainted by the minimum inter-propeller distance constraint instead of the constraint on overlapping regions. Thus, the latter constraint has not been violated.

After 13102 generations, the optimization process has evolved even more significantly. The pitch and roll control propulsion sets now have the smallest propeller diameter of 6.5 cm. The main, pitch and roll control motors are no longer cluttered together, with sufficient clearance between the propellers as shown in Figure 4.6. However, two out of the ten design constraints still have not been fulfilled (Table 4.6).

Table 4.4. Results of optimization constraints at first generation.

Constraints	Status
Overlapping regions	Fulfilled
Maximum Z boundary	Violated
Overall CG location	Violated
Inter-propeller distance	Violated
Balanced yaw moment	Fulfilled
Balanced pitch moment	Fulfilled
Balanced roll moment	Fulfilled
Minimum voltage and current of power source	Fulfilled
Lift-to-weight ratio	Violated
Minimum flight time	Fulfilled

Table 4.5. Results of optimization constraints at seventh generation.

Constraints	Status
Overlapping regions	Fulfilled
Maximum Z boundary	Fulfilled
Overall CG location	Violated
Inter-propeller distance	Violated
Balanced yaw moment	Fulfilled
Balanced pitch moment	Fulfilled
Balanced roll moment	Fulfilled
Minimum voltage and current of power source	Fulfilled
Lift-to-weight ratio	Fulfilled
Minimum flight time	Fulfilled

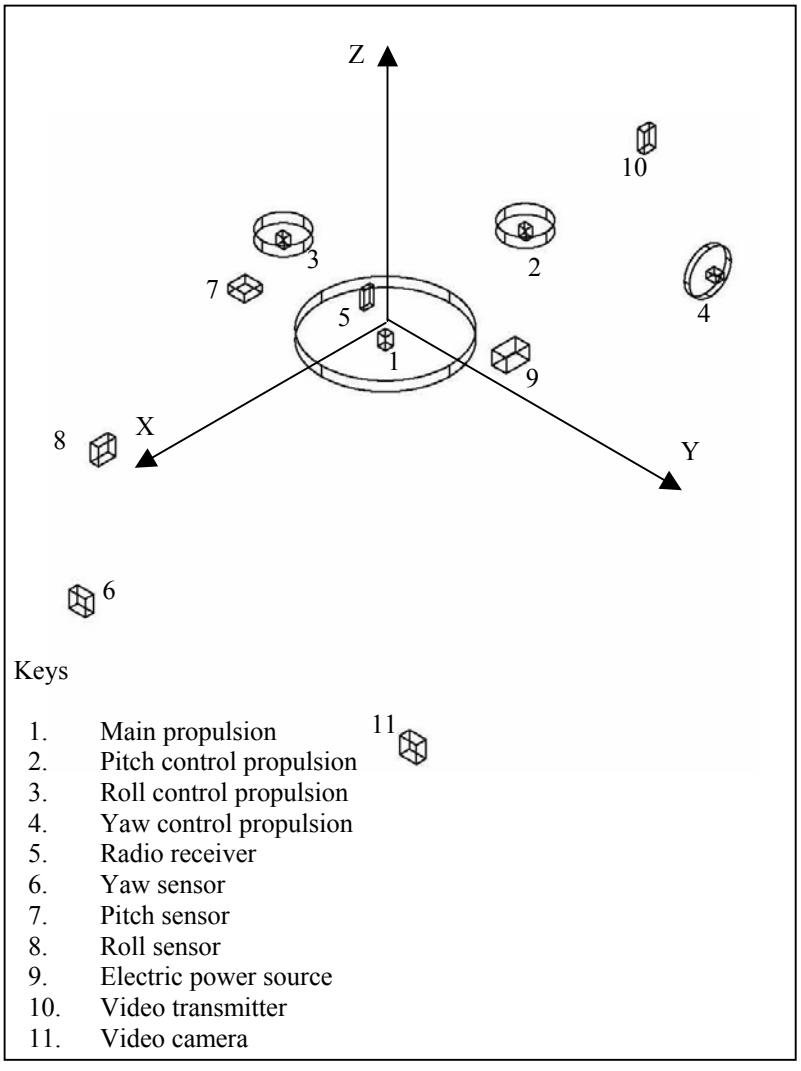

Figure 4.6. Layout obtained by optimization at 13102th generation.

Table 4.6. Results of optimization constraints at 13102th generation.

Constraints	Status
Overlapping regions	Fulfilled
Maximum Z boundary	Fulfilled
Overall CG location	Violated
Inter-propeller distance	Fulfilled
Balanced yaw moment	Fulfilled
Balanced pitch moment	Fulfilled
Balanced roll moment	Fulfilled
Minimum voltage and current of power source	Fulfilled
Lift-to-weight ratio	Violated
Minimum flight time	Fulfilled

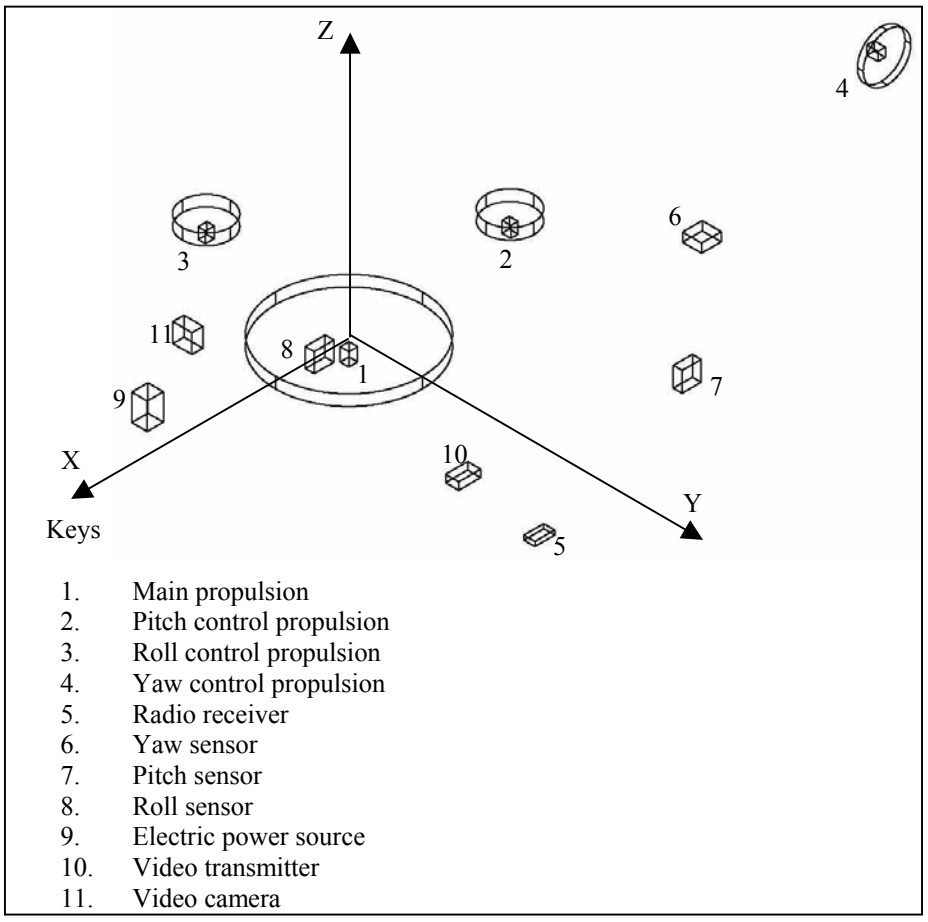

Figure 4.7. Layout obtained by optimization at 201559th generation.

At the 201559th generation, the two unresolved design constraints are now finally satisfied, establishing the first feasible solution. However, there is definitely room

for improvement as the components are widely spread, as shown in Figure 4.7, especially the yaw propulsion. The overall dimensions are given in Table 4.7.

Table 4.7. Results of overall dimensions at 201559th generation.

Overall fuselage x dimension (m)	0.9565
Overall fuselage y dimension (m)	0.5775
Overall fuselage z dimension (m)	0.1205
Overall propellers' x dimension (m)	0.3915
Overall propellers' y dimension (m)	0.3725
Overall propellers' z dimension (m)	0.0150

Table 4.8. Final overall dimensions at 877994th generation.

Overall fuselage x dimension (m)	0.2465
Overall fuselage y dimension (m)	0.2150
Overall fuselage z dimension (m)	0.0655
Overall propellers' x dimension (m)	0.3615
Overall propellers' y dimension (m)	0.3365
Overall propellers' z dimension (m)	0.0150

At the 877994th generation, the final layout is obtained with all penalty functions ($h_{i=1 \text{ to } 13}$) equal to zero. Figure 4.8 shows that the majority of the components are concentrated near the origin in order to achieve the desired CG at the origin (refer Table 4.8 for the overall dimensions). The main propulsion chosen has the second smallest propeller of 20 cm, while the roll, pitch and yaw control propellers are the smallest with 6.5 cm. Obviously, the main propeller is not the smallest because that propulsion set is not able to contribute to the bulk of the total lift required.

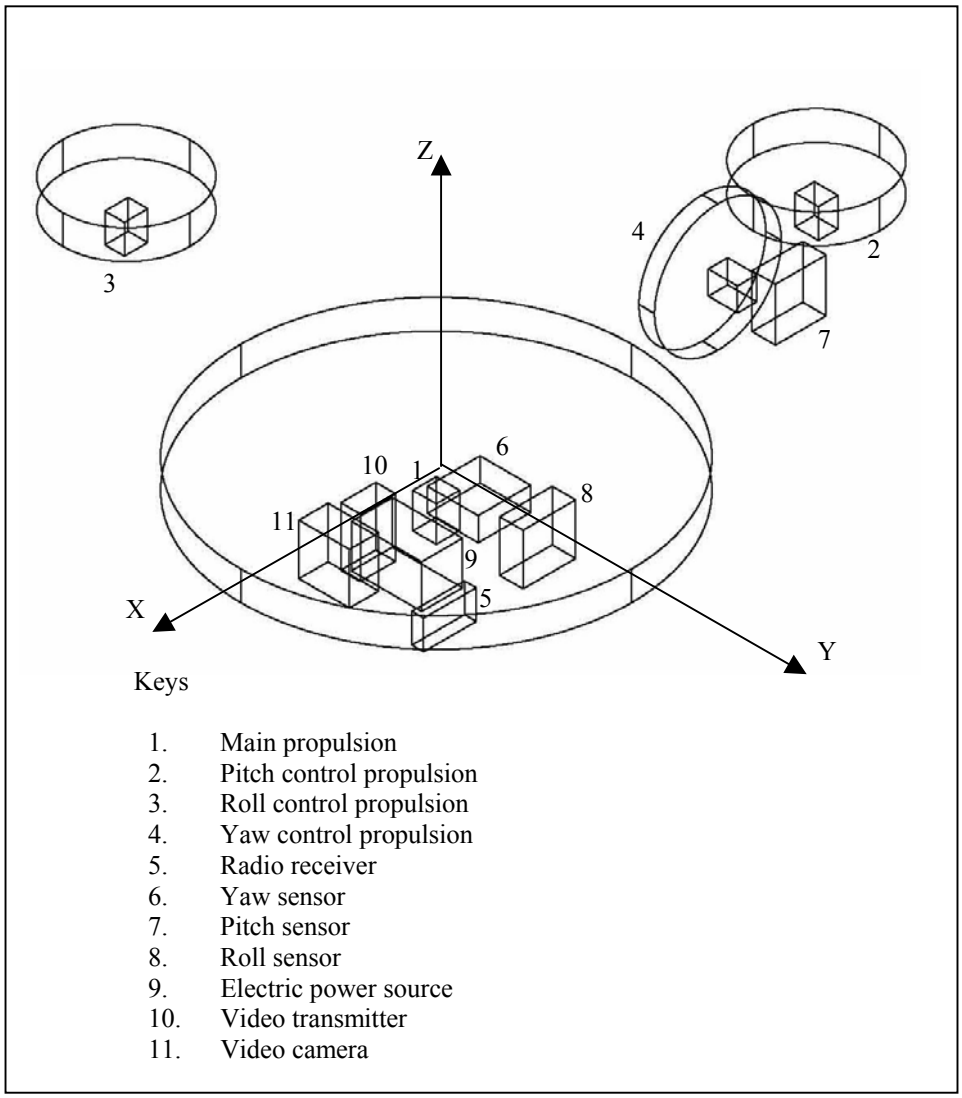

Figure 4.8. Final layout obtained by optimization at 877994th generation.

The final values of the design variables are tabulated in Table 4.9. Figure 4.9 shows the performance graph of objective value with GA generations. The total mass of flight vehicle is only 0.11508 kg (inclusive of safety factor) and the achievable flight time is 395 s. The computational time taken is 8901 s.

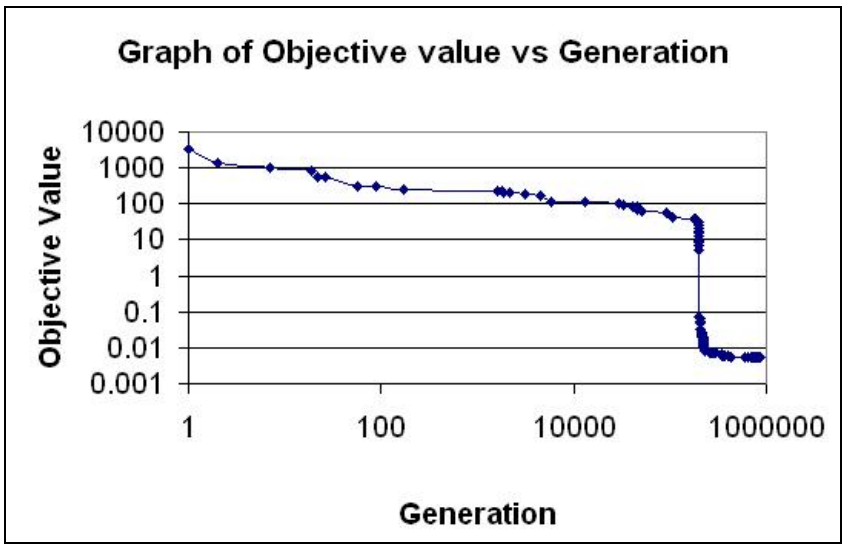

Figure 4.9. Objective value vs generation performance graph (JQUAD-rotor design).

In Chapter 2, the design problem of obtaining a compact configuration given only one set of components, using 34 design variables subjected to four design constraints took 1259 generations to converge. In Chapter 3, with the introduction of component selection variables, the quadrotor design optimization took a longer time to converge at 380170 generations. This is expected since the design problem is more complex, with 45 design variables and eight design constraints. The JQUAD-rotor design took the longest time to converge due to the highest number of design variables and constraints.

The final radio receiver selected was the smaller and lighter radio receiver #1. In this design problem, all the three gyros selected were the lighter gyro #2. This is not by accident, but because the total lift output is not as much as the quadrotor, and thus, GA has ensured that all the components are as light as possible.

Table 4.9. Table of final variable values (JQUAD-rotor design).

	Variable Name	Values
1.	Main propulsion choice	3
2.	Main propulsion orientation	1
3.	Main propulsion x position (m)	0.045
4.	Main propulsion y position (m)	0.034
5.	Main propulsion z position (m)	0.024
6.	Main propulsion percentage usage of maximum allowable current	0.906
7.	Pitch control propulsion choice	1
8.	Pitch control orientation	1
9.	Roll control propulsion choice	1
10.	Roll control orientation	2
11.	Contribution of roll control propulsion on remaining lift after main propulsion ‘s contribution	0.500
12.	Yaw control propulsion choice	1
13.	Yaw control mounting plane	2
14.	Yaw control propulsion y position (m)	-0.014
15.	Yaw control propulsion percentage usage of maximum allowable current	0.855
16.	Radio receiver choice	1
17.	Radio receiver mounting plane	3
18.	Radio receiver orientation	2
19.	Radio receiver x position (m)	0.041
20.	Radio receiver y position (m)	0.034
21.	Radio receiver z position (m)	-0.025
22.	Pitch rate sensor choice	2
23.	Pitch rate sensor mounting plane	1
24.	Pitch rate sensor x position (m)	-0.018
25.	Pitch rate sensor y position (m)	-0.007
26.	Pitch rate sensor z position (m)	-0.023
27.	Roll rate sensor choice	2
28.	Roll rate sensor mounting plane	2
29.	Roll rate sensor x position (m)	-0.155
30.	Roll rate sensor y position (m)	0.015
31.	Roll rate sensor z position (m)	0.011
32.	Yaw rate sensor choice	2
33.	Yaw rate sensor orientation	2
34.	Yaw rate sensor x position (m)	-0.009
35.	Yaw rate sensor y position (m)	0.032
36.	Yaw rate sensor z position (m)	-0.016
37.	Electric power source choice	9
38.	Electric power source mounting plane	1

39.	Electric power source orientation	1
40.	Electric power source x position (m)	0.047
41.	Electric power source y position (m)	0.021
42.	Electric power source z position (m)	-0.001
43.	Video transmitter mounting plane	2
44.	Video transmitter orientation	2
45.	Video transmitter x position (m)	0.033
46.	Video transmitter y position (m)	-0.013
47.	Video transmitter z position (m)	-0.015
48.	Video camera x position (m)	0.050
49.	Video camera y position (m)	-0.011
50.	Video camera z position (m)	-0.016

4.4.1 Comparison of quadrotor and JQUAD-rotor results

A comparison of the quadrotor and JQUAD-rotor reveals that in the former case, the electric power source selected is the heaviest battery #7 while the latter is the lightest #9. This shows that the proposed JQUAD-rotor design is able to consume less current that the quadrotor configuration. From Table 4.10, it can be seen that the flight time of quadrotor is very much longer than JQUAD-rotor. This is understandable because the design problem is constructed to make the vehicle as compact as possible. As a result, the JQUAD-rotor chooses the lightest battery #9 which does not have a high capacity.

All the JQUAD-rotor's overall dimensions are smaller than the quadrotor's except for the fuselage z dimension. The z dimension of the JQUAD-rotor is greater than the quadrotor due to the yaw control propeller which is not present in the latter. If a propulsion set with smaller propeller is available, then it is likely that this z dimension can be further reduced.

The total overall volumes of the two different vehicles confirmed that the proposed JQUAD-rotor is more compact than the quadrotor for the vehicle volume minmization problem. The strategy of using one main powerful propulsion for lift support and three smaller ones for pitch, roll and yaw control has yielded a lighter and more compact rotary-wing UAV/MAV. Therefore, for applications where weight and compactness is of greater concern than flight time, the JQUAD-rotor is a better choice than quadrotor, e.g. for infantry combat soldiers. Another possible application that requires a more compact flight vehicle is for use in urban environment where there are many buildings in close proximity or for maneuvering around narrow passageways.

Table 4.10. Comparison of final quadrotor and JQUAD-rotor results.

Attributes	Quadrotor	JQUAD-rotor
Overall fuselage x dimension (m)	0.3760	0.2465
Overall fuselage y dimension (m)	0.2220	0.2150
Overall fuselage z dimension (m)	0.0285	0.0655
Overall fuselage volume (m^3)	2.38×10^{-3}	3.47×10^{-3}
Overall propellers' x dimension (m)	0.5640	0.3615
Overall propellers' y dimension (m)	0.4100	0.3365
Overall propellers' z dimension (m)	0.0150	0.0150
Overall propeller volume (m^3)	3.47×10^{-3}	1.82×10^{-3}
Total volume (m^3)	5.85×10^{-3}	5.29×10^{-3}
Mass (kg)	0.22197	0.11508
Flight time (s)	1785	395

4.4.2 Parallel computation results

Similar to Sections 2.4.1 and 3.4.1, an investigation is carried out to assess the performance of a parallel GA implementation of the design process. The comparison between the serial GA and parallel GA will be carried out by repeating the optimization process 20 times. For the single machine, the GA population size is 200, while the parallel GA on 4 PCs will each have a subpopulation of size 50. The migration generation is set as 50. The optmization process will terminate if the improvement in the objective value is less than 0.5% for consecutively 5000 generations.

The average time taken for the serial GA to compute one generation is 0.045 s while the parallel GA takes an average time of 0.013 s to complete one generation. From Table 4.11, the average time for convergence in the single machine's case is 855054 x 0.045 s = 38477 s, while the average time for convergence in the parallel GA's case is 958159 x 0.013 s = 12456 s. Therefore, one can expect an average speedup of 38477/12456 = 3.1 for convergence to occur when the parallel GA is used. In this design problem, the average parallel GA result is higher than the single machine average result by 1.7 %.

Table 4.11. Comparison of converged results between single machine GA and parallel GA for 20 runs.

Run	Single machine		4-node cluster	
	Converged value	Generation of convergence	Converged value	Generation of convergence
1	5.310E-03	902994	6.133E-03	973580
2	5.912E-03	797950	5.711E-03	943740
3	6.018E-03	812500	5.947E-03	895400
4	5.296E-03	828900	5.985E-03	986870
5	5.876E-03	865400	5.296E-03	913780
6	5.585E-03	921370	5.791E-03	962320
7	6.133E-03	763120	6.018E-03	998500
8	5.791E-03	858370	5.912E-03	971421
9	5.841E-03	904960	5.676E-03	958375
10	5.296E-03	847480	5.876E-03	883200
11	5.985E-03	870140	5.296E-03	946450
12	5.535E-03	814580	5.912E-03	983478
13	5.791E-03	906310	6.133E-03	956875
14	5.711E-03	841090	5.947E-03	973878
15	5.296E-03	884750	6.052E-03	990680
16	6.052E-03	804300	5.912E-03	946870
17	5.947E-03	855420	5.985E-03	996382
18	5.676E-03	876980	5.791E-03	948657
19	5.985E-03	832470	5.535E-03	986598
20	6.052E-03	912000	6.179E-03	946127
Average=	5.754E-03	855054	5.854E-03	958159

4.5 Simulation Model of JQUAD-rotor UAV/MAV

In order to ascertain that the proposed control concept of the JQUAD-rotor is feasible, a simple model of the flight vehicle is created to find out whether the three gyros are sufficient in maintaining the orientation of the vehicle. To set up the mathematical model of the UAV/MAV, the flight vehicle is regarded as a single rigid body with six degrees of freedom. The linear velocities of the UAV/MAV is given by u, v, w along the x, y, z body axis, while the angular velocities is denoted by p, q and r. The rotation speed of the four rotors are Ω_1, Ω_2, Ω_3, and Ω_4. The motion of the MAV is determined by the summation of external

forces, $\mathbf{F_{ext}} = [\ F_x\ F_y\ F_z]'$, and external moments about the CG, $\mathbf{M_{ext}} = [\ L\ M\ N]'$ acting on it. The rotor thrusts are denoted by F_1, F_2, F_3 and F_4 and rotor torques as M_1, M_2, M_3 and M_4. The aerodynamic forces are not included to keep the simulation model simple. Applying Newton's Second Law of Motion,

$$F_x = m(du/dt + qw - rv) \tag{4.12}$$

$$F_y = m(dv/dt + ru - pw) \tag{4.13}$$

$$F_z = m(dw/dt + pv - qu) \tag{4.14}$$

and

$$L = dH_x/dt + qH_z - rH_y \tag{4.15}$$

$$M = dH_y/dt + rH_x - pH_z \tag{4.16}$$

$$N = dH_z/dt + pH_y - qH_x \tag{4.17}$$

where

$$H_x = pI_{xx} - qI_{xy} - rI_{xz} \tag{4.18}$$

$$H_x = -pI_{xy} + qI_{yy} - rI_{yz} \tag{4.19}$$

$$H_z = -pI_{xz} - qI_{yz} + rI_{zz}$$

(4.20)

The roll, pitch and yaw rotations of the MAV about the vehicle's centre of gravity are defined by the Euler angles ϕ, θ and ψ respectively. The Euler rates of the MAV can be described by the transformation matrix in Eq. (4.21).

$$\begin{bmatrix} \dot{\phi} \\ \dot{\theta} \\ \dot{\psi} \end{bmatrix} = \begin{bmatrix} 1 & \sin\phi\tan\theta & \cos\phi\tan\theta \\ 0 & \cos\phi & -\sin\phi \\ 0 & \sin\phi\sec\theta & \cos\phi\sec\theta \end{bmatrix} \begin{bmatrix} p \\ q \\ r \end{bmatrix}$$

(4.21)

From Eq. (4.12) to Eq. (4.14),

$$\begin{bmatrix} \dot{u} \\ \dot{v} \\ \dot{w} \end{bmatrix} = \begin{bmatrix} g\sin\theta \\ -F_4/m - g\sin\phi\cos\theta \\ (F_1+F_2+F_3)/m - g\cos\phi\cos\theta \end{bmatrix}$$

(4.22)

Let $\mathbf{I} = \begin{bmatrix} I_{xx} & -I_{xy} & -I_{xz} \\ -I_{yx} & I_{yy} & -I_{yz} \\ -I_{zx} & -I_{zy} & I_{zz} \end{bmatrix}$ represent the moments of inertia of the flight vehicle.

From Eq. (4.15) to Eq. (4.20),

$$\begin{bmatrix} \dot{p} \\ \dot{q} \\ \dot{r} \end{bmatrix} = \text{Inv}(\mathbf{I})^* \begin{bmatrix} r(-I_{yx}p + I_{yy}q - I_{yz}r) - q(-I_{zx}p - I_{zy}q + I_{zz}r) + q(J_1\Omega_1 + J_2\Omega_2 + J_3\Omega_3) \\ + rJ_4\Omega_4 + D_{1,y} * F_1 - D_{2,y} * F_2 \\ p(-I_{zx}p - I_{zy}q + I_{zz}r) - r(I_{xx}p - I_{xy}q - I_{xz}r) - p(J_1\Omega_1 + J_2\Omega_2 + J_3\Omega_3) \\ + M_4 + D_{3,x} * F_3 - D_{1,x} * F_1 \\ q(I_{xx}p - I_{xy}q - I_{xz}r) - p(-I_{yx}p + I_{yy}q - I_{yz}r) - pJ_4\Omega_4 - M_1 - M_2 - M_3 \\ + D_{4,x} * F_4 \end{bmatrix}$$

(4.23)

where J_1, J_2, J_3 and J_4 are moment of inertia of the rotors. The schematic of the closed-loop system is given in Figure 4.10. The estimated values for the moment of inertia matrix of the model is $\mathbf{I} = \begin{bmatrix} 0.00025 & -0.00004 & 0.00004 \\ -0.00004 & 0.00063 & 0.00001 \\ 0.00004 & 0.00002 & 0.00082 \end{bmatrix}$.

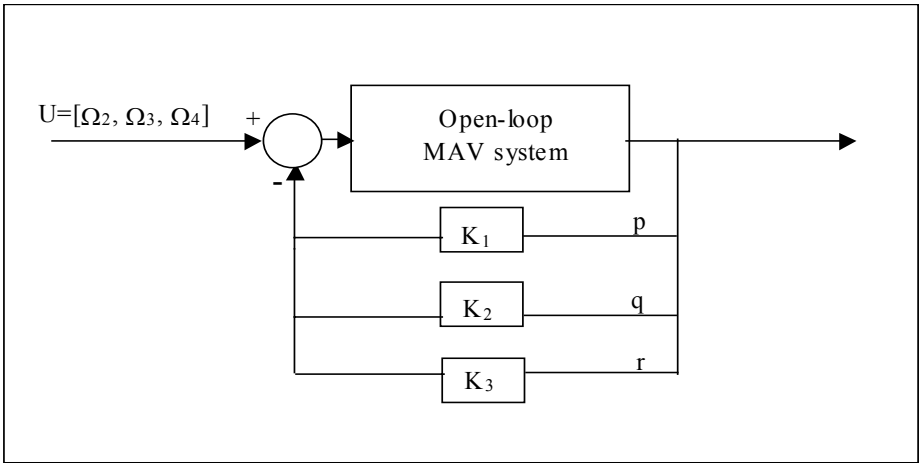

Figure 4.10. Schematic diagram of the closed-loop MAV system.

4.6 Simulation Results

The first simulation is carried out to obtain the response of the open loop system. From the results shown in Figures 4.11-4.16 of Section 4.6.1, it can be seen that the open loop system is highly unstable as expected.

4.6.1 Open-loop simulations

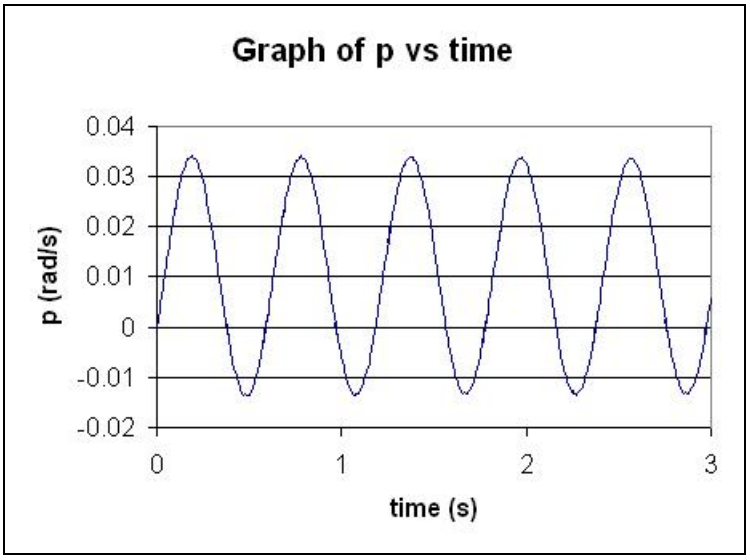

Figure 4.11. JQUAD-rotor open-loop response of p (rad/s) vs time (s).

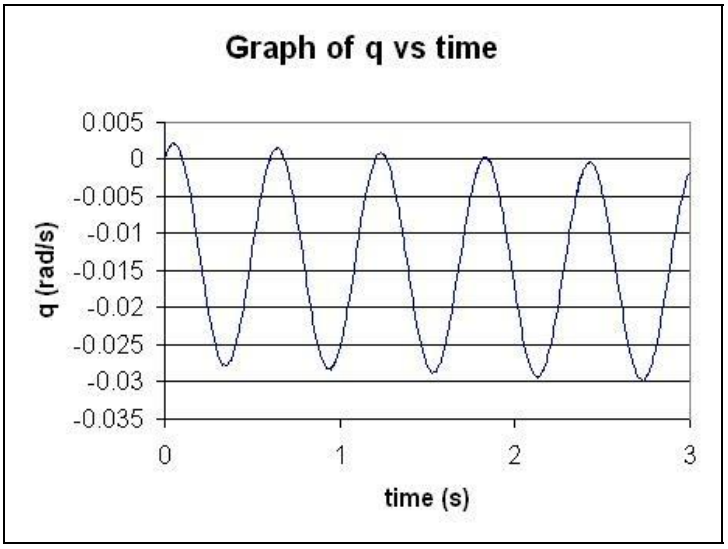

Figure 4.12. JQUAD-rotor open-loop response of q (rad/s) vs time (s).

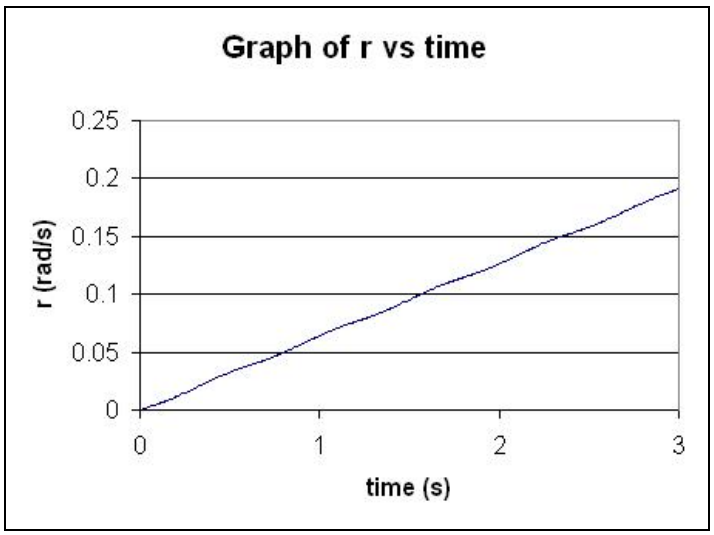

Figure 4.13. JQUAD-rotor open-loop response of r (rad/s) vs time (s).

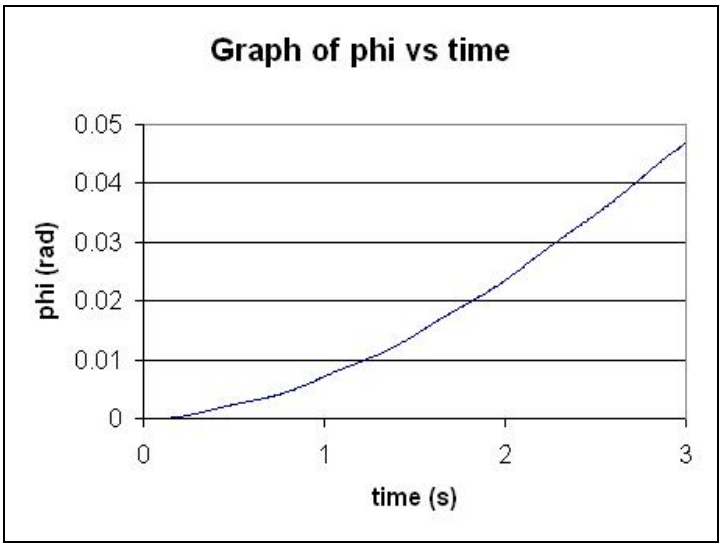

Figure 4.14. JQUAD-rotor open-loop response of angle ϕ (rad) vs time (s).

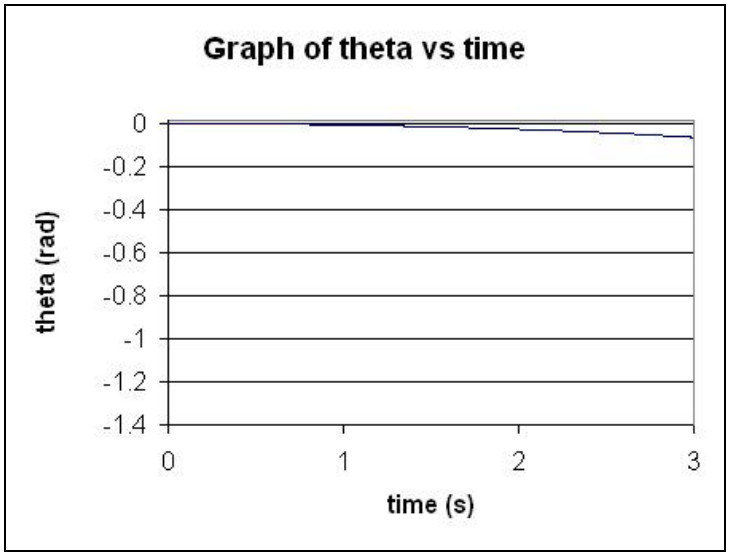

Figure 4.15. JQUAD-rotor open-loop response of angle θ (rad) vs time (s).

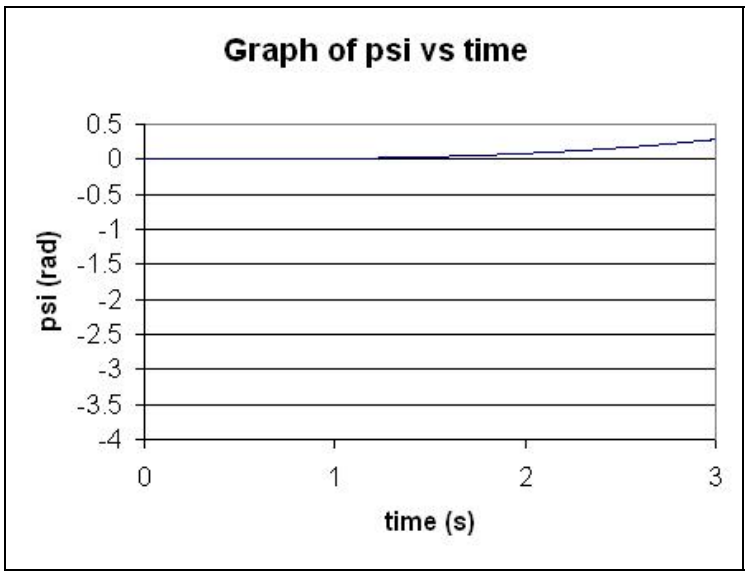

Figure 4.16 JQUAD-rotor open-loop response of angle ψ (rad) vs time (s).

4.6.2 Closed-loop simulations

In order to make the MAV more stable, the angular velocities of the vehicle are fed back via three gyros to regulate them about zero values. In this section, the simulation results (Figures 4.17-4.22) reveal that the closed loop system is now

much stable. The gains of the roll, pitch and yaw gyros used in the simulation are $k_1 = 50$ $k_2 = -50$ and $k_3 = 20$.

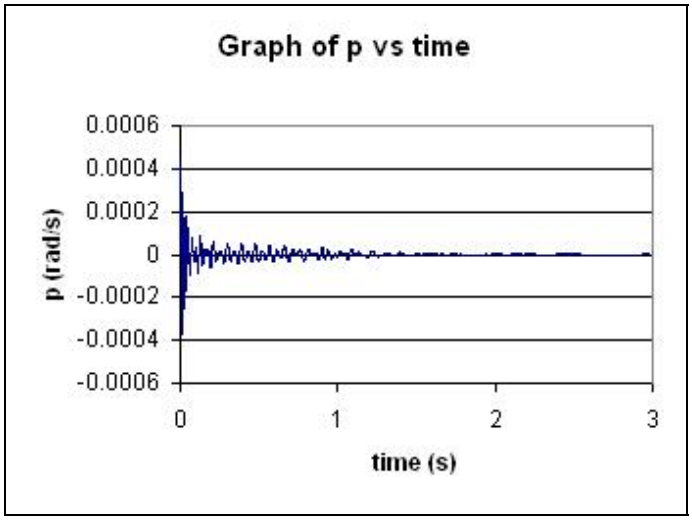

Figure 4.17. JQUAD-rotor closed-loop response of p (rad/s) vs time (s).

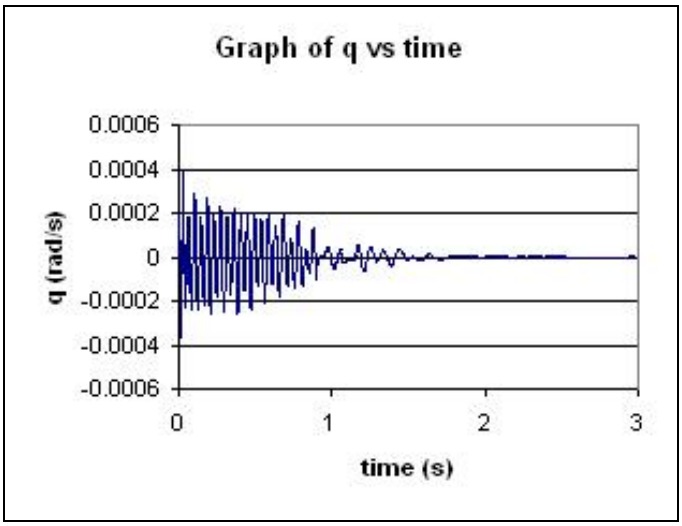

Figure 4.18. JQUAD-rotor closed-loop response of q (rad/s) vs time (s).

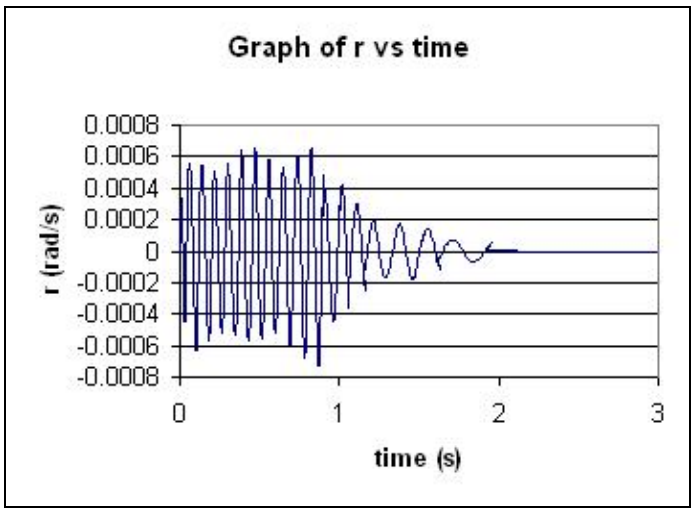

Figure 4.19. JQUAD-rotor closed-loop response of r (rad/s) vs time (s).

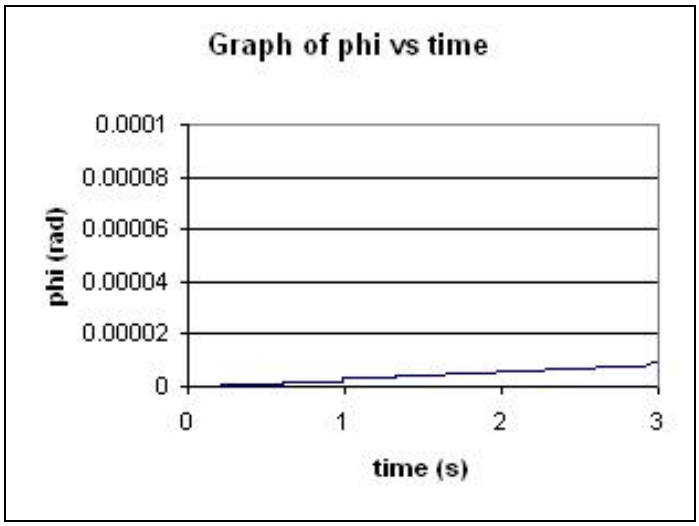

Figure 4.20. JQUAD-rotor closed-loop response of angle ϕ (rad) vs time (s).

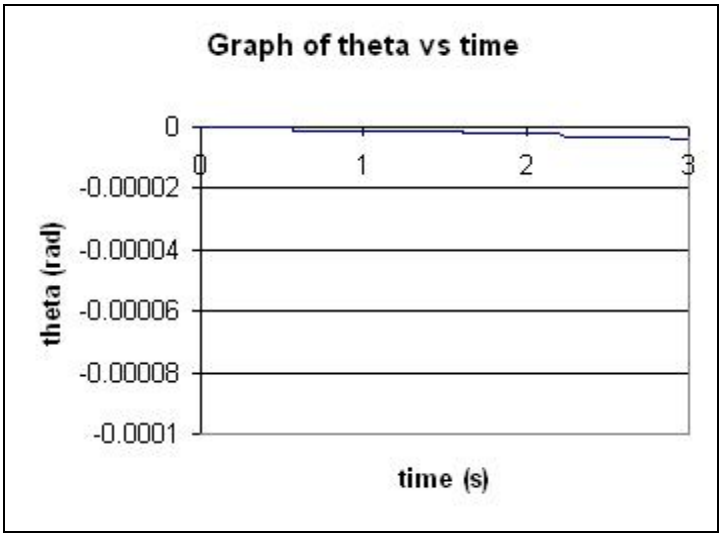

Figure 4.21. JQUAD-rotor closed-loop response of angle θ (rad) vs time (s).

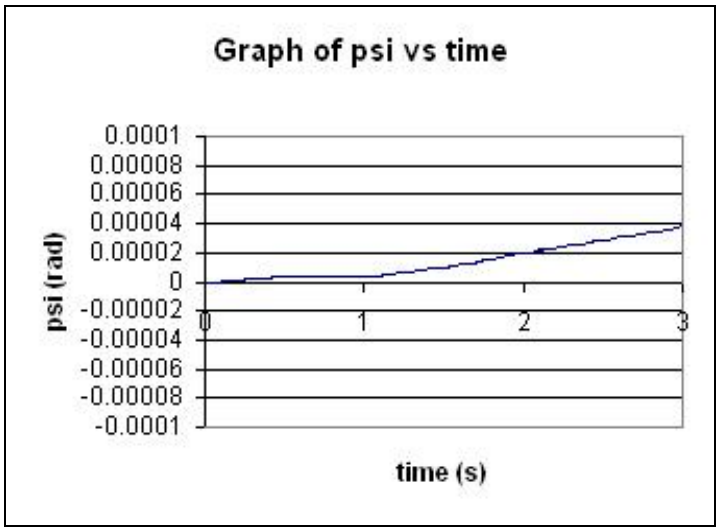

Figure 4.22. JQUAD-rotor closed-loop response of angle ψ (rad) vs time (s).

With the promising findings from the model simulations of the JQUAD-rotor, a prototype has been constructed and the preliminary flight tests (Figure 4.23) confirmed that it is a feasible concept. The content of this work has been published in [144-145].

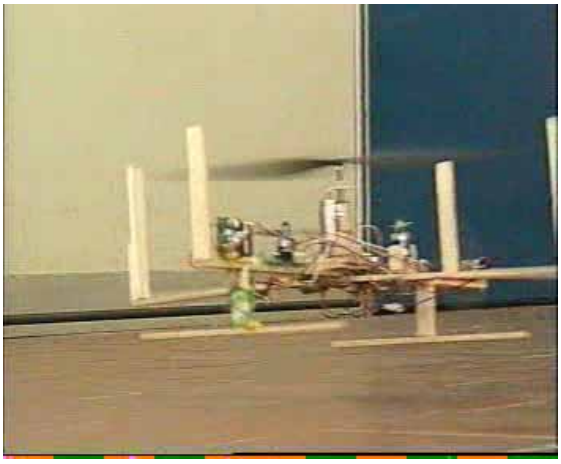

Figure 4.23. Preliminary flight test of JQUAD-rotor.

5. Design Optimization of Fixed-Wing UAV/MAV

In this chapter, an automated design methodology for the conceptual design of a fixed-wing UAV/MAV using genetic algorithms is proposed. Some of the research work on fixed-wing MAV design includes Morris [144] using six design variables: wing area, wingspan, cruise lift coefficient, loiter lift coefficient, gross take-off weight and power. The design problem is restricted by six constraints: flight duration, operation radius, minimum turn radius, minimum climb angle, maximum altitude and number of climbs. His optimization problem is to find the smallest vehicle that will fulfil these mission constraints, using genetic algorithms as the optimization tool.

In the works of Rais-Rohani and Hicks [147], the function of the MAV is to carry out short-range reconnaissance mission using a biplane configuration. The optimization problem is formulated as the minimization of MAV size using seven design variables: wing chord, wingspan, tail span, tail chord, distance from aerodynamic center of wing to that of tail, tail incidence angle and center of gravity location. The eight constraints in their problem are wing loading, thrust-to-weight ratio, horizontal tail-area, horizontal tail span, fuselage length, pitching moment coefficient at zero angle of attack, gradient of pitching moment coefficient versus angle of attack, and gross weight. The optimal solution of their problem is obtained using an extended interior penalty function method which may not be robust enough to prevent the convergence to a local optimality. Some other recent works include Grasmeyer and Keennon [148], Wu et al. [149] and La Rosa et al. [150].

One significant aspect of this study is the incorporation of winglet design and sizing. The purpose of this added feature is to minimize the “leakage” of flow from the bottom surface to the upper surface of the wings, as this will cause a reduction in the overall lift. Another major difference in the proposed MAV design with previous works is that a “flying wing” configuration has been selected here. The advantages of such configuration will be elaborated in the following section.

A multidisciplinary design optimization problem, such as aircraft design, typically has non-convex search space. Gradient-based methods, employed to such problems would usually produce optimal solutions at the local minima. Thus, non-deterministic search methods, such as genetic algorithms (GA) is well suited for such design problem. Moreover, the design process can be shortened significantly through parallel computation as it possible to convert genetic algorithms for parallel implementation without great difficulty. A case study is presented in Section 5.5 to investigate the performance of genetic algorithms, compared with a nonlinear optimization package developed by Spellucci [151-152] called DOLNP2 that is based on well-established sequential quadratic programming (SQP).

5.1 Design Strategy

In the proposed design approach, winglets are incorporated to reduce the effects of “leakage” of flow from the bottom surface of the wing, which will cause a reduction in the overall lift. This is significant in MAVs as they usually have short and stubby wing. Another good strategy is to mount the plane components (such as servos, receiver, electric motor, etc) directly inside the wing, thereby eradicating

the need of a fuselage. This would reduce the size, weight, and thus, overall drag of the flight vehicle. To further enhance this merit point, a tailess configuration is chosen instead of the conventional tailed version. Such strategies will allow the design problem to be simpler, since the design of fuselage and horizontal tail will not be required.

The flying wing would have straight trailing edges, to facilitate the installation of the control surfaces. Only two servos will be installed on the MAV, one for each elevon, to control the pitching and rolling motion. Compared to the tailed version, which needs one servo for pitching and two servos for rolling, this would result in the use of one lesser servo. By removing the rudder control, it will further reduce one servo, and its corresponding linkages, thereby minimizing the air vehicle's overall weight.

It is desirable to have an automatic piloting system for the MAV, especially so since its small size makes it susceptible to wind gusts. However, a study on the current commercially available autopilot systems shows that they are too large and heavy to be implemented on a MAV. Therefore, the MAV will be flown and controlled by a remote human pilot via a conventional radio control system.

5.2 Aerodynamic Estimation

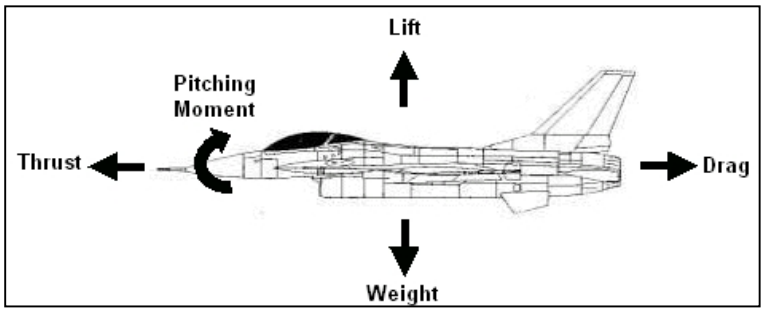

Figure 5.1. Forces and pitching moment acting on an airplane.

Figure 5.1 shows a picture of the forces and pitching moment acting on an airplane. The lift, drag forces and pitching moment are usually expressed in dimensional-less coefficients.

$$\text{Lift coefficient, } C_L = \frac{Lift}{0.5\rho U^2 S} \tag{5.1}$$

$$\text{Drag coefficient, } C_D = \frac{Drag}{0.5\rho U^2 S} \tag{5.2}$$

$$\text{Pitching moment coefficient, } C_M = \frac{Pitching\ \ moment}{0.5\rho U^2 S\bar{c}} \tag{5.3}$$

where $\bar{c}$ is the mean aerodynamic chord length (m), ρ is air density (kg/m^3), U is airplane relative velocity (m/s), and S is the wing planform area (m^2).

There are many methods that can be used by researchers to calculate the aerodynamic characteristics of wing, depending on the types of application. Most recent methods, such as Euler methods [153], are highly complex, and computationally expensive to perform. Vortex lattice method (VLM) is one of the methods that have been applied to solve steady lifting-surface problems. This approach, developed by Falkner [154], Rubbert [155] and others has been proven to give good results for a variety of configurations. Margason et al. [156] compared the aerodynamic coefficients computed using VLM, source panel method, low-order and high-order surface potential distribution methods and concluded that VLM yields agreeable results with experiments. It is noted that VLM is also used in the aerodynamic estimation in the study of Rais-Rohani and Hicks [147].

In this method, the wing is represented as a planar surface on which a grid of horseshoe vortices is superimposed. The velocities induced by each horseshoe vortex element are calculated using the *law of Biot-Savart*,

$$\overrightarrow{\mathrm{dV}} = \frac{\Gamma_n(\overrightarrow{dl} \times \vec{\mathrm{r}})}{4\pi \mathrm{r}^3} \tag{5.4}$$

Figure 5.2 shows a typical finite length vortex segment. The induced velocities are summed for all control points on the wing to give a set of linear algebraic equations for the horseshoe vortex strengths. In solving the governing equation, the continuous distribution of bound vorticities over the wing surface is approximated by a finite number of discrete horseshoe vortices. Trapezoidal panels are used in

this study. The bound vortex is located at the quarter-chord line of the panel and aligned with the local sweep back angle. Each control point (point R) is located at the midspan of the three-quarter-chord line of each elemental panel.

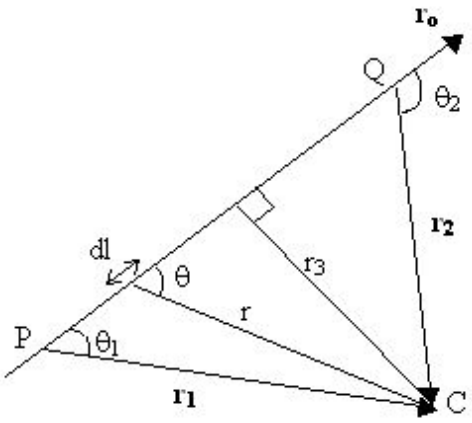

Figure 5.2. Definition of a vortex segment.

The basic expression for calculating the induced velocity by a horseshoe vortex PQ is given as

$$\vec{V} = \frac{\Gamma_n}{4\pi} \frac{\vec{r_1} x \vec{r_2}}{\left|\vec{r_1} x \vec{r_2}\right|^2} \left[\vec{r_0} \cdot \left(\frac{\vec{r_1}}{r_1} - \frac{\vec{r_2}}{r_2} \right) \right]$$

(5.5)

The velocity induced at the m^{th} control point by the vortex of the nth panel can be written in the form

$$\vec{V}_{m,n} = \vec{C}_{m,n} \Gamma_n$$

(5.6)

where $\vec{C}_{m,n}$ is the influence coefficient that depends on the geometry of the n^{th} horseshoe vortex and its distance from the control point of the m^{th} panel. The total induced velocity at the m^{th} control point will then be

$$\vec{V}_{m,n} = \sum_{n=1}^{2p} \vec{C}_{m,n} \Gamma_n \tag{5.7}$$

There are altogether 2p panels on both the starboard and port wing. The boundary condition, that the surface is a streamline, is applied to compute the unknown vortex strengths, Γ_n. This means that the resultant flow is tangential to the wing at every control point. The forces on the panels are then computed from the obtained vortex strengths.

5.3 Mesh Generation

A mesh generator module, written in C language, is used to automate the generation of mesh of the MAV given any set of wing parameters and airfoil shape. The mean camber line of the airfoil shape is extracted from the airfoil shape and discretised in the chordwise and spanwise direction to form the panels for wing and winglet. Horseshoe vortices are then superimposed on all the panels, to calculate the forces acting on each panel, using the vortex lattice method (VLM). Figure 5.3 shows an example of a surface mesh of a tailess MAV with winglets. Vertical flat plate winglets are used in this study, as they are easier to fabricate and install on the flight vehicle, with satisfactory performance. The airfoil chosen is E184, commonly used for tailess airplane.

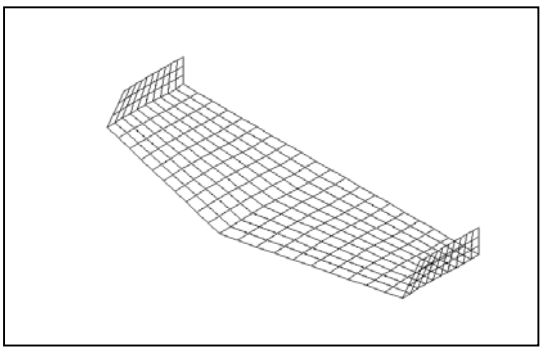

Figure 5.3. Surface mesh of a tailess MAV with winglets.

5.4 Multidisciplinary Optimization Problem Formulation

5.4.1 Design parameter definition

The six design parameters used in the MDO problem are angle of attack (α), main wing twist angle (θ_t), winglet span (b_2), main wing chord (c_1), main wing taper ratio (λ_m) winglet taper ratio (λ_w). The main wingspan is fixed at 30cm. The choice of this set of parameters allows the definition of a tailess flying-wing that can be fabricated with reasonable ease. This is even one design variable less than the study by Rais-Rohani and Hicks [147] because of the flying-wing concept. The wing tip chord and the winglet tip chord are obtained from the values of main wing chord (c_1), main wing taper ratio (λ_m) winglet taper ratio (λ_w) as follows.

$$\text{Wing tip chord, } c_2 = \lambda_m \times c_1 \tag{5.8}$$

$$\text{Winglet tip chord, } c_3 = \lambda_w \times c_2 \tag{5.9}$$

Figure 5.4 shows the parameters for defining the geometry of a wing. The optimal winglet span parameter (b_2) and its chord lengths (c_2) and (c_3), will be determined such that it will reduce the overall drag of the flight vehicle.

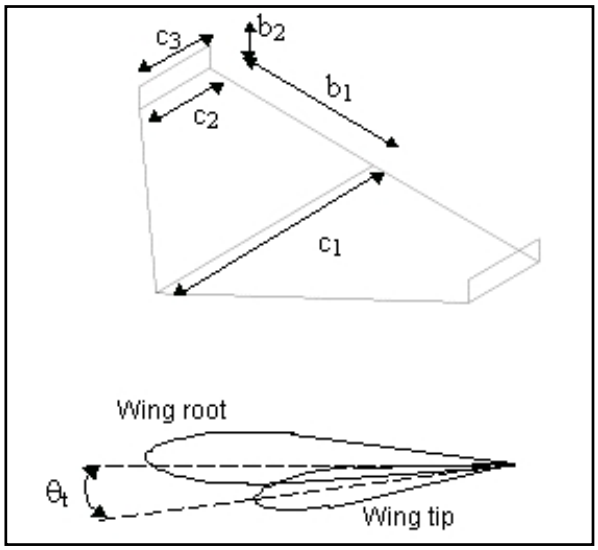

Figure 5.4. Parameters defining the wing geometry.

5.4.2 Optimization constraints

5.4.2.1 Stability constraint

In order to achieve static longitudinal stability, the center of gravity of the flight vehicle, x_{CG}, at a location such that the plane is balanced, must be in front of its aerodynamic center location, x_{ac}. The aerodynamic center of the airplane is defined as the point on the plane whereby the pitching moment is independent of its angle of attack. The difference between the two locations is called static margin, K_n. Static margin is a measure of the static longitudinal stability of an aircraft, and is identified to be a constraint in the design problem. In most aircraft design, the

desired static margin is usually in the range of 5% to 15%. Here, the value of K_n is chosen to be at least 10%.

$$K_n = \frac{X_{ac} - X_{CG}}{X_{CG}} * 100\% \tag{5.10}$$

It is possible to achieve a large K_n by having the center of gravity of the airplane located as nose-front as possible. However, whether this can be achieved is determined by the physical attributes (dimensions and centers of gravity) of the airplane's individual components. These components include the propulsion, power source, and actuators. x_{CG} cannot be shorter than the smallest achievable center of gravity location $x_{CG,\ L}$, that can be attained due to the components' positions. Hence, it is necessary to include this as a constraint as well.

5.4.2.2 Performance constraint

It is unrealistic to fly the MAV at very high speed by a human pilot via radio control, especially near urban structures. Thus, it is necessary to impose a constraint on the cruising speed, V_c. The cruising speed of the MAV developed by Morris [146] is about 9 m/s.

The minimum cruising speed, $V_{c,\ min}$, for a fixed-wing aircraft to maintain level flight depends on air density, the aircraft's lift coefficient, wing area and overall weight,

$$V_{c,\min} = \sqrt{\frac{2 * weight}{C_L \rho S}} \tag{5.11}$$

where C_L is the lift coefficient, ρ is the air density, and S is the wing planform area. The estimated total mass of the MAV is 73 g.

One of the most common figures of merit used in aircraft design optimization is the lift-to-drag ratio (C_L/C_D). It is desirable to maximize this value as it represents the aerodynamic efficiency of the flight vehicle. The design optimization problem is thus formulated as

$$\max f(X) = C_L/C_D \tag{5.12}$$

subject to

$$\text{Cruising speed, } Vc \leq 10 \tag{5.13}$$

$$\text{Static margin, } K_n \geq 10\% \tag{5.14}$$

$$X_{CG} - X_{CG,L} \geq 0 \tag{5.15}$$

where $X = \left(\alpha, \theta_t, b_2, c_1, \lambda_m, \lambda_w \right)$, $L \leq X \leq U$, is the set of design variables to define the geometry of the aircraft. These variables are restricted to the range of lower and upper bounds L and U shown in Table 5.1.

Table 5.1. Table of lower and upper bounds of design parameters.

	Design Parameters					
	α	θ_t	B_2	c_1	λ_m	λ_w
Upper Bound, U	7	1	0.10	0.50	1.00	1.00
Lower Bound, L	1	-1	0.03	0.30	0.01	0.01

5.4.3 Optimization using nonlinear optimization

The nonlinear constrained optimization method used here is called DONLP2, developed by Spellucci [151-152]. The program implements a sequential equality constrained quadratic programming method with an active set technique. An alternative usage of a fully regularized mixed constrained subproblem is used in the case of non-regular constraints i.e. linear dependent gradients in the "working set". The bounds on the variables are treated in a gradient-projection like fashion.

The strategy here is to use many sets of random values within the bounds of the parameters as the starting points in the nonlinear constrained optimization and select the best converged values given by the program DOLNP2. 150 optimization trials are carried out and the results are shown in Section 5.5.1.

5.4.4 Optimization using genetic algorithms

The constraints are coded into the objective function as penalty functions, h_1, h_2 and h_3. The overall objective function becomes

$$\text{Objective value} = \sum_{i=1}^{3} \sigma_i h_i \; - \sigma_4 C_L/C_D \tag{5.16}$$

where σ_i, i = 1 to 4 are the weighting factors (shown in Table 5.2).The C_L/C_D is multiplied to a negative factor since the genetic algorithms routines are originally intended for minimization problem. The population size used is 50, with 95% crossover probability and 10% mutation probability. The search process is carried out for 450 generations to characterize the variation of objective value with the number of evaluations. The optimization codes are compiled and performed on a 950 MHz personal computer. The design optimization flowchart is provided in Figure 5.5.

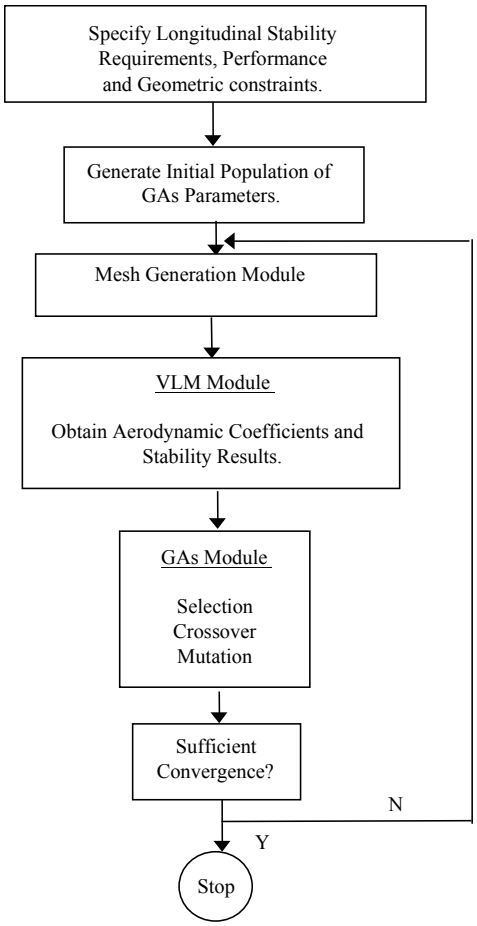

Figure 5.5. Flow chart depicting the proposed design algorithm for fixed-wing MAV.

Table 5.2 Table of weighing factors

Weighing factors	Value
σ_1	0.01
σ_2	33.33
σ_3	33.33
σ_4	33.33

5.5 Optimization Results

5.5.1 Results of nonlinear optimization using DONLP2

In Figure 5.6, the converged results of the 150 trials conducted using DONLP2 are presented. It can be seen that by randomly selecting the initial parameter values, the converged objective function values obtained by the nonlinear optimization routine differ significantly. This reveals that SQP-based optimization approach is highly sensitive to initial starting point due to the complexity of the search space. The good converged solutions found lie in the proximity of C_L/C_D =5, and the best value obtained is 5.0224 after a computation time of 11357s or 2.15 hours. Figure 5.7 shows the corresponding computational time for all optimization trials performed.

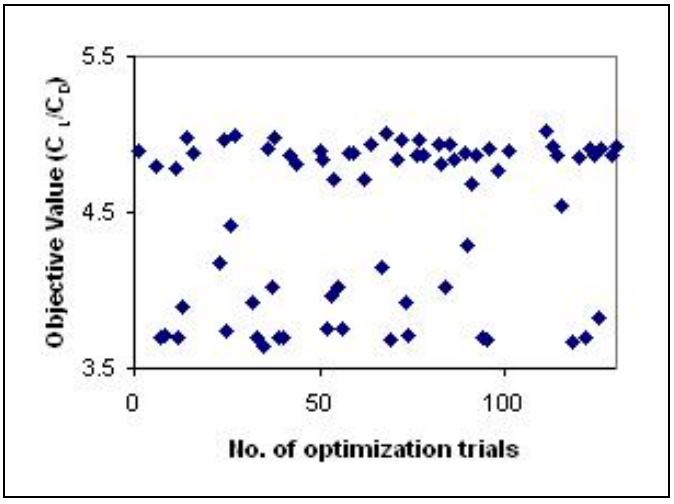

Figure 5.6. Graph of objective value vs 150 optimization trials (DONLP2).

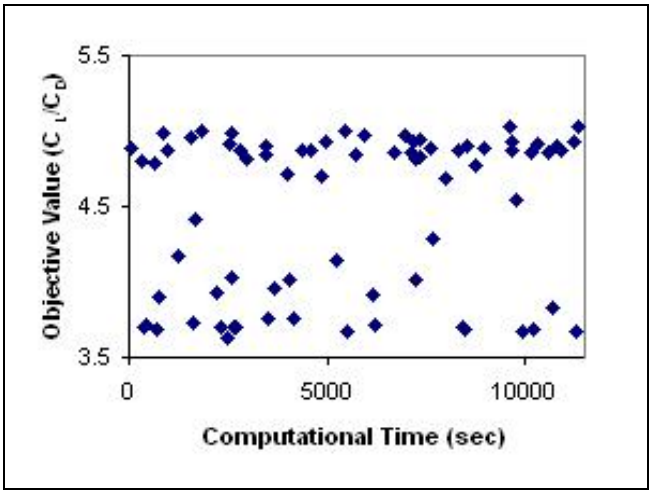

Figure 5.7. Graph of objective value vs computational time (DONLP2).

5.5.2 Results of optimization using genetic algorithms

From Figure 5.8, it can be seen that the objective values obtained by GA lie in the range of 5.1 to 5.5 during the first 150 generations, suggesting that it is "trapped" in a local optimum region. However, it manages to escape and move towards other optimal regions. After the MDO process has been carried out for 450 generations, the converged parameters are obtained (with all penalty functions $h_{i=1 \text{ to } 3}$ equal to zero) and tabulated in Table 5.3. The converged lift-to-drag ratio (C_L/C_D) found here is 7.13, after a computational time of 6195 s (or 1.72 hr). This is 41.9% higher than the best converged solution (C_L/C_D =5.0224) obtained using DONLP2.

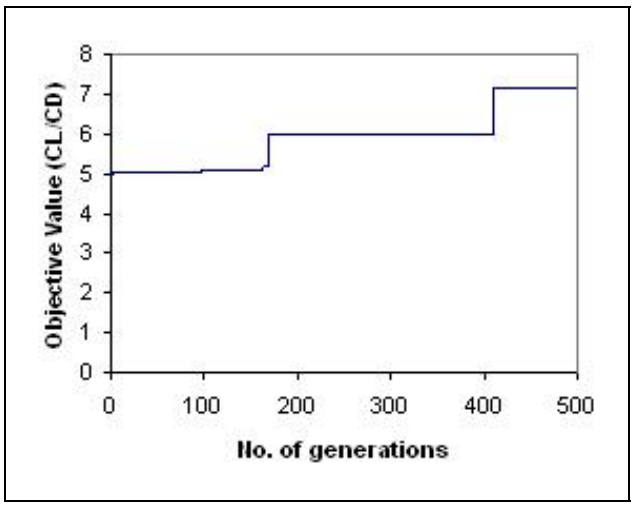

Figure 5.8. Graph of objective value vs generation (GA).

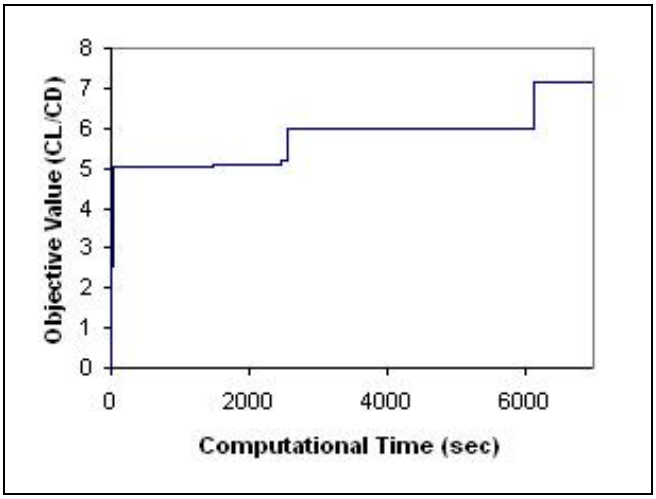

Figure 5.9. Graph of objective value vs computational time (GA).

From the glide tests performed on the fabricated model (Figure 5.10), based on the converged parameters, the airplane is observed to be static longitudinally stable. The actual C_L/C_D ratio differs from the computed value by 10% due to fabrication imperfection and uncontrollable environmental disturbances. This research work has been published in [157-158].

Figure 5.10. Photograph of fabricated prototype.

Table 5.3. Table of converged parameters and objective value.

Optimization Method	Design Parameters						Objective Value
	α	θ_t	b_2	c_1	λ_m	λ_w	
DOLNP2	5.3	0.4	0.058	0.451	0.67	0.92	5.022
Genetic Algorithms	5.0	0.4	0.086	0.500	1.00	0.90	7.130

6. Genetic Algorithms

Genetic algorithms (GA) are search procedures that mimic the renowned Darwinian's theory of evolution. Originally developed by Holland [159], there have been many improvements made by De Jong [160] and Goldberg [161]. Genetic algorithms operate on a population of potential solutions, applying the "survival of the fittest" principle to produce better approximations to a solution.

The optimization using genetic algorithms begins with an initial population of randomly generated chromosomes, whose values are uniformly distributed within a lower and upper bound. The bigger the population means that more points in the search space are explored. It then enters a loop that will end either according to a user-defined number of iterations (also known as generations) or based on some user-specified termination criteria. In each generation, every chromosome will undergo three basic operations: selection, crossover and mutation, to produce better offsprings that will then propagate into the new population.

6.1 Representations in Genetic Algorithms

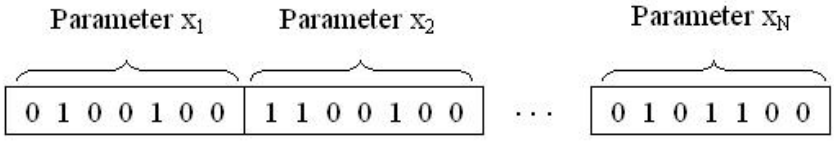

Figure 6.1. Representation of a binary chromosome.

Traditionally, solutions in GA are represented as chromosomes using the single-level, binary string representation, with each gene having a value of either 0 or 1

(Figure 6.1). The actual number of binary digits to represent the parameter depends on the required precision. The resolution of the parameter represented by an n-bit binary number is

$$\text{Resolution} = (\text{upper bound} - \text{lower bound}) / (2^n - 1) \tag{6.1}$$

usually rounding-off to one significant figure. The formula for finding the number of required binary digits for a specified resolution is given as

$$n = \frac{\log_{10}(1 + \frac{\text{upper bound - lower bound}}{\text{resolution}})}{\log_{10} 2} \tag{6.2}$$

rounding up to the next higher integer.

For example, if there are 5 parameters ranging from 0.1 to 0.2 and the required resolution is 0.0001,

$n = \log_{10}[\ 1 + (0.2 - 0.1) / 0.0001] / \log_{10}(2)$

$= 9.96$

≈ 10

Thus, each parameter is represented by a 10-bit binary string, and the chromosome will have a total of 50 genes. The actual value of a particular parameter with a representation of $(1100110101)_2$ can be calculated as follows.

$$(1100110101)_2 = (1 \times 2^0 + 0 \times 2^1 + 1 \times 2^2 + 0 \times 2^3 + 1 \times 2^4 + 1 \times 2^5 + 0 \times 2^6 + 0 \times 2^7 + 1 \times 2^8 + 1 \times 2^9) \times 0.0001 + 0.1$$

= 0.1821

Studies by Wright [162] have shown that real-valued representation in GA offers numerous advantages such as better efficiency and lesser computer memory usage. Hence, in this study, the real-valued representation is chosen instead of the traditional binary representation. Each of the design parameters is represented by a real number and the chromosome is an array of these design parameters (Figure 6.2). Each parameter has its corresponding upper and lower bounds of allowable values. One obvious advantage of real-valued representation is the reduction of overheads incurred in the conversion of the binary number into its equivalent real value as shown in the above example. This is especially pronounced when there are many design parameters, and a high resolution is required for each parameter.

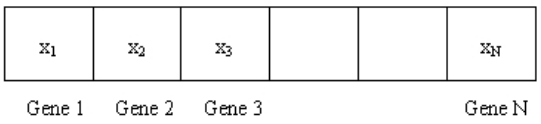

Figure 6.2. Representation of a real-valued chromosome.

6.2 Operations in Genetic Algorithms

Genetic algorithms consist of the following three main processes: selection, crossover and mutation. The selection operator determines the number of times a parent chromosome is chosen for reproduction. There are many variations concerning how potential parents are selected to produce new offsprings. The method chosen here is one of the most commonly used methods, *roulette wheel selection*[161], where chromosomes with high fitness values have a higher probability in participating in reproduction of new chromosomes. This mimics the

"survival of the fittest" phenomenon that one observes in nature. The probability (or fitness ratio) of an individual chromosome selected for reproduction is given by

$$P_i = \frac{f_i}{\sum_{i=1}^{N_{chrom}} f_i} \tag{6.3}$$

where f_i is the fitness of the i^{th} individual chromosome, and N_{chrom} is total number of chromosomes in the population. Table 6.1 shows an example of the roulette wheel selection process for a population of four chromosomes. In a real roulette wheel (Figure 6.3), the segment where the free spinning arrow stops will be the chosen candidate. To simulate this process, a random number is generated in the intervel 0 to 99. If the generated number falls in the intervel of 0 to 59, the chosen candidate for the crossover process is chromosome C1. If the generated number falls in the intervel of 60 to 64, the chosen candidate is chromosome C2. Chromosome C3 is selected if the generated number falls in the intervel of 65 to 79. Finally, if the generated number falls in the intervel of 80 to 99, then chromosome C4 is the chosen one. Thus, the chromosomes with higher fitness values have higher probability to be selected for reproduction or crossover.

Table 6.1. Roulette wheel selection example.

	Fitness value, f_i	Fitness ratio, P_i
Chromosome 1, C1	12	0.600
Chromosome 2, C2	1	0.050
Chromosome 3, C3	3	0.150
Chromosome 4, C4	4	0.200

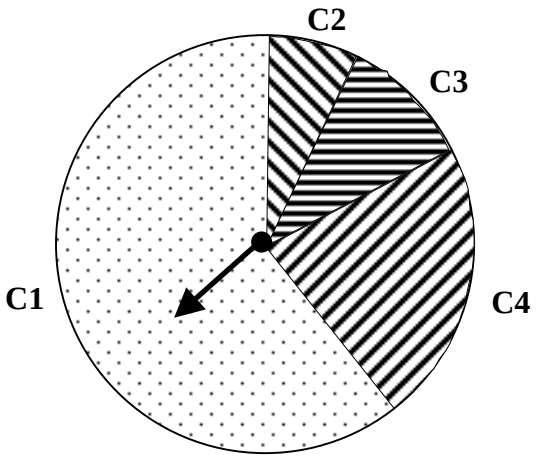

Figure 6.3. Representation of a roulette wheel.

Crossover is the main genetic search operator in genetic algorithms. It recombines the genetic material from two parent chromosomes to create two new children chromosomes, so that the new individuals possess some parts of genetic information from each of their parent chromosomes. It is a powerful process that extends the search in many directions. The crossover operation is controlled by a

crossover rate, denoted by P_c, which is usually set at 80% to 100%. In binary chromosomes, one form of crossover operation is the single point crossover, in which the crossover point is randomly selected, and the genes from two parent chromosomes behind the crossover point are swapped to produce two new child chromosomes (Figure 6.4).

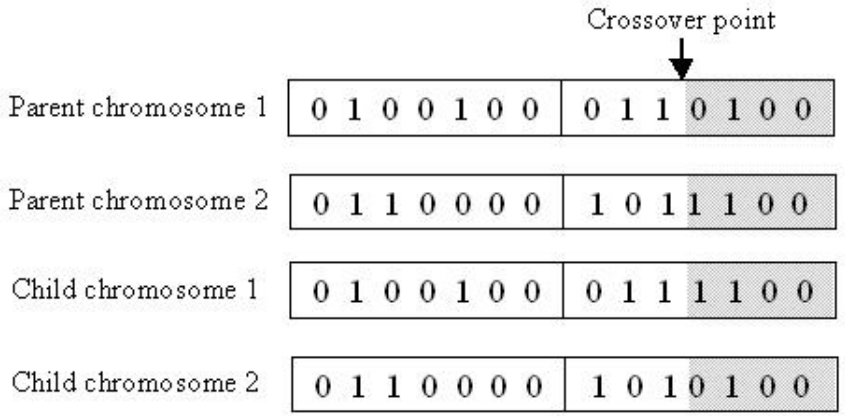

Figure 6.4. Crossover operation on two binary chromosomes.

For GA using the real-valued representation, the preferred crossover operation is the intermediate crossover as studies by Muhlenbein and Schlierkamp-Voosen [163] have reported promising results and is also adopted in this study. The child chromosomes are obtained by,

$$Chrom_{c1} = \gamma_1 (Chrom_{p1} - Chrom_{p2}) \tag{6.4a}$$

$$Chrom_{c2} = \gamma_2 (Chrom_{p1} - Chrom_{p2}) \tag{6.4b}$$

where $Chrom_{p1}$, $Chrom_{p2}$ and $Chrom_{c1,}$ $Chrom_{c2}$ are the parent and child chromosomes respectively, γ_1 and γ_2 are scaling factors chosen randomly in the range of $[\gamma_L, \gamma_U]$, typically set as [-0.25,1.25].

Mutation serves as a secondary search operator for exploring new search region by altering the allele of a gene randomly. This operation helps to ensure that the search process will not be trapped in local minima/maxima. The probability (or mutation rate), denoted by P_m, of the mutation process is usually set low, typically around 5% to 20%. It is not advisable to set P_m too high, as the optimization process will tend towards a haphazard and random search. For binary chromosomes, a gene is selected randomly, and its value inverted from 0 to 1, and vice versa (Figure 6.5).

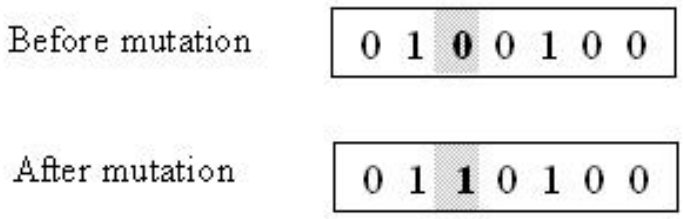

Figure 6.5. Mutation operation for binary chromosome representation.

For real-valued chromosomes, mutation is achieved by perturbing the gene values within the allowed range. One version proposed by Muhlenbein and Schlierkamp-Voosen [163]) is,

Mutated value = original value + 0.5 m_{fac1} m_{fac2} (upper bound – lower bound)

(5.5)

where m_{fac1} = 1 or –1 with equal probability of 0.5 and

$$m_{fac2} = \sum_{i=0}^{19} \gamma_i 2^{-i}$$

(5.6)

where γ_i = 1 with a probability of 5%, and 0 with a probability of 95%.

A cycle of selection, crossover and mutation to reproduce children chromosomes is known as a generation, and the cycle repeats again until the stipulated number of generations is reached or the process has converged to a solution when there is no more improvement in the solutions for many generations. It really depends on the amount of time the designer is willing to wait to obtain the near-optimal or exact optimal solutions.

6.3 Comparison of Genetic Algorithms with Traditional Gradient-based Optimization Methods

One major difference between GA with traditional gradient-based or Newton-based optimization [164-166] methods is that GA does not require the calculation of function gradient or derivative values, which are often unavailable, and computationally expensive to obtain numerically.

Moreover, gradient-based methods are not suitable for solving many engineering design problems are plagued with complex search space with numerous local

minima/maxima. Depending on the starting point, gradient-based methods usually converge to different local minima/maxima, and get trapped in it, unable to arrive at the desired global minimum/maximum. The mutation process allows the search procedure to escape being trapped in these local optima. Using GA, the poor solutions die out since the better ones are able to propagate to produce potential better ones that will replace the poorer solutions.

6.4 Applications of Genetic Algorithms in Engineering Design Problems

Genetic algorithms have proven itself to be a robust optimization tool that has been employed in many engineering design problems, such as scheduling problems, structural design, facility layout design, mechanical hardware design and aircraft design [167-177].

6.5 Enhancement Features Added to Genetic Algorithms

In this work, the generic real-valued genetic algorithms have been modified to enhance its performance in solving real engineering applications. The design problems in this work involve different variables that require different precision. For instance, the position variable should be limited to a precision of three decimal places e.g. 0.011 m, instead of a number like 0.0114537…..m , since the components will be assembled by hand using a typical ruler. Thus, besides a data array that contains the upper bounds, another that contains the lower bounds, one more data array will be used to contain the desired precision of the design variable. 0 means that there is no decimal places i.e. an integer variable and 3 means a precision of 3 decimal places.

Table 6.2. Example of a generic real-valued GA population.

	Gene 1	Gene 2	Gene 3
Chromosome 1	1.037513	2.059302	0.566548
Chromosome 2	3.115782	2.346672	0.415587
Chromosome 3	1.037564	1.431423	0.351487

As an illustration, if the actual problem requires a precision of three decimal places for gene 1, an integer for gene 2 and a precision of two decimal places for gene 3. Table 6.2 shows an example of a population using a generic real-valued GA. The gene 1 in chromosome 3 would be effectively same as the gene 1 in chromosome 1 (1.038 when rounded off to 3 decimal places). The gene 2 in chromosome 2 would be effectively same as the gene 2 in chromosome 1 (2 when rounded off to no decimal place). This will "deprive" the chances for other values in the desired precision to be explored to arrive at the optimal solution. Thus, this will waste unnecessary computational effort when those genes crossover with one another.

Different gene values within the lower and upper bounds of the required precision will have higher chances to appear than if there is no restriction on the desired precision. With the proposed enhanced real-valued representation, an example of the population will appear as in Table 6.3.

Table 6.3. Example of enhanced real-valued GA population.

	Gene 1	Gene 2	Gene 3
Chromosome 1	2.355	2	0.17
Chromosome 2	5.221	3	0.67
Chromosome 3	1.532	1	0.55

With the specification of the desired precision for each design variable, the original real-valued mutation given in Eq. (5.5) has to be modified as well. For example, if the original variable value is 1.034, and after mutation, it may become 1.034056 which is of no new contribution as the required precision may be only 3 decimal places, and the mutated value would be rounded off to be the same as the original value. Again, this will result in wastage of computational time. Therefore, it is proposed that the modified real-valued mutation as,

$$\text{Mutated value} = \text{original value} + 0.5 * m_{fac1} * r \tag{5.7}$$

where m_{fac1} = 1 or –1 with equal probability of 0.5, and r is a random number between the lower bound and upper bound and has the same precision as the original value. If the mutated value exceeds the corresponding bounds, the final mutated value is obtained by performing a wrap-around.

Another advantage of this proposed enhancement is that it is now possible to use only one array of data of type *float* for both integer variables and floating-point variables (i.e. numbers with decimal points). This is easier than working with

separate arrays of variables, one array of data of type *int* and one of type *float* in the programming codes.

7. Conclusions and Future Works

In this thesis, an attempt to automate the preliminary design of small-scale rotary-wing UAV/MAV using genetic algorithms has been carried out successfully. The generic real-valued GA has been greatly enhanced by controlling the desired precision of every design variable at the initialization stage, as well as during the crossover and mutation operations. This prevents the redundant appearance of design values which are smaller than the required precision, and thus, avoids unnecessary computations.

The first part involves the automation of the layout design for a single main and tail rotor UAV/MAV to ensure that the flight vehicle is as compact as possible. With the encouraging results achieved, the complexity of the design optimization problem is further increased by considering component selection and applied in the design of a quadrotor UAV/MAV.

A new multiple-rotor UAV/MAV called JQUAD-rotor has been proposed that is as easy to fabricate as the quadrotor. A specialized automated design methodology for this flight vehicle has also been developed. The strategy of using one powerful propulsion for main lift support and three smaller ones for roll, pitch and yaw control has yielded a lighter and more compact rotary-wing UAV/MAV than the quadrotor, given the same range of component products to choose from. Using three commercial off-the-shelf gyros, the simulation model revealed it is able to maintain a stable hovering condition. Preliminary flight test of a fabricated model confirmed the feasibility of this new rotary-wing UAV/MAV. However, for

applications that require maximum possible flight time, the quadrotor is still a better choice.

A design methodology has been introduced to automate the conceptual design of small-scale fixed-wing UAV/MAV. Adopting a tailess flying-wing with winglets configuration, the design problem has been carefully formulated to produce a longitudinally stable flight vehicle. By supplying the physical attributes of the airplane components, desired performance and stability margin, the developed design optimization program helps to reduce the time needed for the conceptual design of this class of UAV/MAV.

Future works may incorporate some dynamics requirements into the design optimization to achieve certain desired attributes of flight dynamics. Some form of autonomous control can also be incoporated into the current design methodologies.

Bibliography

[1] B. S. Papadales, T. A. Tibbetts, S. M. Schoenung and W. R. Meier. Remote sensing with high-altitude unmanned aerial vehicles. *Proceedings of SPIE - The International Society for Optical Engineering, v 2023*, pp. 266-277, 1993.

[2] M. M. Pendergasta and K. J. Hofstetter. Application of UAVs at the Savannah River site. *Proceedings of the AUVSI '96*, pp. 803-16, 1996.

[3] V. G. Ambrosia, S. S. Wegener, D. V. Sullivan, S. W. Buechel, S. E. Dunagan, J. A. Brass, J. Stoneburner and S. M. Schoenung. Demonstrating UAV-acquired real-time thermal data over fires. *Photogrammetric Engineering and Remote Sensing*, vol. 69, no. 4, pp. 391-402, 2003.

[4] M. Abe, K. Ishii and N. Noguchi. Enhancement of satellite imageries using an unmanned helicopter for environment monitoring. *Proceedings of the International Conference on Automation Technology for Off-road Equipment ATOE 2004*, pp. 232-237, 2004.

[5] R. Lawrence and L. Hilliard. Mission concept for the remote sensing of the cryosphere using autonomous aerial observation systems. *Proceedings of SPIE - The International Society for Optical Engineering, vol. 5661, Remote Sensing Applications of the Global Positioning System*, pp. 160-168, 2004.

[6] U. C. Ofoma and C. C. Wu. Design of a fuel cell powered UAV for environmental research. *Collection of Technical Papers - AIAA 3rd "Unmanned-Unlimited" Technical Conference, Workshop, and Exhibit*, vol. 1, pp. 193-203, 2004.

[7] V. G. Ambrosia, S. S. Wegener, J. A. Brass and S. M. Schoenung. The UAV western states fire mission: Concepts, plans and developmental advancements. *Collection of Technical Papers - AIAA 3rd "Unmanned-Unlimited" Technical Conference, Workshop, and Exhibit*, vol. 1, pp. 289-301, 2004.

[8] A. S. Lomax, W. Corso and J. F. Etro. Employing Unmanned Aerial Vehicles (UAVs) as an element of the integrated ocean observing system. *Proceedings of MTS/IEEE OCEANS*, pp. 184-190, 2005.

[9] D. Hausamann, W. Zirnig, G. Schreier and P. Strobl. Monitoring of gas pipelines - a civil UAV application. *Aircraft Engineering and Aerospace Technology*, vol. 77, no. 5, pp. 352-60, 2005

[10] E. M. Cardenas, P. J. Boschetti, A. Amerio and C. D. Velasquez. Design of an unmanned aerial vehicle, for ecological conservation. *Collection of Technical Papers - InfoTech at Aerospace: Advancing Contemporary Aerospace Technologies and Their Integration*, vol. 3, pp. 1309-1318, 2005.

[11] F. Zhang, Y. Tao, X. Chen and D. Lu. The system framework of earth observation information captures based on high altitude UAV. *IEEE International Geoscience and Remote Sensing Symposium*, pp. 2074-2077, 2005.

[12] G. Zhou, C. Li and P. Cheng. Unmanned Aerial Vehicle (UAV) real-time video registration for forest fire monitoring. *International Geoscience and Remote Sensing Symposium*, vol. 3, pp. 1803-1806, 2005.

[13] K. Kurvinen, P. Smolander, R. Pollanen, S. Kuukankorpi, M. Kettunen and J. Lyytinen. Design of a radiation surveillance unit for an unmanned aerial

vehicle. *Journal of Environmental Radioactivity*, vol. 81, no. 1, pp. 1-10, 2005.

[14] K. L. Moore, M. J. White, R. J. Bamberger and D. P. Watson. Cooperative UAVs for remote data collection and relay. *Proceedings of AUVSI's Unmanned Systems North America 2005*, pp. 41-55, 2005.

[15] M. C. L. Patterson, A. Mulligair, J. Douglas, J. Robinson and J. S. Pallister. Volcano surveillance by ACR silver fox. *Collection of Technical Papers - InfoTech at Aerospace: Advancing Contemporary Aerospace Technologies and Their Integration*, vol. 1, pp. 488-494, 2005.

[16] T. Usami, K. Ishii and N. Noguchi. Thermal remote sensing attached to an unmanned helicopter. *3rd IFAC International Workshop on Bio-Robotics, Information Technology and Intelligent Control for Bioproduction Systems*, pp. 400-404, 2006.

[17] J. W. Youngblood and R. D. Jackson. Airborne reconnaissance in the civilian sector: agricultural monitoring from high-altitude powered platforms. *Proceedings of SPIE - The International Society for Optical Engineering*, vol. 424, pp. 182-189, 1983.

[18] R. Sugiura, T. Fukagawa, N. Noguchi, K. Ishii, Y. Shibata and K. Toriyama. Field information system using an agricultural helicopter towards precision farming. *Proceedings of 2003 IEEE/ASME International Conference on Advanced Intelligent Mechatronics*, vol. 2, pt. 2, pp. 1073-1078, 2003.

[19] S. R. Herwitz, S. Dunagan, D. Sullivan, R. Higgins, L. Johnson, J. Zheng, R. Slye, J. Brass, J. Leung, B. Gallmeyer and M. Aoyagi. Solar-powered UAV Mission for Agricultural Decision Support. *International Geoscience and*

Remote Sensing Symposium (IGARSS), vol. 3, pp. 1692-1694, 2003.

[20] G. Bland, P. Coronado, T. Miles, P. Bretthauer, A. Lunsford and J. Bognar. "Sensors with wings" - Small UAVs for earth science. *Collection of Technical Papers - AIAA 3rd "Unmanned-Unlimited" Technical Conference, Workshop, and Exhibit*, vol. 1, pp. 317-327, 2004.

[21] J. Yokobori, K. Niwa, R. Sugiura, N. Noguchi and Y. Chiba. Variable management for uniform potato yield using remote sensing images with unmanned helicopter. *Proceedings of the International Conference on Automation Technology for Off-road Equipment ATOE 2004*, pp. 447-454, 2004.

[22] L. F. Johnson, S. R. Herwitz, B. M. Lobitz and S. E. Dunagan. Feasibility of monitoring coffee field ripeness with airborne multispectral imagery. *Applied Engineering in Agriculture*, vol. 20, no. 6, pp. 845-849, 2004.

[23] O. Trindade Jr., L. A. C. Jorge and J. G. B. Aguiar. Using UAVs for precision farming: First results. *Proceedings of AUVSI's Unmanned Systems North America 2004*, pp. 1169-1183, 2004.

[24] S. R. Herwitz, L. F. Johnson, S. E. Dunagan, R. G. Higgins, D. V. Sullivan, J. Zheng, B. M. Lobitz, J. G. Leung, B. A. Gallmeyer, M. Aoyagi, R. E. Slye and A. Brass. Imaging from an unmanned aerial vehicle agricultural surveillance and decision support. *Computers and Electronics in Agriculture*, vol. 44, pp. 49-61, 2004.

[25] J. Sullivan, S. Weller, M. Gumz, M. Leasure, C. Ross and J. Brost. Small UAV's for agricultural applications. *Proceedings of AUVSI's Unmanned Systems North America 2005*, pp. 1373-1385, 2005.

[26] R. Furfaro, B. D. Ganapol, L. F. Johnson and S. Herwitz. Model-based neural network algorithm for coffee ripeness prediction using helios UAV aerial images. *Proceedings of SPIE - The International Society for Optical Engineering, v 5976, Remote Sensing for Agriculture, Ecosystems, and Hydrology VII*, pp. 59760X, 2005.

[27] R. Sugiura, N. Noguchi and K. Ishii. Remote-sensing technology for vegetation monitoring using an unmanned helicopter. *Biosystems Engineering*, vol. 90, no. 4, pp. 369-379, 2005.

[28] Y. Han, M. Li, L. Jia, X. Zhang and F. Zhang. Estimating growth status of winter wheat based on aerial images and hyperspectral data. *Proceedings of SPIE - The International Society for Optical Engineering, vol. 5909, Applications of Digital Image Processing XXVIII*, pp. 1-9, 2005.

[29] Y. Han, M. Li, X. Zhang, L. Jia, X. Chen and F. Zhang. Precision management of winter wheat based on aerial images and hyperspectral data obtained by unmanned aircraft. *International Geoscience and Remote Sensing Symposium*, pp. 3109-3112, 2005.

[30] J. Olding. Operational performance analysis "an integral part of all surveillance system design!". *National Aerospace and Electronics Conference, Proceedings of the IEEE*, vol. 2, pp. 1195-119, 1994.

[31] D. Murphy and J. Cycon. Applications for mini VTOL UAV for law enforcement. Proceedings of SPIE The International Society for Optical Engineering, vol. 3577, pp. 35-43, 1998.

[32] B. Robinson, A. Aulbach and K. Lee. US Border Patrol agents test UAV capabilities. *Unmanned Systems*, vol. 18, no. 2, pp. 10-13, 2000.

[33] D. F. hougen. A miniature robotic system for reconnaissance and surveillance. *IEEE International Conference on robotics and automation*, pp. 501-507, 2000.

[34] E Magli, G. Olmo, F. Moscheni and J.-P. Thiran. HELINET: an integrated network of unmanned aerial vehicles for optical Earth surveillance. *Proceedings of the SPIE - The International Society for Optical Engineering*, vol. 4127, pp. 68-75, 2000.

[35] H. G. Nguyen and J. P. Bott. Robotics for Law Enforcement Applications Beyond Explosive Ordnance Disposal. *SPIE Proc. 4232 Technologies for Law Enforcement*, 2000.

[36] J. B. Willis and M. J. Davis. Design of the Reconnaissance, Surveillance, and Target Acquisition Squadron for the US Army's Interim Brigade Combat Team. *2000 IEEE International Conference on Systems, Man, and Cybernetics*, vol. 1, pp. 478-483, 2000.

[37] M. P. Kontitsis, N. C. Tsourveloudis and K. P. Valavanis. A UAV based automated airborne surveillance system. *11th Mediterranean Conference on Control and Automation*, pp. 1-5, 2003.

[38] P. Spanoudakis, L. Doitsidis, N. C. Tsourveloudis and K. P. Valavanis. The Market for VTOL UAVs. *Unmanned Systems Magazine*, vol. 21, no. 5, pp. 14-18, 2003.

[39] T. J. Malthus and P. J. Mumby. Sensing of the coastal zone An overview and priorities for future research. *International Journal of Remote Sensing*, vol. 24, no. 13, pp. 2805-2815, 2003.

[40] A. R. Girard, A. S. Howell and J. K. Hedrick. Border patrol and surveillance

missions using multiple unmanned air vehicles. *Proceedings of the IEEE Conference on Decision and Control, 43rd IEEE Conference on Decision and Control (CDC)*, vol. 1, pp. 620-625, 2004.

[41] B. Coifman, M. McCord, M. Mishalani and K. Redmill. Surface Transportation Surveillance from Unmanned Aerial Vehicles. *Proceedings of the 83rd Annual Meeting of the Transportation Research Board*, 2004.

[42] M. Kontitsis, N. Tsourveloudis and V. Valavanis. A UAV Vision System for Airborne Surveillance. *Proceedings of the 2004 IEEE International Conference on Robotics and Automation (ICRA),* vol. 1, pp. 78-83, 2004.

[43] A. Sinha, T. Kirubarajan and Y. Bar-Shalom. Autonomous surveillance by multiple cooperative UAVs. *Proceedings of SPIE - The International Society for Optical Engineering, v 5913, Signal and Data Processing of Small Targets 2005*, pp. 1-1, 2005.

[44] H. S. Trammell III, A. R. Perry, S. Kumar, P. V. Czipott, B. R. Whitecotton, T. J. McManus and D. O. Walsh. Using unmanned aerial vehicle-borne magnetic sensors to detect and locate improvised explosive devices and unexploded ordnance. *Proceedings of SPIE - The International Society for Optical Engineering, vol. 5778, PART II, Sensors, and Command, Control, Communications, and Intelligence (C3I) Technologies for Homeland Security and Homeland Defence IV*, pp. 963-971, 2005.

[45] J. Luo, S. Xie, Z. Gong and J. Rao. Subminiature Unmanned Surveillance Aircraft and its Ground Control Station for Security. *Proceedings of 2005 IEEE International Workshop on Safety, Security andRescue Robotic*, pp.116-119, 2005.

[46] J. Wheeler. Tactical close aerial support for public events by rotary wing UAV. *Collection of Technical Papers - InfoTech at Aerospace: Advancing Contemporary Aerospace Technologies and Their Integration*, vol. 1, pp. 484-487, 2005.

[47] G. A. Maddux, C. D. Bosco and J. D. Lawrence. Integration of unmanned systems for tactical operations within hostile environments. *Proceedings of SPIE - The International Society for Optical Engineering, v 6230 I, Unmanned Systems Technology VIII*, pp. 62300W, 2006.

[48] M. Freed, W. Fitzgerald and R. Harris. An unmanned aerial system for autonomous surveillance. *AAAI Workshop-Technical Report, v WS-06-03, Cognitive Robotics*, pp. 55-60, 2006.

[49] R. W. Beard, T. W. McLain, D. B. Nelson, D. Kingston and D. Johanson. Decentralized cooperative aerial surveillance using fixed-wing miniature UAVs. *Proceedings of the IEEE*, vol. 94, no. 7, pp. 1306-1324, 2006.

[50] S. Srinivasan, H. Latchman, J. Shea, T. Wong and J. McNair. Airborne traffic surveillance systems - Video surveillance of highway traffic. *VSSN'04 - Proceedings of the ACM Second International Workshop on Video Sureveillance and Sensor Networks*, pp. 131-135, 2004.

[51] B. Coifman, M. McCord, R. G. Mishalani, M. Iswalt and Y. Ji. Roadway traffic monitoring from an unmanned aerial vehicle. *IEE Proceedings of Intelligent Transport Systems*, vol. 153, no. 1, pp.11-20, 2006.

[52] H. Stark, P. Parthasarathy and R. N. Johnson. Considerations in designing a marine-mammal-ship collision avoidance system based on aerial imagery by an unmanned airborne vehicle. *Optical Engineering*, vol. 42, no. 1, pp. 11-

17, 2003.

[53] S. F. Moore and J. P. Cycon. “Effectiveness of Shrouded Rotor UAVs in Support of CLOSE Range Missions. *Proceedings Association for Unmanned Vehicle Systems 19th Annual Technical Symposium*, 1992.

[54] D. E. Copper and J. P. Cycon. Sikorsky Aircraft UAV Development. *Proceedings of the Nineteenth European Rotorcraft Form,* 1993.

[55] J. P. Cycon, B. Wayner and C. W. Withers. Beyond Defense: Commercialization of UAV’s. *Unmanned Systems Magazine*, vol. 11, no, 3, pp. 38-40, 1993.

[56] D. W. Murphy and J. Bott. On the Lookout: The Air Mobile Ground Security and Surveillance System (AMGSSS) Has Arrived. *Unmanned Systems,* vol. 13, no. 4, pp 22-27, 1995,

[57] J. P. Cycon and C. A. Thornberg. Sikorsky Aircraft’s Unmanned Aerial Vehicle, Cypher System Description and Program Accomplishments. *American Helicopter Society 51rd Annual Form*, 1995.

[58] D. W. Murphy, J. P. Bott, W. D. Bryan, J. L. Coleman, D. W. Gage, H. G. Nguyen, and M.P. Cheatham. MSSMP: No Place to Hide. *Proceedings of AUVSI'97*, pp. 281-290, 1997.

[59] J. P. Cycon and D. M. Walsh. Autonomous Flight of the Cypher UAV. *Proceedings American Helicopter Society 53rd Annual Form,* 1997.

[60] M. A. Kovacina, D. Palmer, G. Yang and R. Vaidyanathan. Multi-agent control algorithms for chemical cloud detection and mapping using unmanned air vehicles. *IEEE International Conference on Intelligent Robots and Systems*, vol. 3, pp. 2782-2788, 2002.

[61] N. J. S. Stacy, D. W. Craig, J. Staromlynska and R. B. Smith. The Global Hawk UAV Australian deployment: imaging radar sensor modifications and employment for maritime surveillance. *Proceedings of 24th Canadian Symposium on Remote Sensing*, pt. 2, vol. 2, pp. 699-701, 2002.

[62] A. Ryan, M. Zennaro, A. Howell, R. Sengupta and J. K. Hedrick. An overview of emerging results in cooperative UAV control. *Proceedings of the IEEE Conference on Decision and Control*, vol. 1, pp. 602-607, 2004.

[63] E. Walby, M Logan and J. Perry. Global Hawk support to homeland security operations. *Collection of Technical Papers - AIAA 3rd "Unmanned-Unlimited" Technical Conference, Workshop, and Exhibit*, vol. 1, pp. 170-173, 2004.

[64] J. S. Myers and E. Hildum. NASA UAV sensor development: Works in progress. *Collection of Technical Papers - AIAA 3rd "Unmanned-Unlimited" Technical Conference, Workshop, and Exhibit*, vol. 1, pp. 328-334, 2004.

[65] M. Franzbiau. Unmanned aerial vehicles for the future combat systems unit of action. *Proceedings of the AUVSI's Unmanned Systems North America 2004*, pp. 985-1001, 2004.

[66] A. P. Narayanasamy and A. A. Reyes. Definition and optimization of a parametrized, high-level design for a border patrol system. *Proceedings of the AUVSI's Unmanned Systems 2005*, pp. 1237-1251, 2005.

[67] I. Bostock. Australia to deploy Skylark UAVs for Iraq operations. *Jane's Defence Weekly*, November, pp. 111-112, 2005.

[68] L. Dickerson. UAVs buoyed by defense. *Aviation Week and Space Technology*, vol. 162, no. 3, pp. 101-104, 2005.

[69] L. A. Ingham, T. Jones and A. Maneschijn. Considerations for UAV design and operation in South African airspace. *Aeronautical Journal*, vol. 110, no. 1112, pp. 695-701, 2006.

[70] N. Brown and D Kemp. MUAS progress boosts Australian UAV plans. *Jane's Navy International*, July, 2006.

[71] N. Nrown and D. Kemp. Australia approves UAV patrol plan. *Jane's Defence Weekly*, July, 2006.

[72] R. Vachtsevanos and B. Ludington. Unmanned aerial vehicles: challenges and technologies for improved autonomy. *WSEAS Transactions on Systems*, vol. 5, no. 9, pp. 2164-2171, 2006.

[73] R. W. Beard, T. W. McLain, D. B. Nelson, D. Kingston and D. Johanson. Decentralized cooperative aerial surveillance using fixed-wing miniature UAVs. *Proceedings of the IEEE*, vol. 94, no. 7, pp. 1306-1324, 2006.

[74] S. Kiyotani. Japan pushes ahead with UAVs. *Jane's Defence Weekly*, January, pp. 589-590, 2006.

[75] P. L. Coronado, F. Stetina and D. Jacob. New technologies to support NASA's Mission to Planet Earth satellite remote sensing product validation: the use of an unmanned autopiloted vehicle (UAV) as a platform to conduct remote sensing. *Proceedings of the SPIE - The International Society for Optical Engineering*, vol. 3366, pp. 38-49, 1998.

[76] C. Baldwin, D. Chitwood, B. Demann, and J. Ducheny and R. Hampton. Design of an Unmanned Martian Polar Exploration System. *National Aeronautics and Space Administration, Washington, DC. Report: NAS 1.26:197160*, 1994.

[77] L. A. Young, E. W. Aiken, M. R. Derby, R. Demblewski and J. Navarrete. Experimental Investigation and Demonstration of Rotary-Wing Technologies for Flight in the Atmosphere of Mars. Proceedings of the 58th Annual Forum of the American Helicopter Society, 2002.

[78] D. Quagliarella and A. D. Cioppa. Genetic algorithms applied to the aerodynamic design of transonic airfoils. *Journal of Aircraft*, vol. 32, pp. 889-891, 1995.

[79] S. Obayashi and A. Oyama. Three-dimensional Aerodynamic Optimization with Genetic Algorithm. Proceedings of the Third ECCOMAS Computational Fluid Dynamics Conference, Paris, Sep 9-13, 1996.

[80] A. Vicini and D. Quagliarella. Inverse and direct airfoil design using a multiobjective genetic algorithm. *AIAA Journal*, vol. 35, pp. 1499-1505, 1997.

[81] S. Obayashi, Y. Yamaguchi and T. Nakamura. Multiobjective genetic algorithm for multidisciplinary design of transonic wing planform. *Journal of Aircraft*, vol. 34, pp. 690-693, 1997.

[82] A. Oyama, S. Obayashi, K. Nakahashi and T. Nakamura. Transonic Wing Optimization Using Genetic Algorithm. AIAA Paper 97-1854, AIAA 13th Computational Fluid Dynamics Conference, Snow mass, Colorado, 1997.

[83] S. Takahashi, S. Obayashi and K. Nakahashi. Inverse design optimization of transonic wings based on multi-objective genetic algorithms. *AIAA journal*, vol. 37, pp.1656-1662, 1999.

[84] B. R. Jones, W. A. Crossley and A. S. Lyrintzis. Aerodynamic and aeroacoustic optimization of rotorcraft airfoils via a parallel genetic

algorithm. *Journal of Aircraft*, vol. 37, pp.1088-1096, 2000.

[85] V. R. Akula and R. Ganguli. Finite element model updating for helicopter rotor blade using genetic algorithm. *AIAA journal*, vol. 41, pp. 554-556, 2003.

[86] L. Iuspaa, F. Scaramuzzinoa and P. Petrenga. Optimal design of an aircraft engine mount via bit-masking oriented genetic algorithms. Advances in Engineering Software, vol. 34, pp. 707-720, 2003.

[87] S. Gunawan, S. Azarm and J. Wu. Quality-assisted multi-objective multidisciplinary genetic algorithms. *AIAA Journal*, vol. 41, pp.1752-1762, 2003.

[88] S. Watkins. Development of a micro air vehicle. *The Aeronautical Journal*, vol. 107, pp. 117-123, 2003.

[89] I. Shimoyama, M. Miura, K. Suzuki and Y. Ezura. Insect-like microrobots with external skeletons. *IEEE Control Systems Magazine*, vol. 13, no. 1, pp. 37-41, 1993.

[90] Y. Kubo, I. Shinoyama, T. Kaneda and H. Miura. Study on wings of flying microrobots. *Proceedings of 1994 IEEE International Conference on Robotics and Automation*, vol. 1, pt. 1, pp. 834-839, 1994.

[91] K. I. Arai, W. Sugawara, K. Ishiyama, T. Honda and M. Yamaguchi. Fabrication of small flying machines using magnetic thin films. *IEEE Transactions on Magnetics*, vol. 31, no. 6, pt.2, pp. 3758-3760, 1995.

[92] J. Hollingum. Military look to flying insect robots. Industrial Robot, vol. 25, no. 2, pp. 124-128, 1998.

[93] N. Miki and I. Shimoyama. Analysis of the flight performance of small

magnetic rotating wings for use in microrobots. *IEEE International Conference on Robotics and Automation*, vol. 4, Pt.4, pp. 3065-3070, 1998.

[94] R. S. Fearing, K. H. Chiang, M. H. Dickinson, D. L. Pick, M. Sitti and J. Yan. Wing transmission for a micromechanical flying insect. *IEEE International Conference on Robotics and Automation*, vol.2, pt. 2, pp. 1509-1516, 2000.

[95] R. T. Vaughan, G. S. Sukhatnemf, F. J. Mesa-martinez and J. F. Montgomery. Fly spy lightweight localization and target tracking for cooperating ground and air robots. Proceedings of the International Symposium on Distributed Autonomous Robotic Systems, 2000

[96] T. N. Pornsin-sirirak, S. W. Lee, H. Nassef, J. Grasmeyer, Y. C. Tai, C. M. Ho and M. Keennon. MEMS wing technology for a battery-powered ornithopter. Proceedings of the IEEE Micro Electro Mechanical Systems, pp. 799-804, 2000.

[97] J. Yan, R. J. Wood, S. Avadhanula, M. Sitti and R. S. Fearing. Towards flapping wing control for a micromechanical flying insect. *IEEE International Conference on Robotics and Automation*, vol. 4, pp. 3901-3908, 2001.

[98] M. Sitti. PZT actuated four-bar mechanism with two flexible links for micromechanical flying insect thorax. *IEEE International Conference on Robotics and Automation*, vol. 4, pt.4, pp. 3893-900, 2001.

[99] R. J. Wood and R. S. Fearing. Flight force measurements for a micromechanical flying insect. *IEEE International Conference on Intelligent Robots and Systems*, vol. 1, pp. 355-362, 2001.

[100] T. N. Pornsin-Sirirak, Y. C. Tai, H. Nassef and C. M. Ho. Titanium-alloy MEMS wing technology for a micro aerial vehicle application, *Sensors and Actuators A*, vol. 89, no. 1-2, pp. 95-103, 2001.

[101] X. Deng, L. Schenato and S. Luca. Hovering flight control of a micromechanical flying insect. *Proceedings of the IEEE Conference on Decision and Control*, vol. 1, pp. 235-240, 2001.

[102] L. Schenato, X. Deng and S. S. Sastry. Flight control system for a micromechanical flying insect Architecture and implementation. *Proceedings of IEEE International Conference on Robotics and Automation*, vol. 2, pp. 1641-1646, 2002.

[103] P. G. Ifju, D. A. Jenkins, S. Ettinger, Y. Lian, W. Shyy, and M. R. Waszak. Flexible-wing-based micro air vehicles. AIAA Paper 2002-0705, 2002.

[104] S. Avadhanula, R. J. Wood, D. Campolo and R. S. Fearing. Dynamically tuned design of the MFI thorax. *IEEE International Conference on Robotics and Automation*, vol. 1, pp. 52-59, 2002.

[105] W. C. Wu, R. J. Wood and R. S. Fearing. Halteres for the micromechanical flying insect. *IEEE International Conference on Robotics and Automation*, vol. 1, pp. 60-65, 2002.

[106] X. Deng, L. Schenato and S. S. Sastry. Model identification and attitude control scheme for a micromechanical flying insect. *7th International Conference on Control, Automation, Robotics and Vision*, pt. 2, vol. 2, pp. 1007-1012, 2002.

[107] D. Campolo, R. Sahai and R. S. Fearing. Development of piezoelectric bending actuators with embedded piezoelectric sensors for micromechanical

flapping mechanisms. *IEEE International Conference on Robotics and Automation*, vol. 3, pp. 3339-3346, 2003.

[108] J. Yan and R. S. Fearing. Wing Force Map Characterization and Simulation for the Micromechanical Flying Insect. *IEEE International Conferemce on Intelligent Robots and Systems*, vol. 2, pp. 1343-1349, 2003.

[109] M. Sitti. Piezoelectrically actuated four-bar mechanism with two flexible links for micromechanical flying insect thorax. *IEEE/ASME Transactions on Mechatronics*, vol. 8, no. 1, pp. 26-36, 2003.

[110] R. J. Wood, S. Avadhanula, M. Menon and R. S. Fearing. Microrobotics using composite materials The micromechanical flying insect thorax. *IEEE International Conference on Robotics and Automation*, vol. 2, pp. 1842-1849, 2003.

[111] S. Avadhanula, R. J. Wood, E. Steltz, J. Yan and R. S. Fearing. Lift force improvements for the micromechanical flying insect. *Proceedings of the 2003 IEEE/RSJ International Conference on Intelligent Robots and Systems*, pt. 2, vol. 2, pp. 1350-1356, 2003.

[112] W.-C. Wu, L. Schenato, R. J. Wood and R. S. Fearing. Biomimetic sensor suite for flight control of a micromechanical flying insect design and experimental results. *IEEE International Conference on Robotics and Automation*, pt.1, vol. 1, pp. 1146-1151, 2003.

[113] X. Deng, L. Schenato and S. Sastry. Model identification and attitude control for a micromechanical flying insect including thorax and sensor models. *IEEE International Conference on Robotics and Automation*, vol. 1, pp. 1152-1157, 2003.

[114] L. Schenato, W. C. Wu and S. Sastry. Attitude control for a micromechanical flying insect via sensor output feedback. *IEEE Transactions on Robotics and Automation*, vol. 20, No. 1, pp. 93-106, 2004.

[115] E. Steltz, R. J. Wood, S. Avadhanula and R. S. Fearing. Characterization of the micromechanical flying insect by optical position sensing. *Proceedings of the 2005 IEEE International Conference on Robotics and Automation*, pp. 1252-1257, 2005.

[116] L.-J. Yang, C. K. Hsu, J.-Y. Ho, H.-H. Wang and G.-H. Feng. The micro aerial vehicle (MAV) with flapping wings. *2005 IEEE International Conference on Mechatronics*, pp. 811-815, 2005.

[117] R. Zbikowski, C. Galinski and C. B. Pedersen. Four-bar linkage mechanism for insectlike flapping wings in Hover concept and an outline of its realization. *Transactions of the ASME, Jounral of Mechanical Design*, vol. 127, no. 4, pp. 817-824, 2005.

[118] S. Avadhanula and R. S. Fearing. Flexure design rules for carbon fiber microrobotic mechanisms. *Proceedings of the 2005 IEEE International Conference on Robotics and Automation*, pp. 1579-1584, 2005.

[119] W. Shyy, P. Ifju and D. Viieru. Membrane wing-based micro air vehicles, *Applied Mechanics Reviews*, vol. 58, no. 1-6, pp. 283-301, 2005.

[120] D. Zuo, W. Chen, S. Peng and W. Zhang. Modeling and simulation study of an insect-like flapping-wing micro aerial vehicle. *Advanced Robotics*, vol. 20, no. 7, pp. 807-824, 2006.

[121] P. G. Ifju, B. Stanford, M. Sytsma and R. Albertani. Analysis of a flexible wing micro air vehicle. *Collection of Technical Papers - 25th AIAA*

Aerodynamic Measurement Technology and Ground Testing Conference, vol. 2, pp. 734-748, 2006.

[122] X. Deng, L. Schenato, W. C. Wu and S. S. Sastry. Flapping flight for biomimetic robotic insects part I-system modeling. *IEEE Transactions on Robotics*, vol. 22, no. 4, pp. 776-788, 2006.

[123] X. Deng, L. Schenato, W. C. Wu and S. S. Sastry. Flapping flight for biomimetic robotic insects part II-flight control design. *IEEE Transactions on Robotics*, vol. 22, no. 4, pp. 789-803, 2006.

[124] S. Martello, D. Pisinger, and D. Vigo.The three-dimensional bin packing problem. *Operations Research*, vol. 48, pp.256-267, 2000.

[125] D. Pisinger. Heuristics for the container loading problem. *European Journal of Operations Research*, vol. 141, pp. 382-392, 2002.

[126] W. A. Crossley, D. H. Laananen. Conceptual design of helicopters via genetic algorithm, *Journal of Aircraft*, vol. 33, pp.1062-1070, 1996.

[127] R. W. Prouty. *Helicopter aerodynamics*, Phillips Publishing, 1985.

[128] T. T. H. Ng and G. S. B. Leng. Design Tool for Small-scaled Rotary-Wing Unmanned Air Vehicle. *Aerospace Technology Seminar 2001*, Singapore, Sept 2001.

[129] T. T. H. Ng and G. S. B. Leng. Design optimization of rotary-wing micro air vehicles. *Proc. Instn. Mech. Engrs, Part C, Journal of Mechanical Engineering Science*. (In press).

[130] J. P. Cohoon, S. U. Hedge, W. N. Martin and D. Richards. Punctuated equilibria: a parallel genetic algorithm. *Proceedings of the second International Conference on Genetic Algorithms*, pp. 148-154, 1987.

[131] MPICH – A portable implementation of MPI. http://www-unix.mcs.anl.gov/mpi/mpich.

[132] M. Rao, S. K. Biswas, B. P. Butz, and D. G. Miller. Dynamic modeling and feedback control of a side-by-side tandem helicopter. *5th IEEE International Symposium on Intelligent Control*, vol. 2, pp. 780-785, 1990.

[133] R F. Stengel, J. R. Broussard and P. W. Berry. Digital flight control design for a tandem-rotor helicopter, *Automatica*, vol. 14, no. 4, pp. 301-312, 1978.

[134] C. P. Coleman. A Survey of Theoretical and Experimental Coaxial Rotor Aerodynamic Research. *NASA Tech Paper* 3675, 1997.

[135] A. Dzul, T. Hamel and R. Lozano. Modeling and nonlinear control for a coaxial helicopter. *Proceedings of the IEEE International Conference on Systems, Man and Cybernetics. Conference*, vol. 6, pt. 6, pp. 7-12, 2002.

[136] Y. Su and Y. Cao. A nonlinear inverse simulation technique applied to coaxial rotor helicopter maneuvers. *Aircraft Engineering and Aerospace Technology*, vol. 74, no. 6, pp. 525-533, 2002.

[137] E. Oemichen. The Oemichen-Peugeot Helicopter. NACA Tech Memo 13, 1921.

[138] E. Altug, J. P. Ostrowski and R. Mohony. Control of a Quadrotor Helicopter Using Visual Feedback. *IEEE International Conference on Robotics and Automation*, pp. 72-77, 2002.

[139] G. Hoffmann, D. G. Rajnarayan, S. L. Waslander, D. Dostal and C. J. Tomlin. The Stanford Testbed of Autonomous Rotorcraft for Multi Agent Control (STARMAC). *23rd Digital Avionics System Conference*, Salt Lake City, UT, November 2004

[140] M. Chen and M. Huzmezan. A Combined MBPC_2 DOF H∞ Controller for a Quad Rotor UAV. *AIAA Atmospheric Flight Mechanics Conference and Exhibit*, pp. 329-341, 2005.

[141] A. Tayebi and S. McGilvray. Attitude stabilization of a VTOL quadrotor aircraft. *IEEE Transactions on Control Systems Technology*, vol. 14, no. 3, pp. 562-571, 2006.

[142] L.-C. Lai, C.-C. Yang and C.-J. Wu. Time-optimal control of a hovering quad-rotor helicopter. *Journal of Intelligent and Robotic Systems Theory and Applications*, vol. 45, no. 2, pp. 115-135, 2006.

[143] P. Pounds, R. Mahony and P. Corke. Modelling and control of a quad-rotor robot. *Proceedings of the 2006 Australasian conference on robotics & automation*, 2006.

[144] T. T. H. Ng and G. S. B. Leng. Unconventional Control Design of Small-scaled Unmanned Air Vehicle. *Aerospace Technology Seminar 2002*, Singapore, Sept. 2002.

[145] T. T. H. Ng. Unconventional Control Design of Unmanned Air Vehicle Using Genetic Algorithm. *Numerical Analysis in Engineering 2003 (NAE 2003)*, Batam, Indonesia, 13th-15th Mar., pp.19-26, 2003.

[146] S. Morris. Design and flight test results for micro-sized fixed-wing and VTOL aircraft. *Proceedings of The First International Conference on Emerging Technologies for Micro Air Vehicles*. Georgia Institute of Technology, Atlanta GA, Feb. 1997.

[147] M. Rais-Rohani and G. R. Hicks. Multidisciplinary design and prototype development of a micro air vehicle. *Journal of Aircraft*, vol. 36, no. 1, pp.

227-231, 1999.

[148] J. M. Grasmeyer and M. T. Keennon. Development of the black widow micro air vehicle. *AIAA Paper* AIAA-2001-0127, 2000.

[149] H.-Y. Wu, D. Sun, Z.-Y. Zhou,S.-S. Xiong, X.-H. Wang. Micro Air Vehicle Architecture and Implementation. *Proceedings of the 2003 IEEE International Conference on Robotics & Automation*, Taipei, Taiwan, Sep. 14-19, pp. 534-539, 2003.

[150] G. La Rosa, G. Mirone and A. Risitano. Preliminary design and wind tunnel tests of a micro air vehicle for surveillance and sensor-bearing applications. *Proc. Instn. Mech. Engrs, Part G, Journal of Aerospace Engineering*, vol. 219, pp. 1-10, 2005.

[151] P. Spellucci. An SQP method for general nonlinear programs using only equality constrained subproblems. *Math. Prog.*, vol. 82, pp. 413-448, 1998.

[152] P. Spellucci. A new technique for inconsistent problems in the SQP method. *Math. Meth. of Oper. Res.*, vol. 47, pp. 355-400, 1998.

[153] E. M. Murman and A. Rizzi. Application of Euler Equations to Sharp Edge Delta Wings with Leading Edge Vortices. *AGARD Symposium on Application of Computational Fluid Dynamics in Aeronautics*, Aix-en-Provence, France, April 1986.

[154] V. M. Falkner. The Calculation of Aerodynamic Loading on Surface of Any Shape, ARC R & M 1910, National Physical Lab., Teddington, England, Aug. 1943.

[155] P. E. Rubbert. Theoretical Characteristics of Arbitrary Wings by a Non-Planar Vortex Lattice Method, D6-9244, The Boeing Co., Renton, Wash.,

1964.

[156] R. J. Margason, S. O. Kjelagaard, W. L. Sellers III, C. E. K. Morris, K. B. Walkey Jr. and E. W. Shields. Subsonic Panel Methods – A Comparison of Several Production Codes, AIAA Paper 85-0280, AIAA 23rd Aerospace Sciences Meeting, Jan, 1985.

[157] T. T. H. Ng and G. S. B. Leng. Design of Small-scaled Air Vehicles using Multidisciplinary Optimisation (MDO). *Aerospace Technology Seminar 2000*, Singapore, Sept. 2000.

[158] T. T. H. Ng and G. S. B. Leng. Application of Genetic Algorithms to Conceptual Design of a Micro-air Vehicle. *Engineering Applications of Artificial Intelligence*, vol. 15, Issue 5, pp. 439-445, 2002.

[159] J. Holland. *Adaptation in natural and artificial systems*, Univ. of Michigan Press, Ann Arbor, MI, 1975.

[160] K. A. De Jong. *An analysis of the behaviour of genetic adaptive systems*, Dissertation Abstracts International, University Microfilms, Michigan, 41(9), 3503B, 1975.

[161] D. E. Goldberg. *Genetic algorithm in search, optimization, and machine learning*. Addison Wesley, Reading, MA, 1989.

[162] A. H. Wright. Genetic algorithms for real parameter optimization. *Foundations of Genetic Algorithms*, J.E. Rawlins (Ed.), Morgan Kaufmann, 1991.

[163] H. Muhlenbein and D. Schlierkamp-Voosen. Predictive models for the breeder genetic algorithm. *Evolutionary Computation*, vol. 1, no. 1, pp. 25-49, 1993.

[164] R. Fletcher and M. J. D. Powell. A rapidly convergent descent method for minimization. *Computer J.,* vol. 6, pp. 163-168, 1963.

[165] R. Fletcher and C. M. Reeves. Function mimization by conjugate gradients. *Computer J.,* vol. 7, pp. 149-154, 1964.

[166] A. A. Goldstein and J. F. Price. An effective algorithm for minimization. *Numer. Math.,* vol. 10, pp. 184-189, 1967.

[167] H. Muhlenbein, M. Gorges-Schleuter and O. Kramer. Evolution algorithms in combinatorial optimization. *Parallel Computing*, vol. 7, pp. 65-85, 1988.

[168] D. Whitley, T. Starkweather and D' A. Fuquay. Scheduling problems and traveling salesman: The genetic edge recombination operator. *Proceedings of the Third International Conference on Genetic Algorithms*, pp. 133-140, 1989.

[169] J. Cohoon, S. Hegde and N. Martin. Distributed genetic algorithms for the floorplan design problems. *IEEE Transactions on Computer-Aided Design*, vol. 10, pp. 483-491,1991.

[170] S. Rajeev and C. S. Krishnamoorthy. Discrete optimization of structures using genetic algorithms. Journal of Structural Engineering, vol. 118, no. 5, pp. 1233-1250, 1992.

[171] K. Tam. Genetic algorithms, function optimization, facility layout design. *European Journal of Operation Research*, vol. 63, pp. 322-346, 1992.

[172] H. M. Cartwright and S. P. Harris. Analysis of the distribution of airborne pollution using GAs. *Atmos. Environ* vol. 27A, pp.1783–1791, 1993.

[173] E. Falkenauer. A new representation and operators for GAs applied to grouping problems. *Evolutionary Computation*, vol. 2, No. 2, pp. 123-144,

1994.

[174] D. M. Tate and A. E. Smith. Unequal-area facility layout by genetic search, *IIE Transaction*, vol. 27, pp. 465-472, 1995.

[175] T. Yokota, M. Gen and K. Ida. System reliability of optimization problems with several failure modes by genetic algorithm. *Japanese Journal of Fuzzy Theory and Systems*, vol. 7, pp.117-185, 1995.

[176] D. K. Anthony and A. J. Keane. Robust-optimal design of a lightweight space structure using a genetic algorithm. *AIAA Journal*, vol. 41, pp. 1601-1604, 2003.

[177] D. J. Fonseca, S. Shishoo, T. C. Lim and D. S. Chen. A genetic algorithm approach to minimize transmission error of automotive spur gear sets. *Applied Artificial Intelligence*, vol. 19, pp.153-179, 2005.